Plasma Response to Magnetic Perturbations Relevant to Edge Localised Modes in Tokamaks

Andrew Robert Allen (MENG, MAppNucSci)

York Plasma Institute

Physics

University of York

Doctor of Philosophy

09/2013

Abstract

Edge Localised Modes (ELMs) are repetitive eruptions of particles and energy which occur in many high confinement mode plasmas. In present devices the power loads delivered to the divertor during an ELM do not pose a serious problem. However, extrapolations to the ITER tokamak suggest that divertor lifetimes maybe reduced below acceptable levels. The application of Resonant Magnetic Perturbations (RMPs) to the plasma has successfully demonstrated ELM mitigation and suppression, under a number of operating scenarios. However, the physical mechanism by which mitigation and suppression is achieved is still not well understood. Furthermore many questions remain concerning the threshold perturbation strength and perturbation spectrum required.

Models and theory initially developed for error field analysis are increasingly being used, and developed, to explain the plasma response to RMPs. The BOUT++ code is tested against a selection of linear layer problems. This is a first step in applying code to model the self consistent plasma response to RMPs. The code is demonstrated to be consistent with theory in all cases modelled. In addition for the first time the importance of radial grid packing is considered in obtaining accurate simulations to RMP experiments.

A novel multi-surface model is developed, and a single and two surface model is applied to the neighbourhood of the radial location at which the perpendicular electron rotation is zero. Bifurcation windows are produced which are in qualitative agreement with ELM suppression q_{95} windows. Bifurcation locusts are also shown to be in qualitative agreement with the experimental spectrum results of M. E. Fenstermacher et al, Nucl. Fusion 48:122001, 2008.

Contents

List of Figures

Acknowledgements

Declaration

I declare that the work in this thesis is my own and that it has not been submitted for examination at this or any other institution for another award.

Chapter 1

Introduction

1.1 Motivation

In mid 2011 the estimated world population exceeded 6.9 billion, with $\sim 82\%$ residing in less developed regions. These figures are projected to increase to 9.3 billion and $\sim 86\%$ respectively by 2050 (using the medium variant model) ([1]). Additionally, energy consumption per capita has been growing at an approximately constant rate of 0.7% p.a., with current projections up to 2030 predicting that this figure will remain approximately constant. Thus, world energy consumption appears set to increase over the foreseeable future ([2] predicting a 39% increase in world primary energy consumption by 2030). The projected increase in world energy use, coupled with the need to replace existing energy sources as they are decommissioned, is leading to an interesting debate concerning the role different energy sources should play in supplying future demand.

Of equal importance is the disparity in the energy consumption per capita between developed and less developed regions of the world. This naturally points to the longer term question, what is the energy consumption per capita necessary to allow people to achieve 'a socially acceptable standard of living at a given point in time'? This is a very open question, but if answered would allow a clear goal for longer term world energy policy.

Fossil fuels are estimated to supply 78% of the worlds current primary energy consumption [3]. However, the use of fossil fuels is leading to issues concerning

pollution, climate change, security of supply, and finite resources.

A complex mixture of air pollutants is associated with fossil fuel emissions. The most harmful of these to human health is fine particulate matter. Fine particulate matter is estimated to cause 9% of lung cancer deaths, 5 percent of cardopulmonary deaths, and 1 percent of respiratory deaths worldwide [4].

The burning of fossil fuels has led to a measurable impact on the atmosphere. The pre-industrial revolution atmospheric CO_2 concentration is estimated to have been around 280 ppm. Evidence suggests that this figure has remained roughly constant for of the order of 10^5 years ([5]). Since the time of the introduction of the efficient steam engine atmospheric CO_2 concentrations have dramatically increased (figure 1.1), exceeding 400 ppm in early 2013. Increasing CO_2 concentrations leads to increased absorption of infra-red radiation re-emitted from the earth leading to concerns of man made climate change.
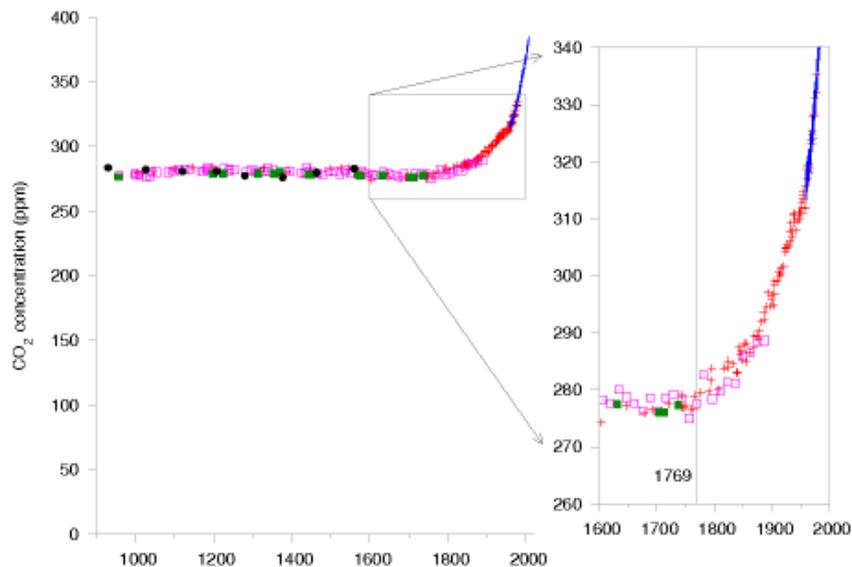
Figure 1.1: atmospheric CO_2 concentrations (ppm) against time ([6])

The inhomogeneous distribution of easily extractable fossil fuel resources, coupled with the inhomogeneous distribution of the worlds population and energy demand, have inevitably led to security of supply issues for many counties. Dramatic price fluctuations are a common feature often depending on the political

stability in fossil fuel supplying regions.

Fossil fuel resources pose less of an immediate problem than other factors, although, by nature, they are finite resources and will become depleted over a sufficient time-scale. Estimates of fossil fuel reserves predict that there is sufficient gas to last for ~ 230 years and sufficient coal to last for ~ 2000 years at the current rate of consumption [3]. It is possible that restrictions, or reduced incentives, may be applied to fossil fuel usage well before resource limitations can have an impact.

Renewable energy resources are both vast and essentially inexhaustible. Negligible CO_2 and atmospheric air pollution emission is produced from direct power generation (except in the case of Biomass). However, there may be some indirect emissions. Renewable sources typically suffer from three problems, low energy density, power fluctuations and for certain sources location issues.

Power fluctuations are inherent in many renewable power sources. These fluctuations do not match the fluctuations associated with power demand. Without efficient energy storage capability power fluctuations can place major strains on the grid. Additional generation capacity from alternative sources must also be held in reserve, increasing the actual cost of certain renewable sources well above the installation cost quoted.

Low energy density power sources inevitably require large amounts of land to reach typical target power requirements. For example solar photovoltaics and wind typically have an output power per unit area of $5-20W/m^2$ and $2-3W/m^2$ respectively (compared to $\sim 150kW/m^2$ for coal and nuclear power [7]).

The large land usage and regions of naturally higher relative energy density can led to restrictions on the location of where certain renewable power sources can be placed.

The use of nuclear fission could be greatly expanded to provide high energy density, base load electricity production. It provides a direct method for avoiding virtually all the issues discussed which concern fossil fuels. Both atmospheric air pollution and CO_2 emissions are minimal. The lifetime of Uranium fuel reserves varies hugely depending on the fuel cycle employed and whether extraction from sea water is considered ([8]). The flexibility of choosing the employed fuel cycle, the relative stability of nations rich in Uranium Ore, coupled with the relatively small mass and volume of fuel required in a fission reactor means that security of

supply is a much smaller issue than for fossil fuels.

It is unfortunate that nuclear fission suffers from other issues though. The public perception of the relative safety of fission power plants has been eroded by a combination of a series of nuclear accidents and largely negative publicity. By design a large amount of potential energy is contained within the reactor at any one time (around 3 years worth of fuel). Although relative safety concerns are perhaps unjustified on a statistical basis, against other power sources, the public perception of risk has led to some countries refusing to use fission power altogether.

The nuclear waste legacy is also of primary concern and is also largely fuel cycle dependent. Nuclear waste from a once through fuel cycle is estimated to have a greater radio toxicity level than natural Uranium Ore for of the order of 10^5 years. Reprocessing Plutonium can reduce this time scale by around a factor of 10. Further conversion of long lived actinides to fission products in fast reactors or accelerator driven systems can reduce the time-scale to around 300-1000 years. Increased costs are involved in implementing waste burning technologies though [9].

Nuclear proliferation is an additional issue and has led to political tensions between a number of countries over recent years. Extraction of Plutonium for weapons use is easier from certain reactor types than others [9]. Reprocessing fuel cycles have been not been considered by certain countries primarily because of proliferation concerns.

Fusion energy has the potential to provide a high energy density base load power source with negligible CO_2 and atmospheric pollution emission. It has a virtually limitless and widely abundant fuel supply, estimates ranging between 5000 years to 100 billion years, based on the 2006 world electricity consumption, depending on the fusion reaction used [10], [7]. The components of the most commonly considered reaction are Deuterium and Tritium. Deuterium can be extracted from sea water, whilst Tritium can be produced from Lithium within the reactor itself. Lithium is a highly abundant element, and, coupled with the small requirements to produce large amounts of energy, security of supply or resource limitation present no problems.

Fusion reactors are inherently safe. Fuel is injected into the plasma, the

amount available at a given time is only able to sustain the fusion reactions for a few tenths of a second. Pure fusion (as opposed to hybrid fission-fusion rectors) do not pose any proliferation risks, the fissile material required for nuclear weapons not being produced. Radioactive waste is much smaller problem in fusion reactors as compared to fission reactors. The helium 'ash' contained in the plasma is not radioactive, however neutron production can activate some of the vessel structural materials. This can be minimised by careful selection of materials. The Tritium fuel has a short half-life of 12.3 years, and although careful handling is required, long term waste disposal is not an issue [11], [7].

The major obstacle associated with fusion reactors is the complexity of the scientific and engineering challenges compared with other energy sources. However, the progress in fusion research over the last 30 years has been remarkable. Reactor like conditions should finally be realised with the construction of ITER, the first plasma due in 2019.

1.2 Fusion

1.2.1 Conditions for Thermonuclear Fusion

It is an experimentally observed phenomena that the mass of a nucleus is not as large as the sum of the masses of its constituent protons and neutrons, when these protons and neutrons are not in the bound state. The binding energy per nucleon is the average energy per nucleon which would be required to break the nucleus into its individual components. Figure (1.2) displays the binding energy per nucleon vs. mass number curve. The general shape of this curve is well explained by basic geometrical arguments concerning the relative magnitudes and range of the attractive nuclear strong force and the repulsive coulomb force. It is observed that a maxima exists at $A \sim 56$ (Fe), and that this implies that energy may be released by the fusing of two light nuclei (fusion), or by the splitting of two heavy nuclei (fission) ([12]).

Of fundamental importance in the contrast in design between fusion and fission reactors, is the typical relative kinetic energies of the reacting particles required for induced reactions. A typical neutron in an induced U^{235} thermal fission re-
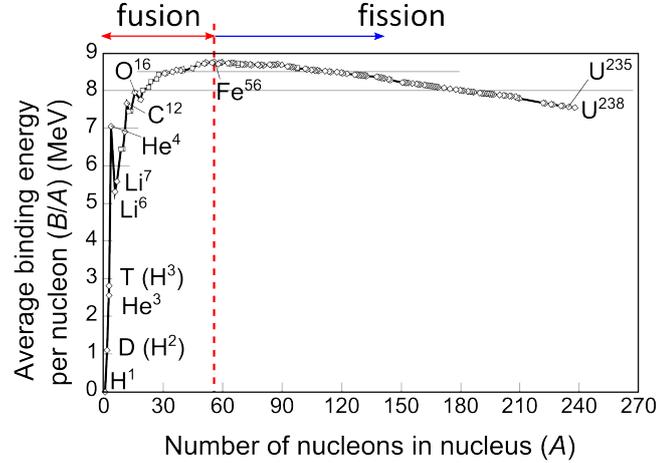
Figure 1.2: Binding energy per nucleon curve (Image courtesy of K. Imada)

action will have an kinetic energy of around $0.025eV$. In fact neutrons produced in thermal fission reactors are purposely passed though a moderator with the specific intention of slowing the neutron down to this energy. By contrast typical reacting nuclei undergoing fusion in a Deuterium-Tritium reactor will have kinetic energies of the order of 10's of KeV. The high energies required in the latter case are as a result of the coulomb force acting between the two like charged nuclei. This coulomb barrier must be at least partially overcome to raise the probability of a fusion reaction occurring. A quantity which characterises the probability of a fusion reaction occurring between an incident and target particle, is the fusion cross-section, σ. The cross-section is an effective interaction area presented by the target particle to the incident particle, which is dependant on their relative velocities. Figure 1.3(a) displays the dependence of the cross-section on the incident particle energy for some fusion reactions typically of interest in man-made reactors. It is clear from the combination of the larger cross-section at lower interaction energies and the large energy release per fusion reaction:

$$D^2 + T^3 \quad \longrightarrow \quad He^4 + n^1 + 17.6 MeV \tag{1.1}$$

$$D^2 + D^2 \quad \longrightarrow \quad He^3 + n^1 + 3.27 MeV \tag{1.2}$$

$$D^2 + D^2 \quad \longrightarrow \quad T^3 + H^1 + 4.03 MeV \tag{1.3}$$

$$D^2 + He^3 \quad \longrightarrow \quad He^4 + H^1 + 18.3 MeV \tag{1.4}$$
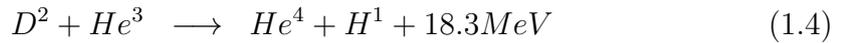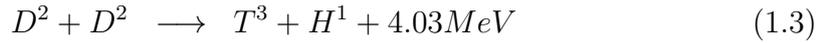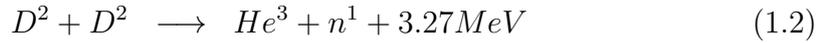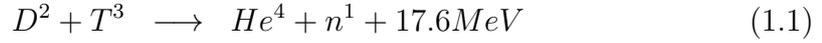
that the Deuterium-Tritium (D-T) reaction is the most promising of these reactions ([13]). Indeed the DT reaction is the most commonly pursued reaction in the fusion energy community. Knowledge of the fusion cross-section and the particular distribution functions of the reacting species allows for the calculation of the important quantity, the fusion reaction rate density, $R(\mathbf{x})$. For the D-T reaction the reaction rate density is encompassed by the following equation.

$$R(\mathbf{x}) = n_d n_t \langle \sigma v \rangle \tag{1.5}$$

The angled brackets, $\langle \sigma v \rangle$, indicates that the quantity is an average over velocity space. n_d and n_t are the number densities of deuterium and tritium respectively. Thermonuclear fusion, the process of providing the necessary energy to partially overcome the coulomb barrier by heating the reacting species, is the focus of this document. Calculations of the fusion reaction rate density typically assume that the reacting species are in thermodynamic equilibrium and therefore have Maxwellian distributions ([13]). The thermonuclear reactivity for the D-T reaction is displayed in figure 1.3(b), and at a particular point in space is only a function of temperature.

The design of any practical fusion reactor requires knowledge of the fusion power, P_f, produced in a given control volume (C.V.). Two quantities are required to calculate the fusion power, the fusion energy output per reaction, ε_f, for the reaction of interest, and fusion reaction rate density throughout the C.V..

$$P_f = \int_{C.V.} R(\mathbf{x}) \varepsilon_f d^3 x \tag{1.6}$$

However, the energy output per reaction is split between the kinetic energy given to the neutron (approx. 4/5ths) and the kinetic energy given to the alpha parti-
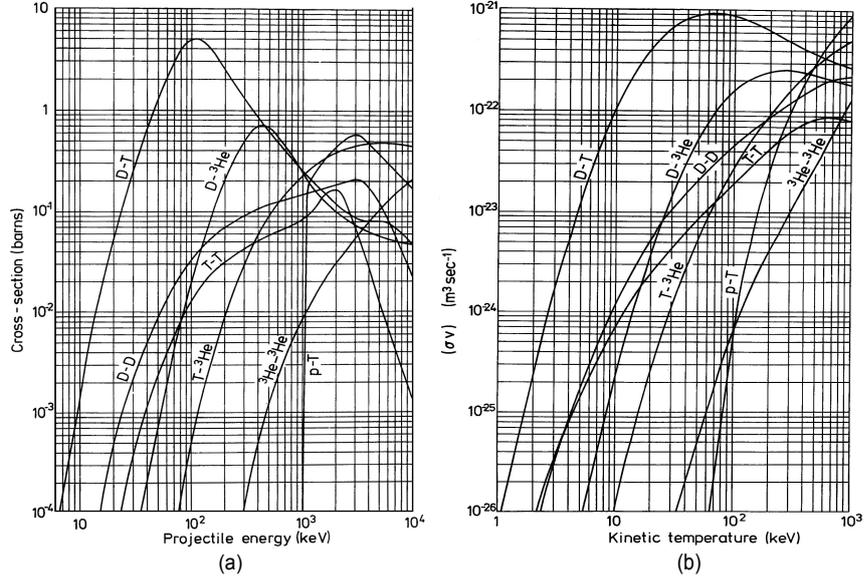
Figure 1.3: (a) fusion cross-sections. (b) fusion reactivity

cle, ε_α, (approx. 1/5th). It is assumed that the neutron does not interact with the plasma and so is lost to the C.V.. The charged alpha particle is assumed to undergo coulomb collisions with the surrounding plasma, and so is a source of plasma heating. If the alpha particle deposits most of it's energy in the surrounding plasma, before escaping the C.V., then the alpha particle heating power form is just a modified version of the total fusion power.

$$P_\alpha = \int_{C.V.} R(\mathbf{x})\varepsilon_\alpha d^3 x \qquad (1.7)$$

Energy is lost from the plasma contained in the C.V. at a rate P_L. If a steady state condition is desired and $P_\alpha < P_L$, then additional external power, P_H, must be supplied to maintain the plasma temperature, and consequently P_α. The steady state power balance condition is simply:

$$P_H + P_\alpha = P_L \qquad (1.8)$$

The ignition condition is attained if $P_\alpha = P_L$.

In such a steady state condition the 'confinement time', τ_E, can be defined as

the time for the thermal energy, W, contained in the C.V. to leak out of the C.V.

$$\tau_E = W/P_L \tag{1.9}$$

For a given C.V. geometry τ_E is characterised by the dominant transport mechanism ([14]).

The previously introduced definitions can be utilised to approximate the requirement for ignition. For a step pressure profile the ignition criterion takes the form ([13]):

$$nT\tau_E > 3 \times 10^{21} m^{-3} keV s \tag{1.10}$$

Ignition it not a necessary condition for a fusion reactor. A common measure of fusion reactor performance is the parameter named the Q value. It is the neutrons which escape from the control volume that generally provides the energy output of the reactor. Some of this energy may be recycled to be used for plasma heating. The Q value is defined as:

$$Q = P_f/P_H \tag{1.11}$$

As a reactor approaches ignition Q will tend to infinity.

1.2.2 Charged Particle Motion

At the high temperatures required for thermonuclear fusion the electrons are stripped from their nuclei, the matter in the control volume existing in the plasma state.

A charge particle moving in an electro-magnetic field will experience the Lorenz force.

$$\mathbf{F} = e_s(\mathbf{E} + \mathbf{v} \times \mathbf{B}) \tag{1.12}$$

In a purely homogeneous magnetic field the charged particle will gyrate about a magnetic field line whilst being unconstrained in its motion along the field line. The frequency at which the particle gyrates is known as its Larmor frequency,

$\Omega_s = e_s B/m_s$, and the direction of rotation is such that the effective current loop formed tries to decrease the magnetic flux though it. The radius of gyration is known as the Larmor radius, $r_l = v_\perp/\Omega_s$ (the $\perp$ indicating the perpendicular component to the field line).

The fact that the perpendicular motion of a charged particle is constrained by the magnetic field is a property exploited by magnetic confinement systems. Deviations away from a homogeneous magnetic field and the presence of an additional perpendicular force will cause the particles guiding centres to drift relative to the field line. The following is a brief explanation of the particle drifts used in this document.

A charged particle moving in a homogeneous magnetic field with an additional constant force, $\mathbf{F}$, exerted on the particle, will experience a perpendicular drift.

$$\mathbf{v}_{\perp D} = \frac{\mathbf{F} \times \mathbf{B}}{e_s B^2} \tag{1.13}$$

With the addition of a constant electric field, $\mathbf{F} = e_s \mathbf{E}$, the $\mathbf{E} \times \mathbf{B}$ drift takes the form:

$$\mathbf{v}_{\perp (E \times B)} = \frac{\mathbf{E} \times \mathbf{B}}{B^2} \tag{1.14}$$

It is of note that the $\mathbf{E} \times \mathbf{B}$ drift is of the same magnitude and direction for both electrons and ions.

In a magnetic field in which the field lines have a slight curvature the particle streaming along the field line, with velocity $v_\parallel$, will experience an effective centrifugal force, $\mathbf{F} = m v_\parallel^2 \mathbf{R}_c / R_c$. The resulting curvature drift is:

$$\mathbf{v}_{\perp c} = -\frac{m_s v_\parallel^2}{e_s B^2} \frac{\mathbf{B} \times \nabla B}{R_c^2} \tag{1.15}$$

R_c being the radius of curvature.

Yet another drift results if a gradient in the magnitude of the magnetic field perpendicular to the field line exists. The so called "∇B drift" is a result of the Larmor orbit "tightening" and "loosening" as the particle moves between regions of stronger and weaker field strengths.

$$\mathbf{v}_{\perp \nabla B} = \frac{m_s v_\perp^2}{2} \frac{\mathbf{B} \times \nabla B}{e_s B^3} \tag{1.16}$$

The direction of the curvature and ∇B drift is dependent on the sign of the charge, e_s.

1.2.3 The Tokamak

The tokamak is a device designed to confine a plasma in an axisymmetric toroidal configuration. It contains the plasma via the use of magnetic fields which are produced by external coils and the plasma itself. The primary dimensions of the system consist of the major and minor radius (R and a respectively in figure 1.4(b)). The ratio of these two quantities, R/a, defines a commonly used parameter known as the aspect ratio.

The most basic tokamak consists of three sets of coils. These are displayed in figure 1.4(a), and consist of the toroidal field coils, the ohmic transformer and the vertical field coils.
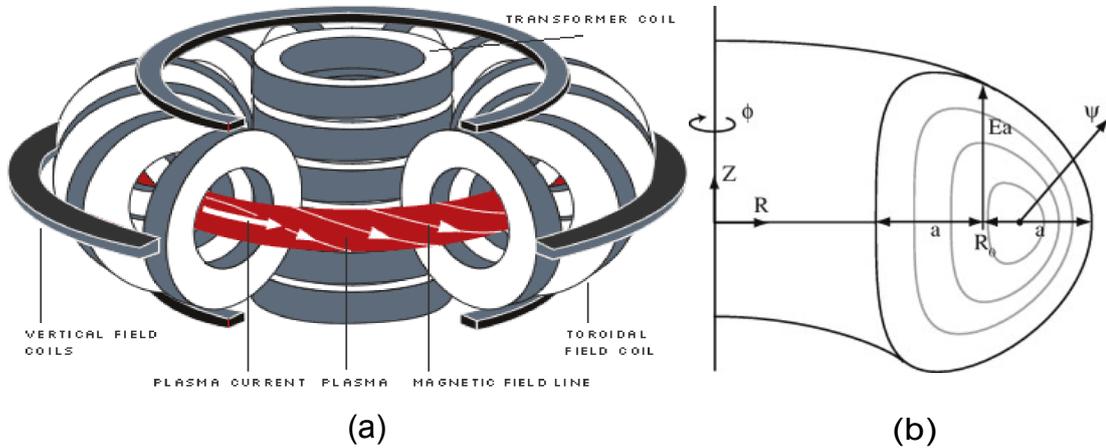
Figure 1.4: (a) The basic tokamak configuration. [Image courtesy of EFDA JET] (b) Key plasma dimensions, Elongation and Triangularity are also included. A set of nested flux surfaces.

The dominant contribution to the magnetic field is the toroidal component, the majority of which is produced by the toroidal field coils. It is the toroidal

component which sets the typical Larmor orbit radius. A minimum requirement for the strength of the toroidal field is that Larmor radii of 3.5 Mev fusion product α particles are small compared to the dimensions of the system [15].

A purely toroidal magnetic field cannot confine the plasma. Conceptually this can be understood in terms of single particle drifts. A charged particle moving in a toroidal field will experience a curvature drift and ∇B drift. Both drifts are in opposite directions for electrons and ions, leading to charge separation and a corresponding electric field. The resulting $\mathbf{E} \times \mathbf{B}$ drift will be in the ∇R direction fo both species (figure 1.5).

A mechanism to combat the outward drift of particles is to reduce the charge separation by requiring the field lines follow helical trajectories. The helical trajectory is achieved by adding a poloidal component to the magnetic field. In an axisymmetric device, in equilibrium with a non-zero pressure gradient(except at $r = 0$ and $r = a$), this requires that the field lines lie on a nested set of 'flux surfaces' (figure 1.4(b)). A charged particle initially located at a particular flux surface will now spend part its trajectory drifting away from the flux surface and part of its trajectory drifting towards the flux surface as it moves in poloidal location ([16]). The poloidal field is constructed by driving a toroidal current through the plasma. The toroidal current is driven by transformer action by ramping the current in the primary winding of the ohmic transformer, the plasma acting as the secondary winding.

The safety factor (or 'q' value) at a particular flux surface is defined to be the average pitch of the field line on that flux surface. For flux surfaces with a q value which is rational the field line will rejoin itself after a particular number of toroidal rotations. These surfaces are known as rational surfaces and play a key role in the plasma stability.

In the large aspect approximation, $R_0/a >> 1$, leading order force balance is satisfied by the balancing of the thermal and magnetic pressure. To the next order, toroidal effects exert forces in the ∇R direction. The hoop force and the tire force must be balanced by a compression of the flux surfaces on the low field side (the Shafranov shift). The hoop force is caused by self inductance of a current carrying circuit, and the tire force is due to the plasma pressure trying to expand the plasma volume, via increasing the major radius. Matching to the

poloidal magnetic field in the vacuum region reveals that force balance can only be achieved by the use of a vertical field. The combination of the vertical field (produced by the vertical field coils) and the plasma current produces and $\mathbf{J} \times \mathbf{B}$ force which balances the hoop, tire, and $1/R$ forces ([17]).
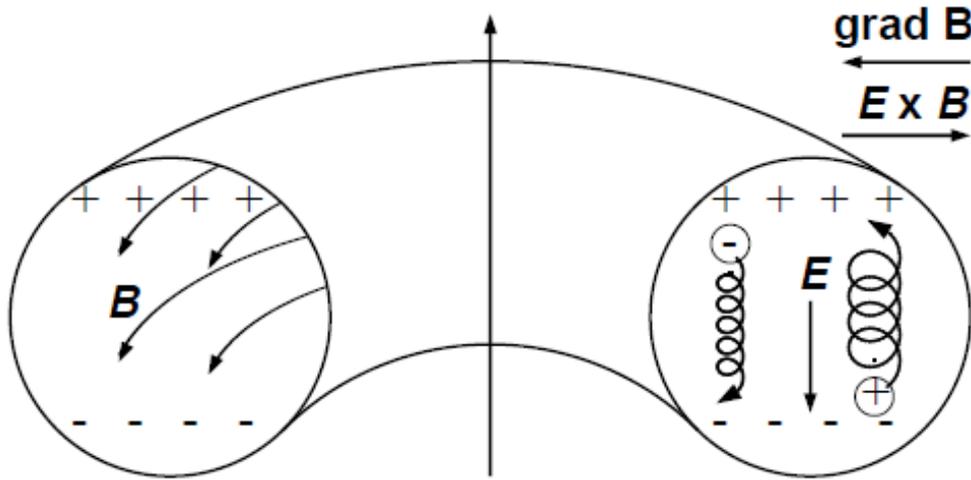
Figure 1.5: Particle drifts in a purely toroidal magnetic field ([16])

The sensitivity of radiative losses on the plasma impurity content, and low edge plasma pressures, requires that a vacuum vessel is employed to separate bulk plasma from the surrounding environment. However, the plasma must also be separated from the vacuum vessel to avoid impurities being introduced from the vacuum vessel itself. Two methods are currently employed for this purpose. A limiter of chosen material can be placed within the vacuum vessel defining an outer plasma boundary. The second method involves channelling particles in the edge plasma to a chosen location via the use of a magnetic divertor ([12]). The method employed in creating the magnetic divertor is conceptually simple. A current is driven in an external coil in the same direction as the toroidal plasma current. A null in the poloidal magnetic field will be created at a particular location dependant on the relative magnitude of the current in plasma and external coil. A surface can be defined, on which the null lies, within which closed

magnetic surfaces remain and external to which the magnetic surfaces are open ending at the divertor plates. Particle escaping from the separatrix will be guided by the magnetic field towards the divertor plates. Cross-field transport will give the 'Scape off Layer (SOL)' a finite thickness helping spread power loads to these plates.
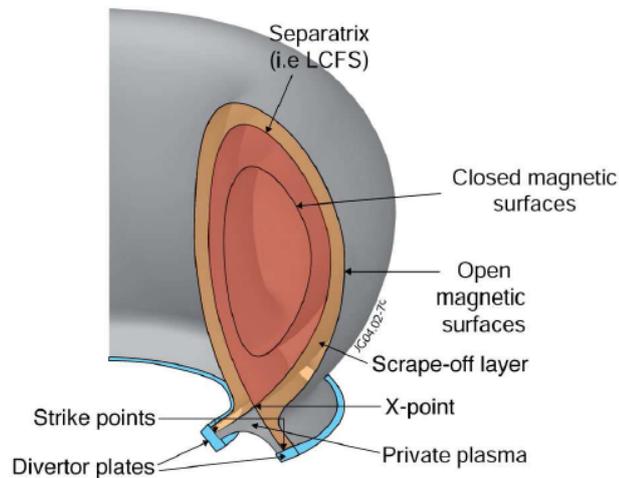
Figure 1.6: a tokamak divertor, [image courtesy of EFTA-JET]
.

1.2.4 Reconnection and Magnetic islands

The majority of a fusion plasma can be modelled as a perfectly conducting fluid (ideal plasma). In such a plasma fluid, fluid elements remain tied to the field lines, and the topology of the magnetic field can not change. However, at rational surfaces plasma resistivity may become important allowing magnetic field lines to slip though the plasma, brake and reconnect to form a different topology.

The magnetic structure of importance in this document is the magnetic island chain (figure 1.7). The island like structure is associated with current filamentation along magnetic field lines at the rational surface. Magnetic field lines are carried by the plasma towards the x point (ideal region), in the vicinity of the x
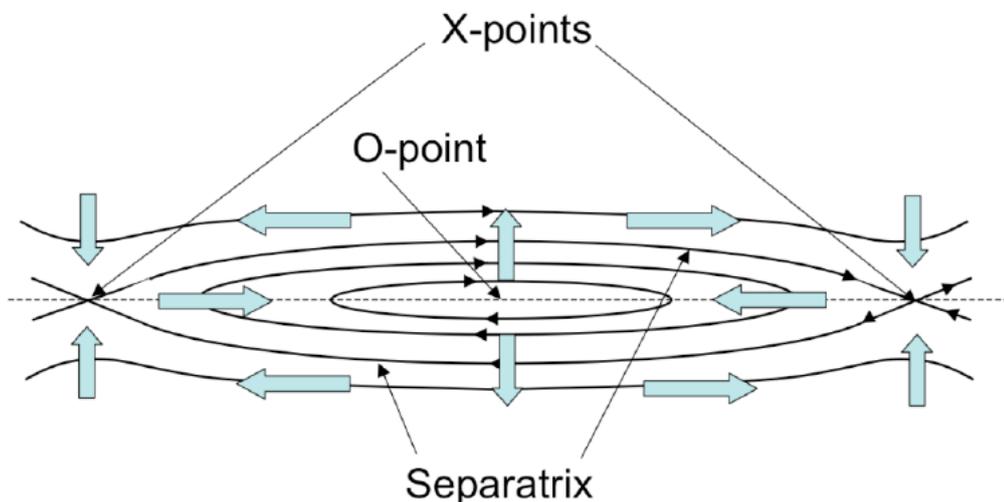
Figure 1.7: The magnetic island structure. The blue arrows indicate the flow pattern in the vicinity of the island [18].

point the field lines may brake and reconnect, the subsequent release of magnetic energy driving the plasma towards to the O point.

The plasma may undergo either spontaneous reconnection in a "tearing unstable plasma" or driven reconnection. Reconnection dynamics will be greatly expanded upon in chapter 2.

1.2.5 Error Fields

Error fields are non-toroidally symmetric static magnetic perturbations, which are caused by the slight misalignment of external current carrying coils. These perturbations typically have a magnitude of around 10^{-4} times the toroidal field strength at the magnetic axis.

Error field can lead to driven magnetic reconnection, at rational surfaces, in otherwise an tearing stable plasma. The subsequent formation of magnetic islands at these surfaces can severely degrade energy confinement.

Plasma rotation allows for the formation of radially localised shielding currents, at the rational surfaces, which suppress magnetic reconnection. However, residual reconnection leads to the formation of radially localised electro-magnetic

torques which act to brake the plasma rotation. Below a critical threshold perturbation strength (dependent on plasma conditions), the viscous torque can balance the electro-magnetic torque. If the critical threshold is exceeded, rapid braking of the plasma occurs, allowing reconnection to proceed unabated [19].

1.2.6   H-mode

The High confinement mode (H-mode) operating Scenario was discovered in 1982 ([20]). The characteristic feature of the H-mode is the formation of a pressure pedestal just inside the separatrix. The effect of the pressure pedestal is to raise the pressure profile throughout the core plasma as compared to the Low confinement mode of operation (L-mode) (figure 1.8). The formation of the edge pressure pedestal is associated with a decrease in turbulence in this region and a corresponding increase in the radial confinement of particles and energy (transport barrier) ([21]). In general the pedestal will continue to grow, as particles and energy are transported from the core to the plasma edge, until either the steep gradients lead sufficient edge transport to maintain equilibrium or an instability occurs which results in the sudden ejection of particles and energy from the edge plasma. An instability of this type commonly observed in H-mode plasmas is the Edge Localised Mode (ELM) [22], [23].

1.2.7   Edge Localised Modes (ELMs)

Edge Localised Modes (ELMs) are repetitive eruptions of particles and energy which occur in some high confinement mode plasmas ([24]). The eruption itself typically occurs over a time period of $< 1ms$ (in ITER $500\mu s$ predicted ([25])) and can release several of the plasma stored energy (in ITER $500MJ$ energy release predicted for large ELMs [26]) . The release of particles and energy causes a partial collapse in the edge pressure profile. The edge pressure gradient slowly (compared to the ELM crash) builds again until the Peeling-Ballooning stability limit is reached, at which point another ELM occurs.

Energy and particles released during the ELM typically stream down field lines and are predominately deposited on the divertor plates. An ELM event can be inferred by spikes on a D_α trace (figure 1.10). Diagnostics are placed around
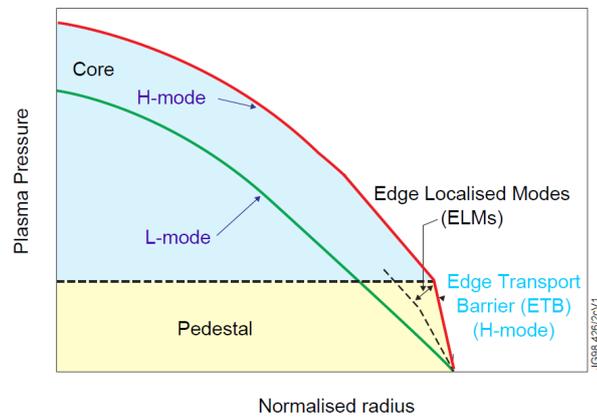
Figure 1.8: The H-mode and L-mode typical pressure profiles [image courtesy of EFTA-JET]

.
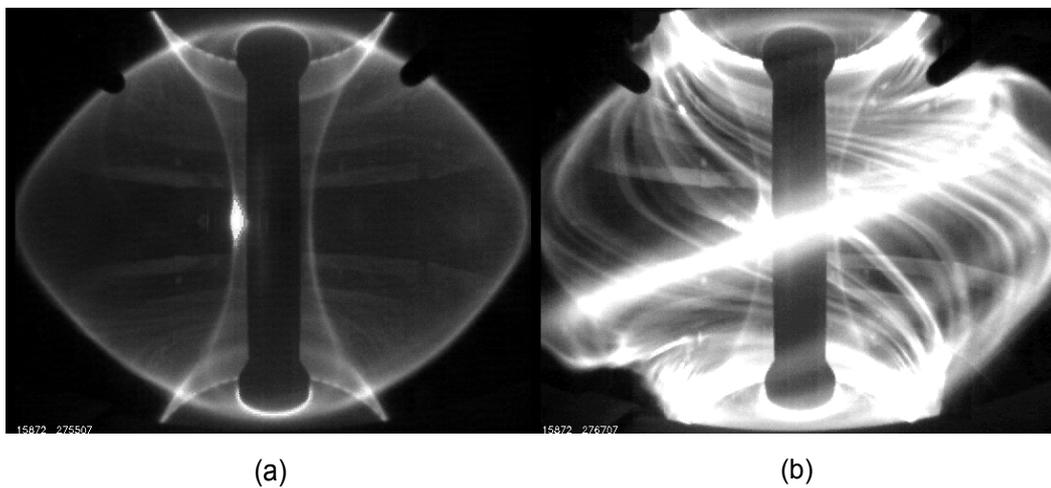
Figure 1.9: (a) Inter ELM H-mode in MAST. (b) An ELM eruption in MAST ([27])

.

the divertor plates which measure the D_α light emitted predominately by the interaction of electrons with neutral particles . The number of such interaction events is greatly increased with the increased particle flux to the divertor plates following an ELM.

Dalpha Divertor
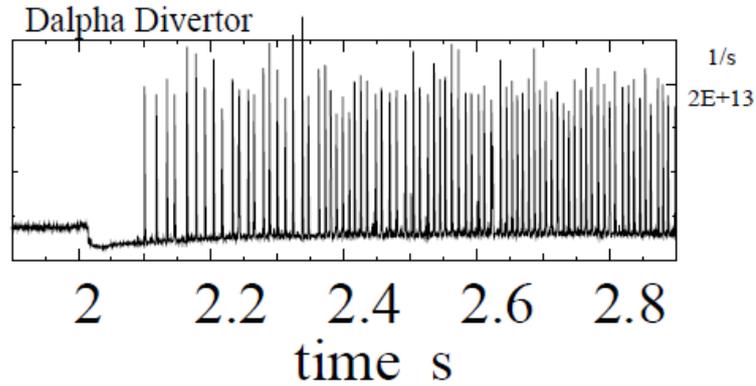
Figure 1.10: A D_α trace, the spikes indicating when an ELM occurs [28]

.

It is experimentally observed that the energy released during large type 1 ELMs decreases as the ELM frequency increases (figure 1.11(a)). It has been observed in the MAST tokamak that this trend occurs in such a way as to keep the average energy released by ELMs, over many ELM cycles, approximately constant (figure 1.11(a) red line). It has also been observed that the natural ELM frequency tends to decrease with the plasma current (figure 1.11(b)).

For current machines the power loads delivered to the divertor plates during an ELM do not pose a serious problem. However, extrapolations to the ITER tokamak suggest that the divertor lifetime maybe reduced below acceptable levels if the plasma current is raised above $I_p = 8MA$. The $Q = 10$, demonstration case is predicted to have a plasma current of $I_p = 15MA$.

A possible solution to the problem is to find a mechanism by which the ELM frequency can be increased whilst maintaining the same plasma current. Figure 1.12 (left) displays the required ELM frequency increase to maintain the energy release per ELM at the natural $I_p = 8MA$ level (This assumes the product $\Delta W_{ELM} f_{ELM}$ still remains approximately constant). For the ITER $I_p = 15MA$ scenario the ELM frequency must be increased above that of the natural ELM
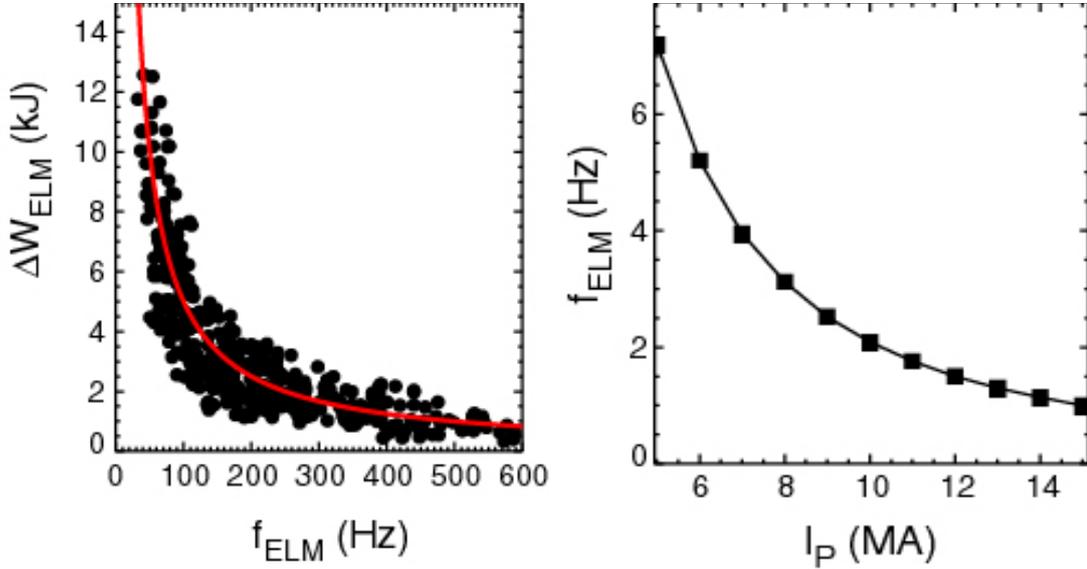
Figure 1.11: (a) frequency of type 1 ELMs with plasma current. (b) required ELM frequency to have little damage at Plasma Facing Components (PFC) [27]

.

frequency by a factor of around 60.

ELMs provide a natural way for particles to be transported out of the plasma. ELMs can therefore be used as a mechanism for transporting impurities out of the plasma. The blue line in figure 1.12(right) provides the predicted ELM frequency required to prevent a build up of Tungsten, which is the divertor material in contact with the plasma. The larger of the red and blue curves provide the desired ELM frequency for a particular plasma current.

1.2.8 Resonant Magnetic Perturbations (RMPs)

Resonant Magnetic Perturbations are non-toroidally symmetric magnetic perturbations applied to plasmas via coil sets external to the plasma. It has been successfully demonstrated that RMPs, applied to ELMing plasmas, can mitigate or even completely suppress ELMs under a number of operating conditions and on different machines (Type 1 ELM mitigation or suppression has been demonstrated on MAST, KSTAR, JET, AUG, and DIII-D (figure 1.13)).
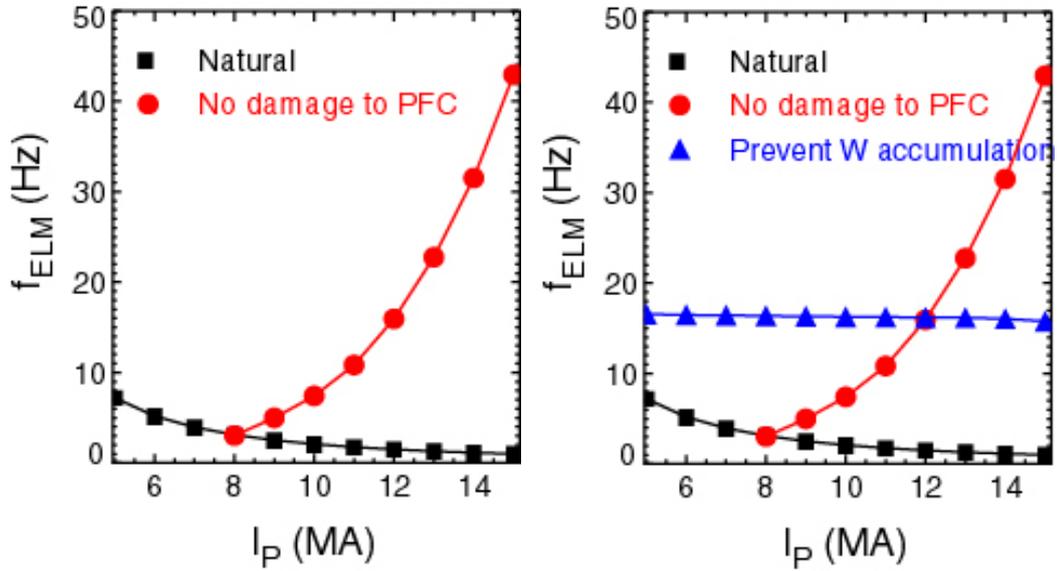
Figure 1.12: (left) frequency of type 1 ELMs with plasma current. (right) required ELM frequency to have little damage at Plasma Facing Components (PFC) [27] .
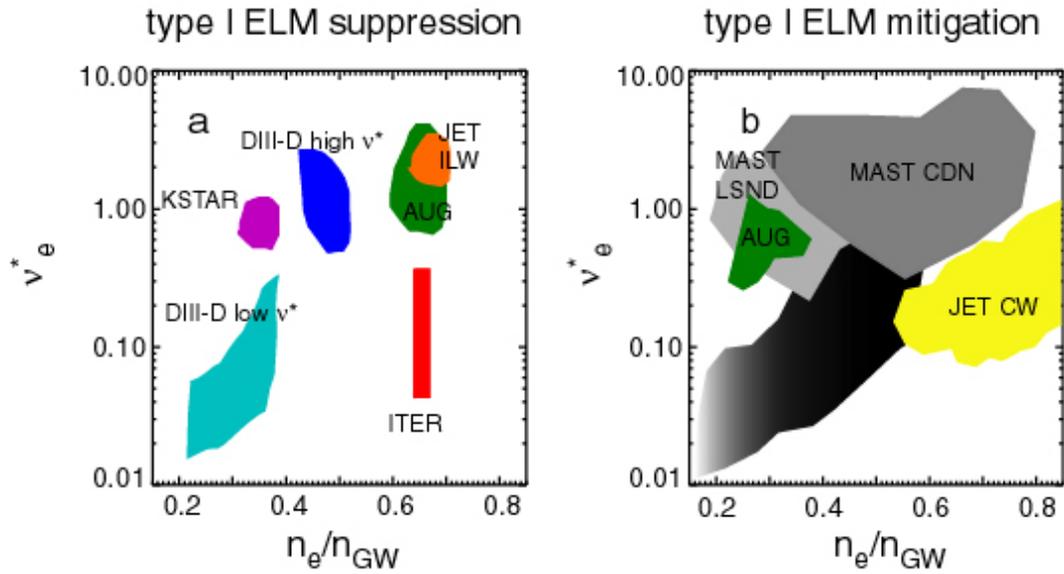
Figure 1.13: Operational space for a number of machines in which type 1 ELM suppression/mitigation has been achieved [27]

The term 'ELM mitigation' is used to describe plasmas in which the application of the coils increases the ELM frequency whilst reducing the energy released per ELM. The term 'ELM suppression' is used when the application of the coils completely stops ELMs from occurring. A D_α trace at the divertor plate indicates the presence of an ELM by a sudden spike. Three such D_α traces are shown in figure (1.14). Trace (c) has no RMPs applied and is typical of an H-mode ELMing plasma trace on DIII-D. Trace (b) is a mitigated case, whilst trace (a) is an ELM suppressed case.
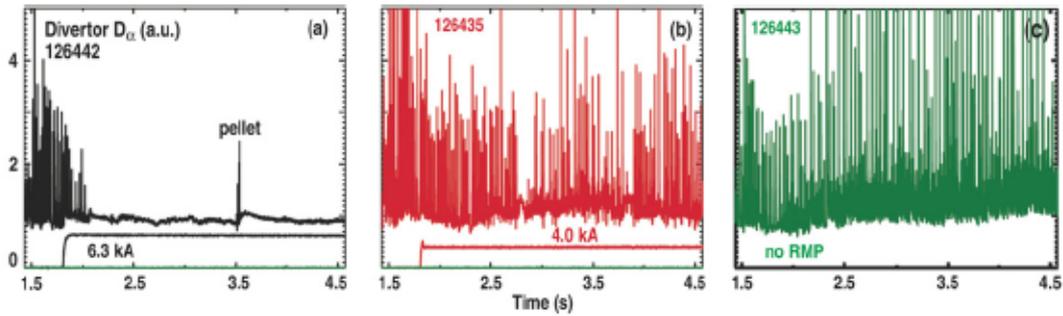
Figure 1.14: A D_α trace in the DIII-D tokamak, the spikes indicating the presence of ELMs. (a) An ELM suppressed case (6.3kA rmp coil current), (b) An ELM mitigated case (4.0kA rmp coil current), (c) A typical case with no RMPs applied

An example of the coil sets used for applying RMPs is displayed for the Mega Amp Spherical Torus (MAST) in figure 1.15. The magnetic perturbation can be Fourier decomposed in the geometric toroidal angle. A magnetic perturbation of fundamental period p is typically referred to as an n = p coil current configuration.

When a particular axi-symmetric equilibrium profile is known before the ELM coils are applied, a coordinate transform may be applied such that the equilibrium field lines appear as straight lines in the new coordinate system. The magnetic perturbations may then be displayed as a double Fourier decomposition in the angle coordinates. An amplitude spectrum is a useful way of displaying the decomposition of the component of the perturbed magnetic field normal to the flux surface (figure 1.16). The change in amplitude is shown as a function of a flux coordinate and poloidal mode number for the fundamental toroidal mode number. The amplitude of the higher poloidal mode numbers tend to decrease fastest
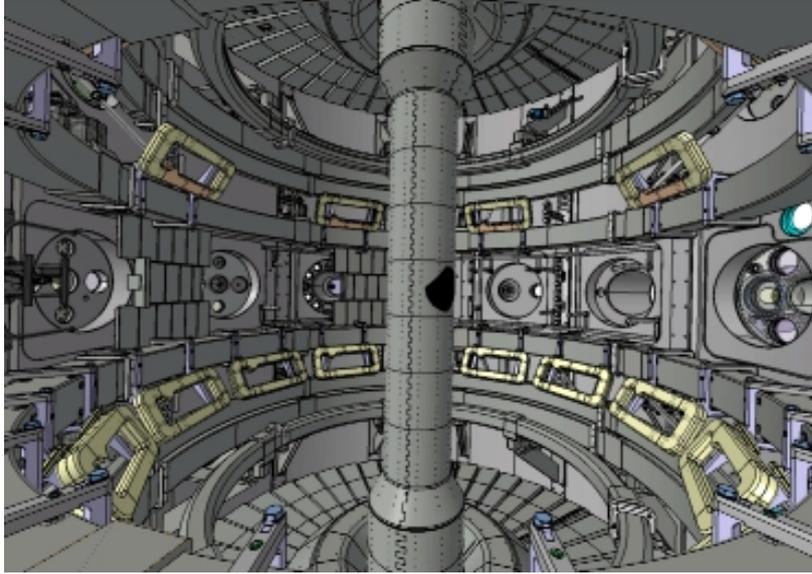
Figure 1.15: The inside of the MAST tokamak displaying a number of its ELM coils ([29])

when moving from the plasma edge towards the central plasma. Locations of the rational surfaces are also displayed to indicate whether the vacuum perturbation is well 'pitch aligned' with the equilibrium field. A spectrum is deemed to have good 'pitch alignment' if high amplitude harmonics line up with the rational surface locations.

A number of experimental observations have been made when RMPs are applied. The effects the RMPs have on the plasma can broadly be split into high and low collisionality cases. This document will only consider the low collisionality observations.

1.2.8.1 low collisionality observations

Low collisionality ELM suppression and mitigation have been achieved on the DIII-D machine for both $n = 3$ and $n = 2$ coil configurations. In this section the focus is on ELM suppression but mitigation results are included where relevant. RMPs are applied to the plasma in the DIII-D machine through 2 different sets of coils, the I-coils and the C-coils (figure 1.17).
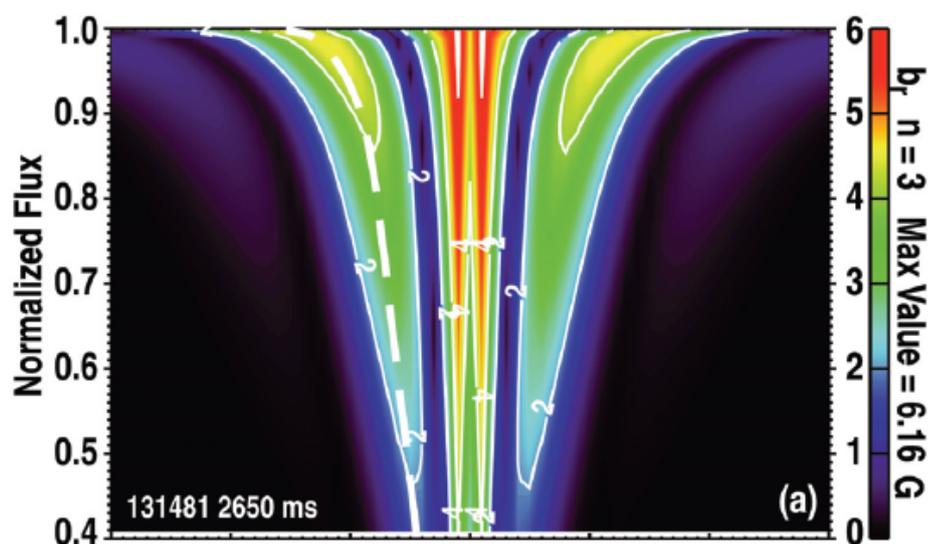
Figure 1.16: n = 3 amplitude spectrum displaying how the vacuum poloidal harmonics change in flux space. The dashed line shows the q value as a function of normalised flux [30]
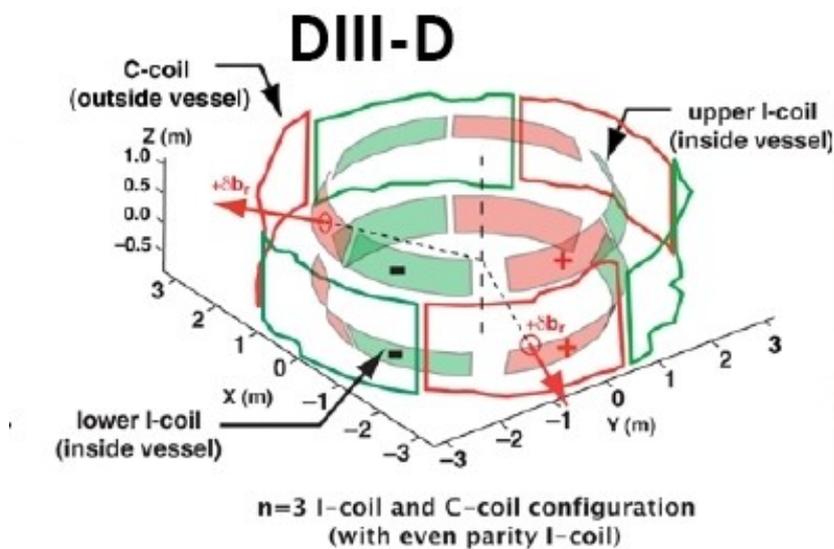
Figure 1.17: The DIII-D C coil and I coil set [30]

It is reported ([31], [32]) that ELM suppression has been achieved for edge electron collisionalities $\nu_e^* < 0.35$, and no observation thus far has been observed above this "threshold". The pedestal collisionality is typically raised by an increase in the edge density (figure 1.18).
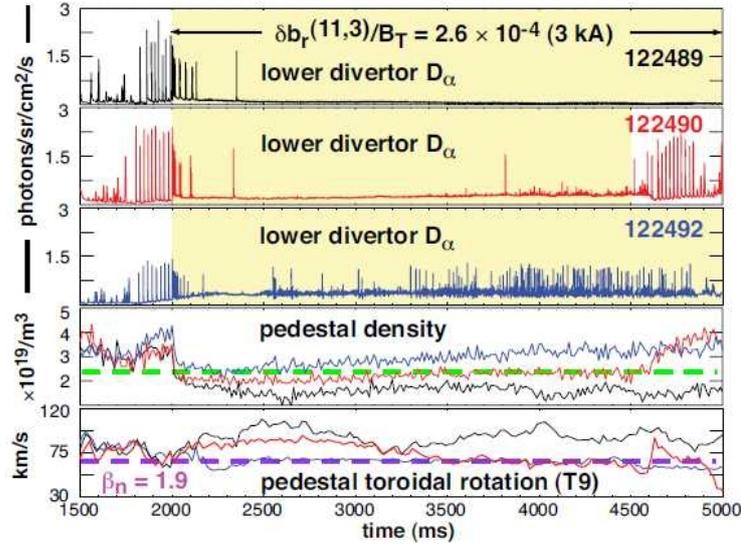
Figure 1.18: An apparent density threshold for ELM suppression in the low collionallity regime on the DIII-D tokamak [33]. The yellow regions correspond to RMPs switched on.

Another access condition for ELM suppression is that the Neutral Beam Injection (NBI) must be applied in the same direction as the plasma current (Co-NBI as oppose to Counter-NBI). This condition implies that there will exist a position (generally close to the plasma edge) at which the perpendicular electron rotation will be zero (figure 1.19).

Both mitigation and suppression are accompanied with changes in both the temperature and density profiles. Figure 1.20 provides a typical example. The density profile is lowered across the entire plasma, a phenomenon commonly referred to as "density pump out". The electron temperature profile is not so drastically affected. Its peaked value in the pedestal region is typically raised slightly helping to maintain a relatively steep pressure gradient close to the plasma edge.
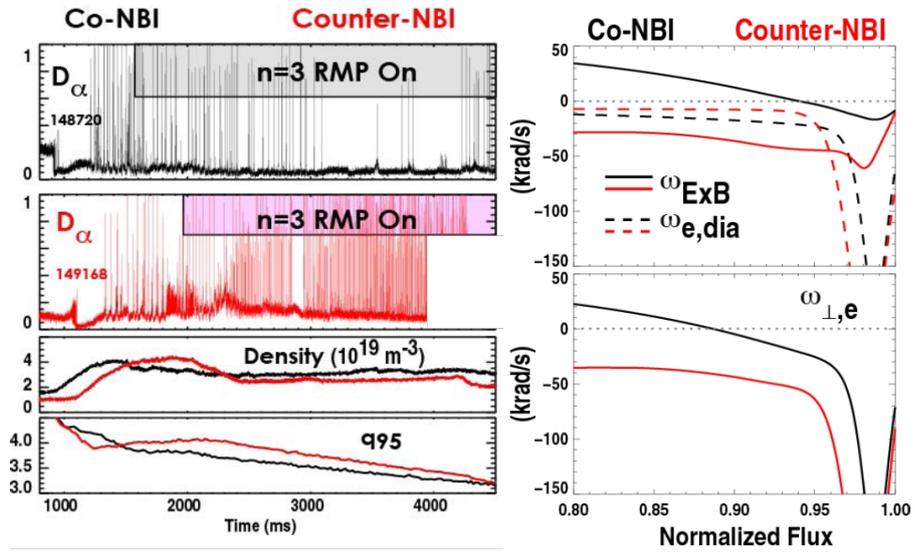
Figure 1.19: A demonstration that ELM suppression requires a surface of $\omega_{\perp e} = 0$ [34]
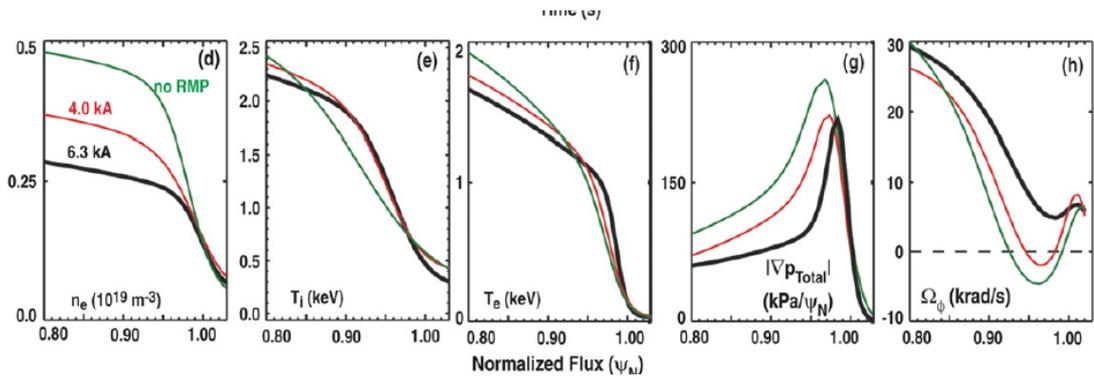
Figure 1.20: temperature, density, pressure and velocity profiles with coil currents 0.0kA (green), 4.0kA (red), 6.3 kA (black) [35]

Systematic studies have been carried out on the effect of altering the q-profile. It is observed that by maintaining the same applied perturbation strength and spectrum, and slowly ramping the edge q-profile that "windows of suppression" are present (figure 1.21). The q value quoted is typically that at the 0.95 position in the normalised flux coordinate, q_{95}. The size of the "suppression windows" increases as the amplitude of the perturbation increases. q_{95} scans have been performed by two methods, By ramping the plasma current, and by ramping the toroidal field strength. The size and location of the "windows" is seen to change depending on the ramping method (figure 1.22). It is also worth noting that if a q_{95} scan is started outside the suppression window, the mitigated ELM frequency increases as the suppression window is approached (figure 1.23).
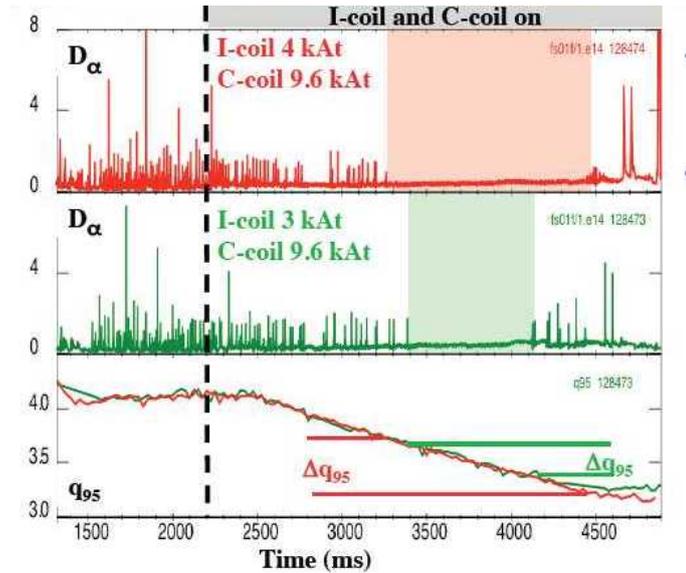
Figure 1.21: q_{95} windows in the DIII-D tokamak, demonstrating an increased window width with increasing perturbation strength [31]

Experiments have also been carried out maintaining the same plasma profile, but varying the coil sets used to apply the perturbation. In effect the applied perturbation spectrum is changed. In these experiments the spectrum was altered by applying the upper I-coils, lower I-coils and C-coils separately. In addition both I-coils where then applied together. The experiment demonstrated that the threshold perturbation amplitude for attaining suppression is highly dependant
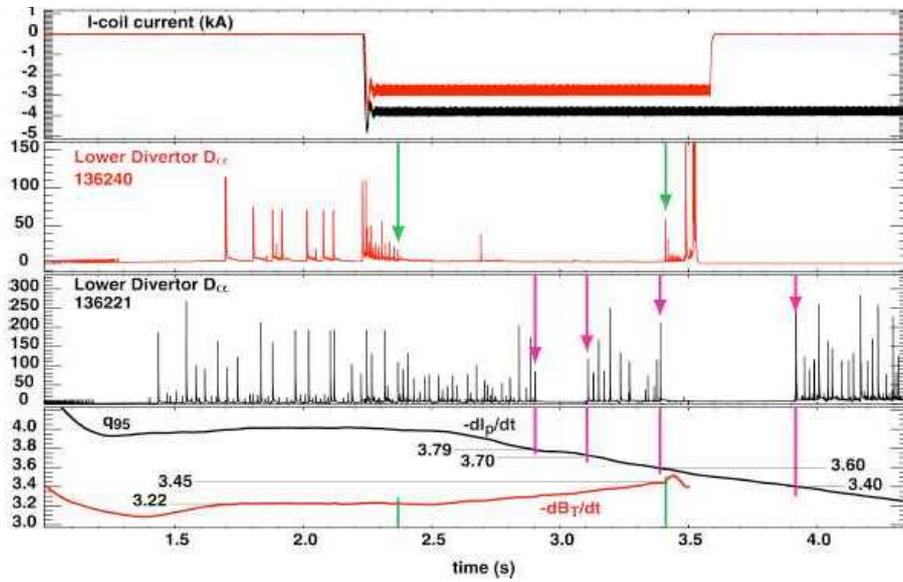
Figure 1.22: q windows displaying differing window size depending on the ramping method [27]
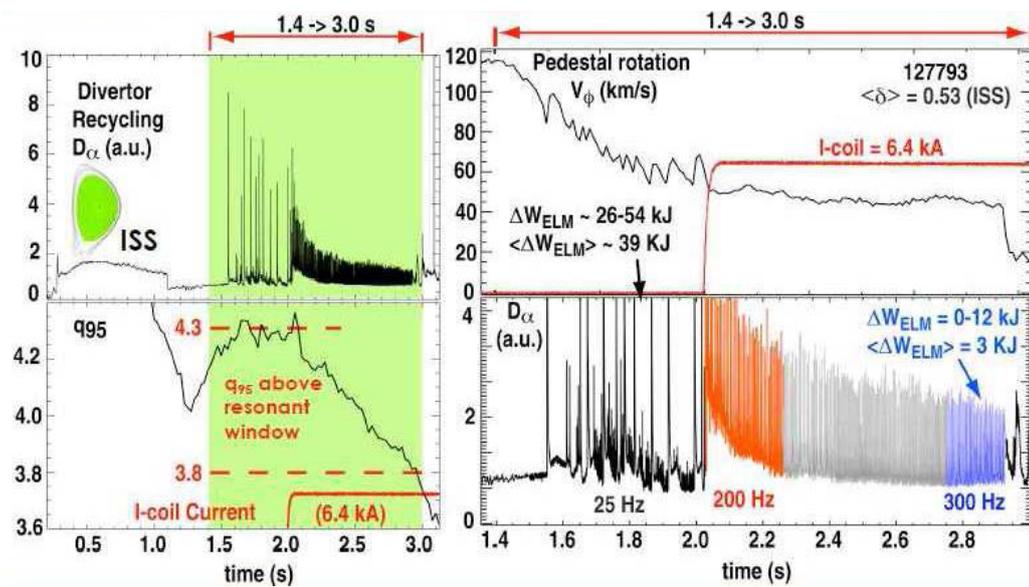
Figure 1.23: ELM frequency increase during a q_{95} scan as the suppression window is approached [27]

on the applied spectrum. The results are outlined in figure 1.24.
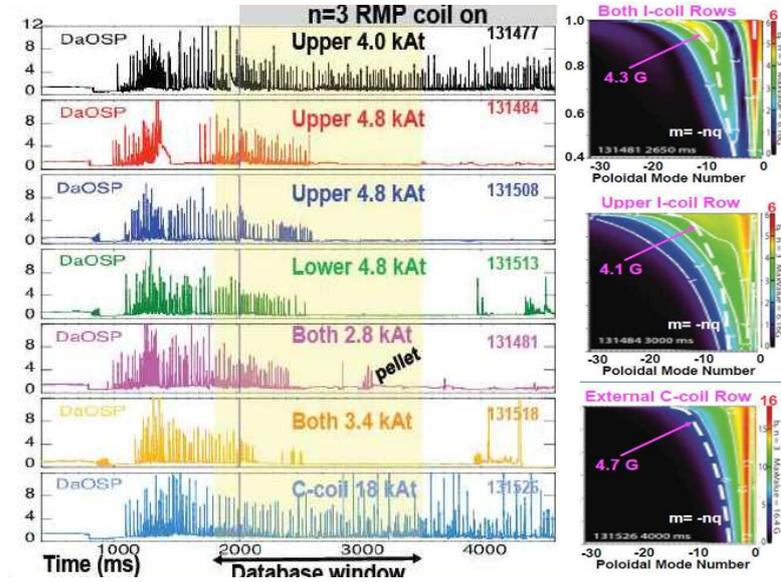
Figure 1.24: Results from the DIII-D tokamak demonstrating that suppression is dependent on the applied spectrum, and not only the perturbation amplitude [36]

1.2.9 The Fluid Model

The following section is presented to aid with conceptual insight rather than for mathematical rigour (i.e. definitions are used loosely). A fluid is made up of a collection of particles in space. A small volume at position $\mathbf{x}$ will contain a number of particles, each particle having a particular velocity. The particles in the volume in real space can be further categorised into small volumes in velocity space, each volume associated with a small range of velocities about a particular velocity, $\mathbf{v}$. The distribution density function, $f(\mathbf{x}, \mathbf{v}, t)$ is defined such that the product $f(\mathbf{x}, \mathbf{v}, t)d^3x d^3v$ is the number of particles, contained in a small region of real space and a small region of velocity space located at points $\mathbf{x}$ and $\mathbf{v}$ respectively.

The fluid density, $n(\mathbf{x}, t)$, is defined such that the product, $n(\mathbf{x}, t)d^3x$ is the total no of particles contained in the small volume of real space at point $\mathbf{x}$ at

time t.

$$n(\mathbf{x}, t) = \int_{allvelspace} f(\mathbf{x}, \mathbf{v}, t) d^3v \tag{1.17}$$

Next consider the surface element, $d\mathbf{a}$, at position $\mathbf{x}$.

The number of particles with a small distribution of velocities about $\mathbf{v}$ (i.e. those in d^3v), passing through $d\mathbf{a}$ per unit time is given by:

$$f(\mathbf{x}, \mathbf{v}, t) d^3v \mathbf{v} \cdot d\mathbf{a} \tag{1.18}$$

These particles carry momentum and kinetic energy such that, the momentum and kinetic energy passing though $d\mathbf{a}$ per unit time by these particles is

$$m\mathbf{v} f(\mathbf{x}, \mathbf{v}, t) d^3v \mathbf{v} \cdot d\mathbf{a} \tag{1.19}$$

$$\frac{1}{2} m v^2 f(\mathbf{x}, \mathbf{v}, t) d^3v \mathbf{v} \cdot d\mathbf{a} \tag{1.20}$$

respectively.

The fluid velocity, $\mathbf{V}(\mathbf{x}, t)$, is defined such that the product $n\mathbf{V}(\mathbf{x}, t) \cdot d\mathbf{a}$ is equal to the total particle flux passing through $d\mathbf{a}$ (The direction of $d\mathbf{a}$ is arbitrary).

$$\mathbf{V}(\mathbf{x}, t) = \frac{1}{n} \int_{allvelspace} \mathbf{v} f(\mathbf{x}, \mathbf{v}, t) d^3v \tag{1.21}$$

The stress tensor, $\overleftrightarrow{P}(\mathbf{x}, t)$, and energy flux density, $\mathbf{Q}(\mathbf{x}, t)$, are defined such that the products $\overleftrightarrow{P}(\mathbf{x}, t) \cdot d\mathbf{a}$ and $\mathbf{Q}(\mathbf{x}, t) \cdot d\mathbf{a}$ equal the total momentum flux and kinetic energy flux passing though $d\mathbf{a}$.

$$\overleftrightarrow{P}(\mathbf{x}, t) = \int_{allvelspace} m(\mathbf{v} \otimes \mathbf{v}) f(\mathbf{x}, \mathbf{v}, t) d^3v \tag{1.22}$$

$$\mathbf{Q}(\mathbf{x}, t) = \int_{allvelspace} \frac{1}{2} m v^2 \mathbf{v} f(\mathbf{x}, \mathbf{v}, t) d^3v \tag{1.23}$$

(Note: the dyadic tensor is defined such that $(\mathbf{a} \otimes \mathbf{b}) \cdot \mathbf{c} = \mathbf{a}(\mathbf{b} \cdot \mathbf{c})$). It is

also worth pointing out that the vector $\overleftrightarrow{P}(\mathbf{x}, t) \cdot d\mathbf{a}$ has a component normal and tangent to the surface element signifying the momentum transfer rate in these directions.

The distribution function, for a particular species, will evolve over time.

$$\frac{\partial f_s}{\partial t} + \mathbf{v}_s \cdot \nabla f_s + \mathbf{a}_s \cdot \nabla_v f_s = C_s(f) \tag{1.24}$$

$$\mathbf{a}_s = \frac{e_s}{m_s}(\mathbf{E} + \mathbf{v}_s \times \mathbf{B}) \tag{1.25}$$

Fluid evolution equations, for each species, can be obtained by considering the various moments of equation 1.24 in velocity space. The fluid equations are more intuitive in their integral from, and the following are presented considering an arbitrary fixed volume, V, in real space which is bounded by a surface S.

$$\underbrace{\frac{d}{dt}\int_V n_s d^3 x}_{(1)} =$$

$$\underbrace{- \oint_S n_s \mathbf{V}_s \cdot \overrightarrow{da}}_{(2)} \tag{1.26}$$

$$\underbrace{\frac{d}{dt}\int_V m_s n_s \mathbf{V}_s d^3 x}_{(3)} =$$

$$\underbrace{- \oint_S \overleftrightarrow{P}_s \cdot d\mathbf{a}}_{(4)} + \underbrace{\int_V e_s n_s (\mathbf{E} + \mathbf{V}_s \times \mathbf{B}) d^3 x}_{(5)} + \underbrace{\int_V \mathbf{F}_s d^3 x}_{(6)} \tag{1.27}$$

$$\underbrace{\frac{d}{dt}\int_V (\frac{3}{2}p_s + \frac{1}{2}m_s n_s V_s^2) d^3 x}_{(7)} =$$

$$\underbrace{- \oint_S \mathbf{Q}_s \cdot d\mathbf{a}}_{(8)} + \underbrace{\int_V e_s n_s (\mathbf{E} \cdot \mathbf{V}_s) d^3 x}_{(9)} + \underbrace{\int_V (W_s + \mathbf{F} \cdot \mathbf{V}_s) d^3 x}_{(10)} \tag{1.28}$$

The scalar pressure, p_s, is associated with the kinetic energy of the particles as seen by an observer travelling with the fluid velocity. Terms $1 - 10$ can be described as follows:

1. The total rate of change of particles in V.

2. The rate of particle outflow through S.

3. The rate of change of momentum in V.

4. The rate of momentum outflow through S.

5. The rate of momentum transfer from electro-magnetic body forces.

6. The rate of momentum transfer through collisions with other species.

7. The rate of change of particle kinetic energy in V.

8. The rate of outflow of energy through particle passing through S.

9. The rate of work done on V by electro-magnetic forces.

10. The rate of energy transfer through particle collisions with other species.

Two contributions to the fluid flow perpendicular to the field lines are of particular importance. These are the $\mathbf{E} \times \mathbf{B}$ and diamagnetic velocities. The former has its origin in the single particle $\mathbf{E} \times \mathbf{B}$ drift and maintains the same form:

$$\mathbf{V}_{\perp s} = \frac{\mathbf{E} \times \mathbf{B}}{B^2} \tag{1.29}$$

The flow again being the same magnitude and direction for both electrons and ions and so does not contribute to the plasma current.

The diamagnetic flow is an apparent flow associated with the relative motion of particle orbits across a pressure gradient.

$$\mathbf{V}_{\perp s}^{Dia} = \frac{\nabla p_s \times \mathbf{B}}{e_s n_s B^2} \tag{1.30}$$

The relative motion of charge species caused by diamagnetic flow lead to the formation of a perpendicular diamagnetic current.

$$\mathbf{J}_{\perp}^{(Dia)} = \frac{\nabla(p_i + p_e) \times \mathbf{B}}{B^2} \tag{1.31}$$

(quasi-neutrality is assumed in the above form $n_i \approx n_e$)

1.2.10 Document summary

Chapter 2 begins with a summary of linear layer physics. The model is built in an intuitive way so the effects of additional terms are clear, and also to reflect the layout of the results presented in chapter 3. The chapter begins with a summary of linear reconnection dynamics. Forced reconnection dynamics is then considered as a natural progression. The dynamics are initially discussed with zero equilibrium flow. The effects of equilibrium flow are then included with particular attention paid to the amount reconnection flux in the final equilibrium state. The inclusion of viscosity raises the order of the coupled differential equations and the four linear regimes are presented. The inclusion of non-linear terms gives rise to a net localised $\mathbf{J} \times \mathbf{B}$ force at the rational surface. Section 2.1.9 discusses possible equilibrium states when the $\mathbf{J} \times \mathbf{B}$ and viscous force balance in quasi-linear regimes. Finally, the effect diamagnetic terms have on linear regime resonances and the corresponding electromagnetic torques are presented in section 2.1.10.

In chapter 3 the results of testing the BOUT++ code against reconnection type problems and linear layer physics are presented. The code linear reconnection dynamics are tested against various analytic scalings. The reconnection problem considered is used to test the amount of radial grid packing required to produced accurate results in the layer. This is the first time such an analysis has been considered for reconnection type problems in the presence of RMPs. The regimes and parameters which determine minimum amount of grid packing are considered. Equilibrium flow is added and the final reconnected states are tested in the so called constant ψ regimes, particular emphasis being placed on the importance of getting the boundary conditions implemented in the correct way to avoid sheet current between the boundary and internal grid cells.

Chapter 4 develops a simplified multi-surface model which is a hybrid be-

tween tokamak and induction motor physics. The equilibrium points and various bifurcation scenarios for a two layer model are discussed for two different cases. Initially the electromagnetic torques act in the same direction, each surface acting to slow the fluid rotation at the other. The second case involves introducing a diamagnetic off-set so that the surface brakes towards the zero in the electron rotation. Particular attention is place on analysis around the region in which the electron rotation is zero, this being a necessary condition for ELM suppression. This is the first possible equilibrium state and bifurcation analysis has been carried out in this region. The bifurcation dynamics of moving a single surface over the position of the $\omega_{\perp e} = 0$ location is discussed. Then the bifurcation scenarios of two surfaces straddling the location of $\omega_{\perp e} = 0$ are presented. These results suggest the bifurcation windows exist as the radial locations of these surfaces are incrementally changed relative to the position of the location at which $\omega_{\perp e} = 0$. These bifurcation windows are shown to have the same qualitative features as the q_{95} windows seen in the DIII-D experiments. In addition the unique shape of what will be call 'ψ space' will be shown to provide a possible explanation for the range of penetration threshold seen in DIII-D experiments.

In chapter 4 the hypothesis is put forward that a bifurcation may occur in either one of the surfaces straddling the $\omega_{\perp e}$ before ELM suppression is observed. The results of chapter 4 are compared with the results of low collisionallity DIII-D experiments. The validity of the hybrid model and the hypothesis is discussed and further work is proposed.

Chapter 2

Singular Surface Theory

2.1 Theory

The interpretation of the experimental results of RMP experiments, and the design of the RMP coils on ITER, have relied heavily on the magnetic chaos model. In this model the RMPs create overlapping magnetic islands which lead to regions of magnetic chaos. Radial transport is increased in these regions reducing pedestal gradients, consequently leading to ELM stability.

The formation of lobe structures at the separatrix [37] (figure 2.1) and strike point splitting at the divertor plates [38] are in agreement with the presence of magnetic chaos in the edge plasma.

The vast majority of chaos modelling estimates the size of the magnetic islands by adding the vacuum magnetic perturbations to an equilibrium magnetic field, neglecting the response of the plasma to the applied field. Indeed these models greatly over estimate the size of the lobe structures, and ad hoc screening currents must be applied in the plasma to observe similar sizes of lobe structures in the vacuum model.

Two fluid modelling [39], and theory [40] [41], indicate that electron rotation perpendicular to the magnetic field acts to screen the applied perturbation. The steep pressure gradients in the pedestal region give rise to diamagnetic flows which may exceed the $\mathbf{E} \times \mathbf{B}$ flows in this region. Modelling indicates that islands throughout most of the pedestal region are strongly suppressed [39], making it
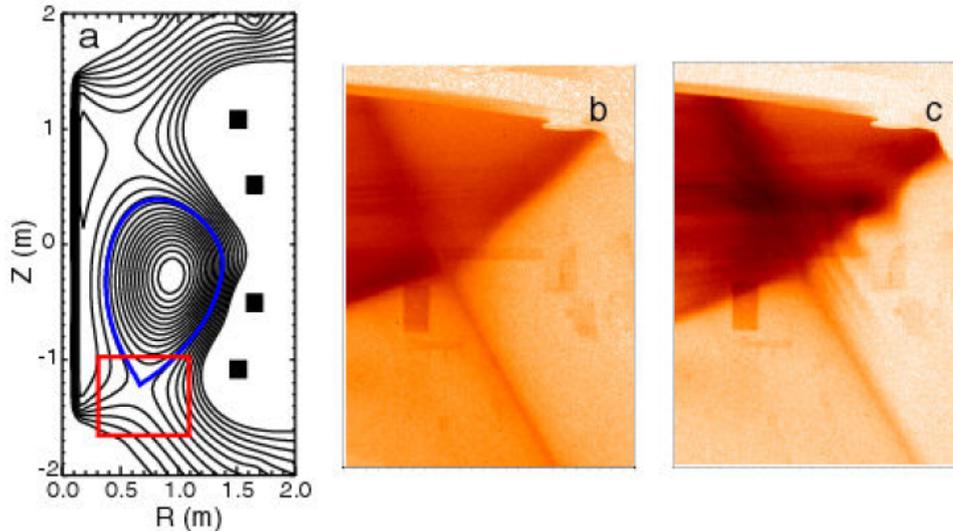
Figure 2.1: (a) poloidal cross-section of the MAST plasma showing region of the camera view. An inter-ELM H-mode plasma with (b) no RMPs applied, (c) RMPs applied demonstrating the formation of lobe type structures [37].

unlikely for magnetic chaos to exist in this region without adjacent surfaces undergoing lock mode bifurcations, which, if occurring in the pedestal would be predicted to cause a transition back to L-mode. The foot of the pedestal region may be an exception to this case [40].

A further region of interest exists in plasmas which exhibit a surface at which the perpendicular electron rotation is zero. The surface usually exists at a radius less than that of the pedestal region. Both modelling and theory predict that screening is much reduced in the neighbourhood of this surface.

2.1.1 The low frequency shear Alfven wave in a homogeneous plasma

The large number of variables associated with the two fluid equations, coupled with complicated geometry, lead to difficulties in the identification of physical phenomenon and in the interpretation of results. It is useful to attempt to reduce the equation set used by identifying temporal and spatial scales of importance.

The temporal scale used for the model equations in section 2.1.3 is that associated with the shear Alfven wave.

The shear Alfven wave is associated with the restoring force exerted by the bending of magnetic field lines (magnetic tension). The simplest description of the wave is gained by considering a homogeneous plasma which is infinite in extent and an equilibrium magnetic field of the form $\mathbf{B} = B_0 \hat{\mathbf{e}}_z$. A small amplitude perturbation is considered (allowing for linearisation of the equations) of the form $f_1(\mathbf{x}, t) = \tilde{f}_1 exp(i(\mathbf{k} \cdot \mathbf{x} - \omega t + \gamma))$. The wave vector, $\mathbf{k}$, will be assumed parallel to the equilibrium magnetic field, $\mathbf{k} = k_{\parallel} \hat{\mathbf{b}}_0$, and ω is the temporal frequency.

By consideration of the cold plasma, $T = 0$, momentum equations, the perpendicular fluid velocities of both species are given by [42]:

$$\mathbf{V}_{1\perp s} = -\frac{i\omega}{(\Omega_{cs}^2 - \omega^2)} \frac{e_s}{m_s} \mathbf{E}_{1\perp} + \frac{\Omega_{cs}^2}{(\Omega_{cs}^2 - \omega^2)} \frac{\mathbf{E}_{1\perp} \times \mathbf{B}_0}{B_0^2} \qquad (2.1)$$

For the particular case of interest the following ordering shall be adopted, $\omega/\Omega_i \ll 1 \ll \Omega_e/\Omega_i$. With this ordering the ordinary $\mathbf{E} \times \mathbf{B}$ velocity dominates the $\perp$ motion for both species, which to leading order is the same for both species and so does not contribute to the perturbed current density, $\mathbf{J}_1 = \Sigma n_0 e_s \mathbf{V}_{1s}$. However of the polarization velocities (1st term in equation 2.1) the ion polarization velocity dominates, contributing the leading order current density. Examination of ion polarisation velocity and the form for the current density leads to the realization that the conductivity, σ, will, to leading order, be a scalar as oppose to its more general tensor form (i.e. the relationship between the current density and the electric field is $\mathbf{J}_1 = \sigma \mathbf{E}_1$), with scalar conductivity given by:

$$\sigma = -i\epsilon_0 \omega \frac{\Omega_{pi}^2}{\Omega_{ci}^2} \qquad (2.2)$$

$$\Omega_{pi}^2 = \frac{ne^2}{\epsilon_0 M_i} \qquad (2.3)$$

Ω_{pi} being the ion plasma frequency. Using Faraday's Law, the extended Ampere's Law:

$$\frac{\partial \mathbf{B}_1}{\partial t} = \nabla \times \mathbf{E}_1 \tag{2.4}$$

$$\mu_0 \epsilon_0 \frac{\partial \mathbf{E}_1}{\partial t} = -\mu_0 \mathbf{J}_1 + \nabla \times \mathbf{B}_1 \tag{2.5}$$

$$\tag{2.6}$$

and that $\mathbf{k} \cdot \mathbf{E}_1 = 0$, an expression for the perturbed electric field can be derived.

$$(\frac{\omega^2}{c^2}(1 + \frac{\Omega_{pi}^2}{\Omega_{ci}^2}) - k_\parallel^2)\mathbf{E}_1 = \mathbf{0} \tag{2.7}$$

The non-trivial solution leads to the dispersion relation (using $\Omega_{pi}^2/\Omega_{ci}^2 \gg 1$):

$$\omega^2 = \frac{(k_\parallel V_A)^2}{(1 + V_A^2/c^2)} \approx (k_\parallel V_A)^2 \tag{2.8}$$

$$V_A = c\frac{\Omega_{ci}}{\Omega_{pi}} = \frac{B_0}{\sqrt{\mu_0 n_0 m_i}} \tag{2.9}$$

Equation 2.8 is the desired form for the temporal frequency. V_A is the Alfven speed. In this low frequency limit the shear Alfven waves are plane polarised waves [42].

2.1.2 The Shear Alfven Law

Many of the concepts described in this chapter may be derived from the single fluid Magneto Hydro-Dynamic (MHD) equations. This provides a much simpler equation set to work with than the two fluid set. For a mixture of clarity and for ease of presenting many of the results in chapter 3, the simplest equation set for describing phenomena will be used, then additional terms will be added where needed. The derivations are not intended to be rigorous, rigorous reductions can be found elsewhere. Reductions of the two fluid equations to the MHD equations can be found in a number of texts [43], [44].

The shear Alfven law is a useful starting point in the analysis of many common plasma instabilities, and is a fundamental part in the analysis which follows. The

stating point for its derivation is the single fluid momentum equation [43].

$$\rho\frac{d\mathbf{V}}{dt} + \nabla \cdot \overleftrightarrow{\Pi} = -\nabla P + \mathbf{J} \times \mathbf{B} \tag{2.10}$$

with $\overleftrightarrow{\Pi}$ denoting the viscous tensor and $d/dt = \partial/\partial t + \mathbf{V}\cdot\nabla$ the total derivative. Following the notation used in [43], $\mathbf{f}$ is used to encompass both the inertial and viscous contributions (the 1st and 2nd terms of the l.h.s. of 2.10 respectively).

$$\mathbf{f} = \rho\frac{d\mathbf{V}}{dt} + \nabla \cdot \overleftrightarrow{\Pi} \tag{2.11}$$

Making use of the following:

$$\mathbf{B} \cdot \nabla \times (\mathbf{J} \times \mathbf{B}) = B^2\mathbf{B} \cdot \nabla(\frac{J_\parallel}{B}) - \frac{1}{B^2}\mathbf{B} \times (\mathbf{J} \times \mathbf{B}) \cdot \nabla_\perp B^2 \tag{2.12}$$

$$\mathbf{J} \times \mathbf{B} = \frac{B^2}{2\mu_0}\vec{\kappa} - \nabla_\perp(\frac{B^2}{2\mu_0}) \tag{2.13}$$

(the quantity $\vec{\kappa} = \hat{\mathbf{b}} \cdot \nabla\hat{\mathbf{b}}$ being the magnetic field line curvature) and taking $\mathbf{B} \cdot \nabla\times$ of equation 2.10, the shear Alfven Law may be derived.

$$\mathbf{B} \cdot (\nabla \times \mathbf{f} + 2\vec{\kappa} \times \mathbf{f}) = B^2\mathbf{B} \cdot \nabla(\frac{J_\parallel}{B}) + 2\mathbf{B} \times \vec{\kappa} \cdot \nabla P \tag{2.14}$$

The right hand side of this equation constitutes the drive terms. The 1st term, associated with current driven modes, can be split into two terms when considering slight departures away from equilibrium.

$$\mathbf{B} \cdot \nabla(\frac{J_\parallel}{B}) \approx \delta\mathbf{B} \cdot \nabla(\frac{J_{\parallel 0}}{B_0}) + \mathbf{B}_0 \cdot \nabla(\frac{\delta J_\parallel}{B_0}) \tag{2.15}$$

The 1st of these terms is commonly referred to as kink term and arises' when gradients in the equilibrium parallel current are present (the 0 suffix is used to denote equilibrium quantities). The second term is known as the line-bending term is associated with the bending of magnetic field lines. The line-bending term is usually stabilizing, but may become small near 'mode rational surfaces'.

The 2nd drive term in equation 2.14 is associated with pressure driven modes and is commonly referred to as the interchange term. The name derives from it

being responsible for the Rayleigh-Taylor instability.

The terms on the left hand side of equation 2.14 are both mainly associated with parallel vorticity evolution and dissipation. This will become clearer in the next section.

2.1.3 The cylindrical zero beta large aspect ratio model

The bending of field lines is accompanied by a restoring force which attempts to straighten them. As a consequence unstable plasma modes are often elongated along field lines, tending to locally resemble flute like corrugations. The use of flux coordinates, (r, θ, ϕ) (coordinates in which the field lines appear as straight lines), allow perturbations in the double periodic system to be Fourier decomposed.

$$f(r, \theta, \phi) = \sum_{m,n} \tilde{f}_{mn}(r) e^{i(m\theta - n\phi)} \tag{2.16}$$

If the perturbation has a particular dominant harmonic, it useful to define the dominant wave vector.

$$\mathbf{k} = m\nabla\theta - n\nabla\phi \tag{2.17}$$

Perturbations are elongated along field lines when the parallel component of the wave vector, $k_\parallel = \mathbf{k} \cdot \hat{\mathbf{b}}$, is small. Specifically searching for such modes the quantity $\epsilon = k_\parallel/k_\perp$ may be utilised as a small parameter to separate scale lengths in a particular region of interest. [43] provides a lengthy analysis utilising the perturbation method of multiple scales (an excellent account of the technique can be found in [45]) to derive the flute reduce MHD equations. The large aspect ratio assumption, $\varepsilon = a/R_0$ with $0 < \varepsilon \ll 1$, may also be used as an expansion parameter. The flute reduction may now hold over the whole plasma region, and the large aspect ratio evolution equations can be obtained by taking the flute reduced terms to this limit. Throughout this document a cylindrical or slab approximation is used. The cylindrical approximation used is very similar to the large aspect ratio, low β, circular cross-section case, and the slab approximation may be used to look at radially localised phenomena whilst further reducing complications arising due to geometry (a good account of obtaining large aspect

ratio equilibria can be found in [17]. The metrics obtained are useful in obtaining further evolution equations. [46] is an account of obtaining evolution equations in this limit). It is useful to outline how a cylindrical set of evolution equations can be derived, with the object of introducing approximations, forms for the operators, and to introduce normalisations.

A number of approximations are used in the following derivation.

- The cylinder is periodic along its axis with a period length of $2\pi R_0$, and the plasma exists in a region $0 \le r \le a$

- The large aspect ratio assumption is used to form an expansion parameter, $0 < \varepsilon \ll 1$.

- Equilibrium quantities are only dependent on r. An orthogonal coordinate system is used, (r, θ, ϕ) with $\phi = z/R_0$ (z is the length coordinate along the axis of the cylinder).

- $q(r) = O(1)$ as $\varepsilon \to 0$

- Equilibrium $B_{0\phi}$ is assumed constant. This is not a requirement but is assumed for simplicity.

- Temporal frequencies will be assumed to be of the order of the shear Alfven time-scale, $\omega = k_{\parallel} V_A \Rightarrow \omega \tau_A = O(\varepsilon)$ as $\varepsilon \to 0$ ($\tau_A = a/V_A$).

- Over bars will be used to denote normalised quantities. Length scales are normalised to the minor radius a ($0 \le \bar{r} \le 1$). The magnetic field is normalised to $B_{0\phi}$.

In light of the temporal frequency assumption the following normalisations are used for time and velocity:

$$\bar{t} = \frac{\varepsilon t}{\tau_A} \qquad \overline{\mathbf{V}} = \frac{\mathbf{V}}{\varepsilon V_A} = O(1) \tag{2.18}$$

As consequence of the condition on the q profile:

$$q(\bar{r}) = \varepsilon \frac{\bar{r}}{\bar{B}_{0\theta}(\bar{r})} \quad \Rightarrow \quad \bar{B}_{0\theta}(\bar{r}) = O(\varepsilon) \tag{2.19}$$

The harmonics that are of interest in the following analysis, are those for which a rational surface exists in the plasma. Consequently $m/n = O(1)$ as $\varepsilon \to 0$ is assumed. This may be used to order the ∇ operator when operating on such a harmonic.

$$
\begin{aligned}
\overline{\nabla} = a\nabla &= \hat{\mathbf{e}}_r \frac{\partial}{\partial \bar{r}} + \hat{\mathbf{e}}_\theta \frac{1}{\bar{r}} \frac{\partial}{\partial \theta} + \hat{\mathbf{e}}_\phi \varepsilon \frac{\partial}{\partial \phi} \\
&= \hat{\mathbf{e}}_r \frac{\partial}{\partial \bar{r}} + \hat{\mathbf{e}}_\theta i \frac{m}{\bar{r}} - \hat{\mathbf{e}}_\phi i \varepsilon n
\end{aligned}
\tag{2.20}
$$

The normalised perturbed magnetic field will have the following assumed ordering, $\delta \mathbf{B}/B_{0\phi} = O(\varepsilon)$, hence the order of the parallel gradient operator is:

$$
\overline{\nabla}_\parallel = \frac{\mathbf{B}}{B} \cdot \overline{\nabla} \approx \frac{\mathbf{B}_0}{B_{0\phi}} \cdot \overline{\nabla} + \frac{\delta \mathbf{B}}{B_{0\phi}} \cdot \overline{\nabla} = O(\varepsilon)
\tag{2.21}
$$

and the leading order expression for the perpendicular gradient operator may be written.

$$
\overline{\nabla}_\perp = \hat{\mathbf{e}}_r \frac{\partial}{\partial \bar{r}} + \hat{\mathbf{e}}_\theta \frac{1}{\bar{r}} \frac{\partial}{\partial \theta}
\tag{2.22}
$$

A consequence of $\nabla \cdot \delta \mathbf{B} = 0$ is that to leading order.

$$
\frac{\partial \overline{\delta B}_r}{\partial \bar{r}} + \frac{1}{\bar{r}} \frac{\partial \overline{\delta B}_\theta}{\partial \theta} = 0
\tag{2.23}
$$

i.e. the perturbed magnetic field may be expressed as a potential function.

$$
\overline{\delta \mathbf{B}} = \varepsilon \overline{\nabla} \times (\bar{\psi} \hat{\mathbf{e}}_\phi)
\tag{2.24}
$$

$\overline{\delta B_\phi} = o(\varepsilon)$ if leading order incompressibility is assumed for the temporal ordering used. A comparison of the above with the expression for the magnetic vector potential leads to the conclusion that the normalised toroidal component of the vector potential could be used to represent the function $\epsilon \bar{\psi}$ (note with the definition used above $\bar{\psi} = O(1)$ as $\varepsilon \to 0$).

Using 2.24 a linearised form of 2.21 may be written (using a perturbation with a poloidal and axial dependence of the form $e^{i(m\theta - n\phi)}$):

$$\overline{\nabla}_\parallel = i\varepsilon(\frac{m}{q(\bar{r})} - n) + i\varepsilon\frac{m}{\bar{r}}\bar{\psi}\frac{d}{d\bar{r}} = i\bar{k}_\parallel + i\varepsilon\bar{k}_\perp\bar{\psi}\frac{d}{d\bar{r}} \qquad (2.25)$$

Note $k_\parallel/k_\perp = \bar{k}_\parallel/\bar{k}_\perp = O(\varepsilon)$, which is consistent with the flute reduction. This expression also makes clear the temporal frequency order used. To explicitly show that the parallel gradient operator is $O(\varepsilon)$ the following are defined:

$$\overline{\overline{\nabla}}_\parallel = \frac{\overline{\nabla}_\parallel}{\varepsilon}$$

$$\overline{\overline{k}}_\parallel = \frac{\bar{k}_\parallel}{\varepsilon}$$

The resistive ohm's law is assumed to have the following form:

$$\mathbf{E} + \mathbf{V} \times \mathbf{B} = \eta\mathbf{J} \qquad (2.26)$$

$$\mathbf{E} = -\frac{\partial\mathbf{A}}{\partial t} - \nabla\Phi \qquad (2.27)$$

The leading order $\perp$ contribution to ohm's law, the $\mathbf{E} \times \mathbf{B}$ velocity, and 2.18 suggests:

$$\bar{\varphi} = \frac{\Phi}{\varepsilon V_A a B_\phi} = O(1) \qquad (2.28)$$

Three further quantities are defined.

$$\bar{U} = \hat{\mathbf{e}}_\phi \cdot \overline{\nabla}_\perp \times \overline{\mathbf{V}} = \overline{\nabla}_\perp^2\bar{\varphi} = O(1) \qquad (2.29)$$

$$\bar{j} = -\overline{\nabla}_\perp^2\bar{\psi} = O(1) \qquad (2.30)$$

$$\bar{\eta} = \frac{\tau_A}{\tau_R} \qquad (2.31)$$

These are the normalised vorticity, current and resistivity respectively, $\tau_R = a^2\mu_0/\eta$ is the resistive time scale.

With the above definitions the leading order expressions for the parallel ohms law and shear Alfven law may be derived.

$$\frac{\partial \bar{\psi}}{\partial \bar{t}} + \overline{\overline{\nabla}}_\parallel \bar{\varphi} = -\bar{\eta}\bar{j} \qquad (2.32)$$

$$\frac{\partial \bar{U}}{\partial \bar{t}} + \overline{\mathbf{V}}_\perp \cdot \overline{\nabla}_\perp \bar{U} = \overline{\overline{\nabla}}_\parallel(\bar{j} + \bar{j}_0) \qquad (2.33)$$

The inverse Lundquist number $\bar{\eta}$ is taken to be $O(\varepsilon)$ so as to maintain the restive term in the parallel Ohm's law.

2.1.4 The shear Alfven wave in cylindrical zero beta plasmas and neighbouring equilibria

In the following subsection the linearised ideal, $\bar{\eta} = 0$, evolution equations are considered.

$$\frac{\partial \bar{U}}{\partial \bar{t}} = i\overline{\overline{k}}_\parallel \bar{j} + i\bar{k}_\perp \bar{j}_0' \qquad (2.34)$$

$$\frac{\partial \bar{\psi}}{\partial \bar{t}} = -i\overline{\overline{k}}_\parallel \bar{\varphi} \qquad (2.35)$$

The ideal assumption is found to be a valid throughout most of the bulk plasma, typical value of $\bar{\eta}$ ranging from $10^{-7} - 10^{-10}$ in tokamak plasmas.

A perturbation of the form defined above is described as a resonant if there exists a rational surface in the plasma such that $k_\parallel(r_s) = 0$.

From this point onward the over bars are dropped for ease of notation. Performing a spectral analysis (assume a time dependence of the form $e^{-i\omega t}$), a single eigenvalue equation can be obtained for the $\omega \neq 0$ case.

$$\frac{\partial}{\partial r}((\omega^2 - k_\parallel^2)r^3 \frac{\partial}{\partial r}(\frac{\varphi}{r})) + (\omega^2 - k_\parallel^2)(1 - m^2)\varphi = 0 \qquad (2.36)$$

The inner boundary condition can be established from physical considerations. In order that the velocity remain finite $\varphi(0) = 0$. The plasma will be assumed to be bounded by a perfectly conducting wall for this instance. The radial velocity is zero $\Rightarrow \varphi(1) = 0$.

A continuum of spectrally stable solutions exist corresponding to the Alfven

modes. The Alfven modes possess singular behaviour at positions at which $\omega^2 = k_\parallel^2$. As ω decreases the singularities approach the position of $k_\parallel = 0$, which corresponds to the rational surface q_r.

The eigenvalue equation 2.36 is invalid at $\omega = 0$ unless $\varphi = 0$. However, a more general solution in which φ is independent of time can be obtained.

$$\frac{\partial}{\partial r}(k_\parallel^2 r^3 \frac{\partial}{\partial r}(\frac{\varphi}{r})) + k_\parallel^2(1 - m^2)\varphi = 0 \tag{2.37}$$

$$\psi = -ik_\parallel \varphi t \tag{2.38}$$

alternatively 2.38 may be left in terms of ψ.

$$k_\parallel \nabla_\perp^2 \psi + k_\perp j_0' \psi = 0 \tag{2.39}$$

These solutions are known as neighbouring equilibria solutions (It is noted that 2.38 has the same form as the $\omega \to 0$ case). At a rational surface, radius r_s, $k_\parallel(r_s) = 0$, suggesting a singularity in φ. The nature of the singularity is shown to be regular by expanding 2.38 about r_s, using $x = r - r_s$ and $k_\parallel(x) = k_\parallel'(0)x = 0$.

$$\frac{\partial^2 \varphi}{\partial x^2} + \frac{2}{x}\frac{\partial \varphi}{\partial x} + \frac{(1 - m^2)}{r_s^2}\varphi = 0 \tag{2.40}$$

which admits solutions

$$\varphi = |x|^\nu \sum_i a_i x^i \tag{2.41}$$

with $\nu = -1$ and $\nu = 0$ and the possibility of differing constants either side of the singularity. However, with these solutions the kinetic energy of the plasma would be infinite, i.e. no ideal MHD solution of this form actually exists.

If, with the introduction of non-ideal effects, the growth rate of the instability is sufficiently slow, then it expected that inertia effects will be small away from the singular surface. Any resistive instability with length scales of order of the macroscopic length scale will grow too slowly to be of interest. However, the effects of resistivity may become locally important in the region around the singular surface, leading to locally increased spatial gradients, thereby increasing the growth rates. In this case it is expected that to leading order the neighbour-

ing equilibria solution will hold in the bulk of the plasma away from the singular surface, and that the solution approaching the singular surface will be of the form of equation 2.41.

These neighbouring equilibria solutions lead to a jump discontinuity in $\partial \psi / \partial r$ across the rational surface corresponding to the presence of $\delta(r - r_s)$ in the perturbed current density (i.e. a current sheet must exit).

Solutions to 2.39, with $\psi(r_s, t) = \Psi(r_s, t)$ and $\psi(0, t) = \psi(a, t) = 0$, typically have a profiles similar to figure 2.2. Note the shape of the profile is determined by the equilibrium current density profile and value of the poloidal harmonic. With these boundary conditions the quantity $\hat{\psi}(r) = \psi(r, t) / \Psi(r_s, t)$ will be independent of time (linear solution). The relative jump discontinuity in the gradients at r_s is dependent of the nature of the profile. The tearing stability index, Δ', is defined as follows:

$$\Delta' = \frac{1}{\Psi(r_s, t)} \left(\frac{\partial \psi}{\partial r} \Big|_{r^+} - \frac{\partial \psi}{\partial r} \Big|_{r^-} \right). \tag{2.42}$$

The sign of Δ' will be shown to be important in the tearing mode analysis in the following section [43].
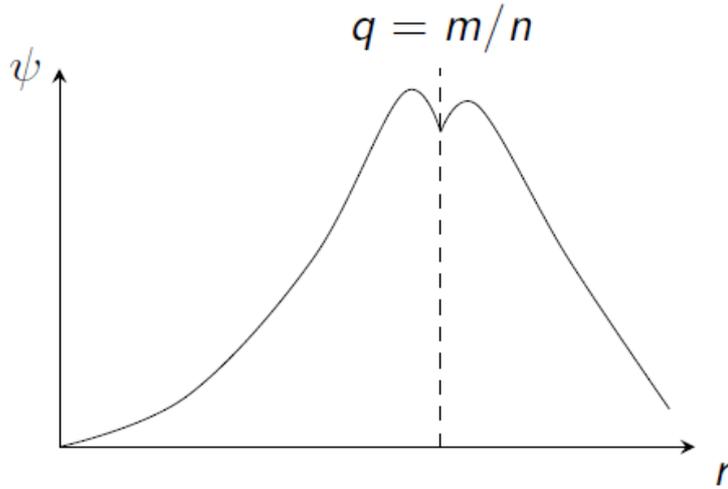
Figure 2.2: Typical neighbouring equilibria solution for the ψ profile. The jump discontinuity in $\partial \psi / \partial r$ at the rational surface indicate the presence of a current sheet [47].

Evidently the neighbouring equilibria solution is incompatible with the inclusion of resistivity around the singular surface. Even very small, but finite, resistivity would act to smooth out the discontinuity, inertia effects also becoming locally significant with the ensuing temporal changes.

2.1.5   The linear tearing mode

The introduction of small but finite resistivity raises the order of the coupled differential equations 2.34, 2.35. Boundary layers are a common feature in problems in which a small parameter multiplies the highest derivative term ([45], [48]). For most of the domain the leading order solution neglects the presence of the highest derivative term. However, in general this solution may not satisfy all of the boundary conditions, and a localised region exists whereby scale lengths are greatly increased. The highest derivative term becomes important in this localised region and the dominant balance between terms changes. Boundary layers commonly occur at the edge of domains but a zero in a coefficient of a dominant term may lead to an internal boundary layer.

A boundary layer may occur with a perturbation for which $k_\parallel(r_s) = 0$ at the rational surface. Within the boundary layer typical length scales in the radial direction, L_x, are assumed to much smaller than length scales in both the poloidal and axial direction, i.e. $k_\perp L_x \ll 1$. The linear 2 field equations, 2.35, are renormalised using a coordinate centred on the rational surface, $x^* = (\bar{r} - \bar{r}_s)/\epsilon$, $\epsilon \ll 1$. With such a normalization:

$$
\begin{aligned}
\jmath &= -\frac{1}{\epsilon^2}\frac{\partial^2 \psi}{\partial x^{*2}} \\
U &= \frac{1}{\epsilon^2}\frac{\partial^2 \varphi}{\partial x^{*2}} \\
k_\parallel(x^*) &= \epsilon k_\parallel'(0)x^* = -\epsilon k_{par}' x^*
\end{aligned}
$$

to leading order as $\epsilon \to 0$. Assuming a time dependence of the form $e^{-i\omega t}$, a natural normalisation of the layer equations is:

$$Q\frac{\partial^2 \varphi_{in}}{\partial x^{*2}} = ix^* \frac{\partial^2 \psi_{in}}{\partial x^{*2}} \qquad (2.43)$$

$$Q\psi_{in} = ix^* \varphi_{in} + \frac{\partial^2 \psi_{in}}{\partial x^{*2}} \qquad (2.44)$$

with $Q = -i\omega/(k_{par}'^{2/3}\eta^{1/3}) = (x_A/x_R)^{3/2}$ and $\epsilon = (\eta/k_{par}')^{1/3}$. x_A is the Alfven width, corresponding to the distance from the rational surface at which the growth rate is equal to the Alfven frequency, and x_R is the resistive skin depth.

These solutions can be rearranged into a single eigenvalue equation, in terms of the radial electric field, $E = \varphi_{in}'$, ([43]) which is useful for demonstrating the large x^* behaviour of the inner solution.

$$(1 + (\frac{x^*}{Q})^2)E - \frac{x^{*2}}{Q}(\frac{E'}{x^{*2}})' = \frac{1}{\Delta'} \int_{-\infty}^{\infty} \frac{E'}{x^*} dx^* \qquad (2.45)$$

Using dominant balance techniques (see [48]) the behaviour of the homogeneous (left) and inhomogeneous (right) solutions, as $x^* \to \pm\infty$, can be obtained.

$$E \sim p(x)exp(-\frac{x^{*2}}{2Q^{1/2}}) \qquad E \sim \frac{Q^2}{x^{*2}\Delta'} \int_{-\infty}^{\infty} \frac{E'}{x^*} dx^* \qquad (2.46)$$

$p(x)$ is a polynomial. The inhomogeneous term will dominate in this limit, which if integrated gives the appropriate form of φ_{in} for matching to the outer region (equation 2.41).

Equation 2.45 is invariant under the transformation $x^* \to -x^*$ which implies that the eigenmode solutions may be chosen to have even or odd parity. Those with even parity are known as tearing modes. Tearing modes allow non-zero values of $\psi_{in}(0)$ which implies that the magnetic field lines may reconnect with an associated change in topology. The odd eigenmode solutions are known as twisting modes and are not considered in this document.

Two analytic estimates [43] for the tearing mode dispersion relation may be obtained. The large solution (non-constant ψ) corresponds to the limit $\Delta'w \gg 1$ and the small solution $\Delta'w \ll 1$ (w is a the layer width).

$$Q = 1 \qquad\qquad large \qquad\qquad (2.47)$$

$$Q = (\frac{\Gamma(1/4)}{2\pi\Gamma(3/4)})^{4/5}(\epsilon\Delta')^{4/5} \qquad small \qquad (2.48)$$

Using the definitions of Q and ϵ above two relevant normalised (to the Alfven time) time-scales can be defined. $\tau_E = 1/(k_{par}'^{2/3}\eta^{1/3})$ is the typical normalised eddy decay time-scale, while $\tau_c = 1/(k_{par}'^{2/5}\eta^{3/5})$ and is the typical normalised reconnection time-scales associated with tearing modes [49]. Note that the condition for instability for the small solution is that $\Delta' > 0$. Plasmas for which $\Delta' > 0$ are known as tearing unstable [50].

2.1.6   Forced reconnection

A plasma which is tearing stable with boundary condition $\psi(a,t) = 0$ may no longer be tearing stable if this boundary condition is altered, i.e. to $\psi(a,t) = \Psi(a,t)$. Such a change in the boundary condition, with perfectly conducting walls, may occur if a slight corrugation is introduced into the wall, momentarily causing a radial plasma flow. Such a solution may be broken up into a linear combination of two separate solutions, $\psi(r,t) = \Psi(r_s,t)\hat{\psi}_m(r) + \Psi(a,t)\hat{\psi}_s(r)$, with the corresponding effective boundary conditions:

$$\hat{\psi}_m(0) = 0$$
$$\hat{\psi}_m(r_s) = 1$$
$$\hat{\psi}_m(a) = 0$$
$$\hat{\psi}_s(0) = 0$$
$$\hat{\psi}_s(r_s) = 0$$
$$\hat{\psi}_s(a) = 1$$

Substitution of this solution into equation 2.38 demonstrates that the equation and the boundary conditions are satisfied. $\hat{\psi}_m$ will be referred to as the mode solution and its solutions are the same as those previously shown in section 2.1.4

. $\hat{\psi}_s$ is the shielded solution and represents the ideal solution when the perturbed flux is completely screened). With this solution the tearing stability index may be broken into two terms.

$$
\begin{aligned}
\Delta'(t) &= \frac{1}{\Psi(r_s, t)}(\frac{\partial \psi}{\partial r}|_{r+} - \frac{\partial \psi}{\partial r}|_{r-}) \\
&= (\frac{\partial \hat{\psi}_m}{\partial r}|_{r+} - \frac{\partial \hat{\psi}_m}{\partial r}|_{r-}) + \frac{\Psi(a, t)}{\Psi(r_s, t)}(\frac{\partial \hat{\psi}_s}{\partial r}|_{r+} - \frac{\partial \hat{\psi}_s}{\partial r}|_{r-}) \\
&= \Delta'_m + \frac{\Psi(a, t)}{\Psi(r_s, t)}\Delta'_s
\end{aligned}
\tag{2.49}
$$

Note both Δ'_m and Δ'_s are independent of time (for the linear problem), however Δ' is now time dependent. Cases will be examined for which $\Delta'_m < 0$ (i.e. the plasma without the corrugation is tearing stable). For simplicity the boundary condition will be taken to be time independent in the following, $\Psi(a)$, the rise time assumed to be much faster than the reconnection dynamics (i.e. appearing as effective step function).

The outer solution may be Laplace transformed in time $L(f)(x, s) = \tilde{f}(x, s) = \int_0^\infty f(x, t)e^{-st}dt$ yielding:

$$
\frac{\tilde{\Psi}(r_s, s)}{\Psi(a)} = \frac{\Delta'_c}{(\tilde{\Delta}'(s) - \Delta'_m)}\frac{1}{s}
\tag{2.50}
$$

In general the inverse Laplace has the form:

$$
\frac{\Psi(r_s, t)}{\Psi(a)} = \frac{1}{2\pi i}\oint_C \frac{\Delta'_c e^{st}}{(\tilde{\Delta}'(s) - \Delta'_m)}\frac{1}{s}ds
\tag{2.51}
$$

the integral may be solved by finding the residues (see [51]), with poles occurring when $s = 0$ and $\tilde{\Delta}'(s) = \Delta'_m$, with the possibility of branch points if $\tilde{\Delta}'(s) - \Delta'_m$ is multivalued. The behaviour as $t \to \infty$ will be dominated by the pole or branch point with the largest real part (see [48]). In a naturally tearing stable plasma no poles should appear for $\Re(s) > 0$. Assuming that the pole at $s = 0$ is the only pole lying on the imaginary axis the final reconnected flux should have a value $\Psi(r_s, \infty) = \Psi(a)\Delta'_s/(-\Delta'_m)$. This makes intuitive sense as it as at this value the jump discontinuity in the gradient is removed and $\Delta' = 0$.

The quantity $\tilde{\Delta}(s)$ is found by matching to the inner layer. The Laplaced transformed inner layer equations have the same form as 2.43 and 2.44 with $Q = s\tau_E$, $\psi_{in}(x^*, t) \to \tilde{\psi}_{in}(x^*, Q)$, and $\varphi_{in}(x^*, t) \to \tilde{\varphi}_{in}(x^*, Q)$.

If $\psi(x^*, \tau)$, with a renormalised temporal variable $\tau = t/\tau_E$, possesses an expansion in the neighbourhood of $\tau = 0$, of the form $\psi(x_*, \tau) = \tau^\lambda \sum_p \tau^p \psi^{(p)}(x^*, 0)$, ($\lambda < 1$), then Watson's Lemma (see [48]) implies that the asymptotic form of the Laplace transform, as $|Q| \to \infty$, $|arg(Q)| < \pi/2$, is:

$$\tilde{\psi}(x^*, Q) \sim \sum_p \frac{\psi^{(p)}(x^*, 0)\Gamma(\lambda + p + 1)}{p! Q^{\lambda + p + 1}} \tag{2.52}$$

This intern implies that if the expression 2.50 can be expanded in the above form as $|Q| \to \infty$, $|arg(Q)| < \pi/2$, then this expansion may be inverse Laplace transformed to yield $\psi(x^*, \tau)$ for $\tau \ll 1$. The same argument holds for φ.

The form of $\tilde{\varphi}$ as $x^* \to \pm\infty$ is assumed from the outer region as $x \to 0$. Multiplying $\tilde{\varphi}$ by a step function, $H(x^*)$ and Laplace transforming $x^* \to g$, $\tilde{\varphi}(x^*, s) \to \breve{\varphi}(g, s)$, the final value theorem, $g \to 0^+ \Rightarrow g\breve{\varphi} = \tilde{\varphi}_R$, demonstrates the existence of a pole at $g = 0$ corresponding to the behaviour of $x^* \to \infty$. Similar analysis can be performed on the left hand limit.
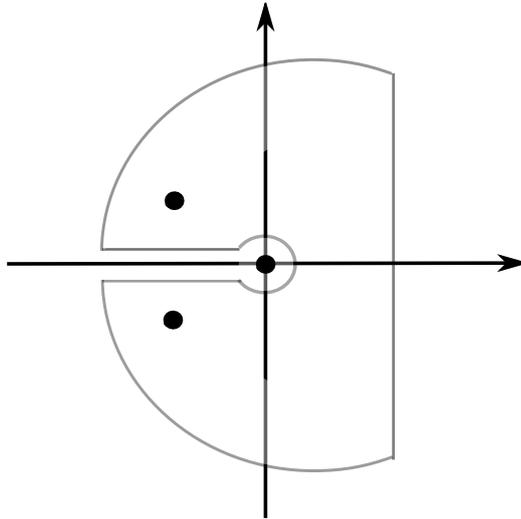
Figure 2.3: Poles in the complex plane of the constant ψ regime

[52] and [53] both consider the problem in the symmetric slab configuration. Analytic limits in either case are obtained for $Q \gg 1$ ($\tau \ll 1$) and $Q \ll 1$, the later case approaching the root at $s = 0$ in equation 2.51 corresponding to the final condition. [52] rearranges 2.43 and 2.44 to form a single evolution equation in terms of the perturbed current. [53] Fourier transforms, $\breve{f}(g, Q) = \int_{-\infty}^{\infty} \tilde{f} e^{-igx^*} dx^*$, 2.43 and 2.44 in x^* ultimately producing a single equation in $\breve{\varphi}$.

$$\frac{\partial^2 \breve{\varphi}}{\partial g^2} + \frac{2Q}{g(Q + g^2)} \frac{\partial \breve{\varphi}}{\partial \breve{g}} - Q(Q + g^2)\breve{\varphi} = 0 \tag{2.53}$$

Resolving the solution about the singularity at $g = 0$ will determine the matching condition to the outer region. The leading order behaviour in an expansion about $g = 0$ is determined by a balance between the first two terms in 2.53. However information regarding the constants in the expansion are dependent on the profile in the rest of the layer. For full detail refer to [53], although the results may be summarised. By expansion of g in terms of in intermediate variable it is possible to determine the range of dominance of particular terms. For the $Q \gg 1$ case, to leading order, terms involving resistivity are neglected. This is to be expected by consideration of the definition for Q, resistivity only becoming important in a small secondary layer close to the rational surface. This regime is known as the inertial regime, the plasma behaving as if it were essentially ideal. Matching to the outer region:

$$\Delta'(Q) = -\frac{\pi}{\epsilon Q} \qquad \delta_I \sim 1 \tag{2.54}$$

δ_I is the approximate layer width. Note $\Delta'(Q)\delta_I \sim 1$ inferring ψ will vary across the layer and so this regime is known as a non-constant ψ regime. An indication of the amount of reconnection which has taken place can be inferred from $\psi_{in}(0, t)$, and the reconnection rate $\partial \psi_{in}/\partial t(0, t) = \eta \jmath(0, t)$. [54] demonstrates how to relate ψ at the centre and edge of the layer, with the result:

$$\psi_{in}(0, t) \quad \propto \quad \eta t^2 \tag{2.55}$$
$$\jmath(0, t) \quad \propto \quad t \tag{2.56}$$

In the Resistive Inertial (RI) regime, $Q \ll 1$, resistivity becomes important. The layer equation is solved in a two step process by matching over two overlapping analytic limits. The results are:

$$\Delta'(Q) = (2\pi \frac{\Gamma(3/4)}{\Gamma(1/4)})^{5/4} \frac{Q^{5/4}}{\epsilon} \qquad \delta_{RI} \sim Q^{1/4} \qquad (2.57)$$

or renormalising to the tearing mode time scale, $h = s\tau_c$.

$$\Delta'(h) = (2\pi \frac{\Gamma(3/4)}{\Gamma(1/4)})^{5/4} h^{5/4} \qquad (2.58)$$

By a similar analysis the RI regime is found to be a constant ψ regime, i.e. $\Psi(r_s, t)$ will be a good approximation of $\psi_{in}(0, t)$

Substitution of the expression for Δ' into equation 2.51 and renormalising the temporal variable $\tau_1 = t/\tau_c$ the form for the inverse Laplace transform can be obtained:

$$\frac{\Psi(\tau_1)}{\Psi(a)} = 1 - \frac{4}{5}(e^{h_+\tau_1} + e^{h_-\tau_1}) + \frac{\lambda}{\sqrt{2\pi}} \int_0^\infty \frac{u^{1/4}e^{-u\tau_1}du}{(1 - \sqrt{2}\lambda u^{5/4} + \lambda^2 u^{5/2})} \qquad (2.59)$$

with $\lambda = (2\pi/(-\Delta'_m))(\Gamma(3/4)/\Gamma(1/4))$ poles at $h_\pm = \lambda^{-4/5}e^{\pm i4\pi/5}$. The two poles $h_\pm$ have decaying components (figure 2.3). A pole also exist at $h = 0$ as well as a branch line along the negative real axis (The integral contribution in equation 2.59) Asymptotic limits can be found in the limit $\tau_1 \gg 1$ by expansion of the integral in this limit. The asymptotic expansion for the limit $\tau_1 \ll 1$ can be obtained by considering the renormalise form of 2.50.

$$\frac{\Psi(t)}{\Psi(a)} = \frac{8\sqrt{2}}{5\pi}\Gamma(\frac{3}{4})(\frac{t}{\tau_0})^{5/4} \qquad \tau_0 \ll 1 \qquad (2.60)$$

$$\frac{\Psi(t)}{\Psi(a)} = 1 - \frac{\Gamma(5/4)}{\sqrt{2\pi}}(\frac{\tau_0}{t})^{5/4} \qquad \tau_0 \gg 1 \qquad (2.61)$$

with $\tau_0 = \lambda^{4/5}\tau_c$

The reconnection rate in the constant ψ regime is then given by:

$$\frac{\partial \Psi}{\partial \tau_1} = -\frac{5}{4}(h_+ e^{h_+ \tau_1} + h_- e^{h_- \tau_1}) - \frac{\lambda}{\sqrt{2\pi}} \int_0^\infty \frac{u^{5/4} e^{-u\tau_1} du}{(1 - \sqrt{2}\lambda u^{5/4} + \lambda^2 u^{5/2})} \quad (2.62)$$

The inverse Lundquist number $\bar{\eta}$ is taken to be $O(\varepsilon)$ so as to maintain the restive term in the parallel Ohm's law.

2.1.7 Suppression of reconnection with plasma rotation

The effect of the introduction of an equilibrium velocity, $\mathbf{V}_0(r)$, profile will now be examined. It is assumed that the flow is of the same order as described in section 2.1.3, and the velocity is approximately constant across the layer.

The Laplace transformed layer equations have the form

$$(Q + iQ_\Omega)\frac{\partial^2 \tilde{\varphi}_{in}}{\partial x^{*2}} = ix^* \frac{\partial^2 \psi_{in}}{\partial x^{*2}} \quad (2.63)$$

$$(Q + iQ_\Omega)\tilde{\psi}_{in} = ix^* \tilde{\varphi}_{in} + \frac{\partial^2 \tilde{\psi}_{in}}{\partial x^{*2}} \quad (2.64)$$

with $Q = \Omega\tau_E = (v_{\theta 0}(r_s)m/r_s - v_{\phi 0}(r_s)n/R_0)\tau_E$. Making note of:

$$\tilde{f}(x,t) = \int_0^\infty f(x,t)e^{-st}dt = \int_0^\infty f(x,s)e^{i\Omega t}e^{-s_1 t}dt = L\{fe^{i\Omega t}\}(x,s_1) \quad (2.65)$$

the layer equations have the same form as 2.43 and 2.44.

$$Q_1 \frac{\partial^2 L\{\varphi_{in}e^{iQ_\Omega \tau}\}}{\partial x^2} = (...) \quad (2.66)$$

$$Q_1 L\{\psi_{in}e^{iQ_\Omega \tau}\} = (...) \quad (2.67)$$

The outer equations region equations have the form:

$$\frac{L\{\Psi(r_s,t)e^{i\Omega t}\}}{\Psi(a)} = \frac{\Delta_c'}{(\tilde{\Delta}'(s_1) - \Delta_m')} \frac{1}{(s_1 - i\Omega)} \tag{2.68}$$

$$\tilde{\Delta}'(s_1) = \frac{dL\{\psi e^{i\Omega t}\}}{dr}\Big|_{r^+} - \frac{dL\{\psi e^{i\Omega t}\}}{dr}\Big|_{r^-} \tag{2.69}$$

Upon inverse transforming:

$$\frac{\Psi(r_s,t)}{\Psi(a)} = \frac{e^{-i\Omega t}}{2\pi i} \oint_C \frac{\Delta_c' e^{s_1 t}}{(\tilde{\Delta}'(s_1) - \Delta_m')} \frac{1}{(s_1 - i\Omega)} ds_1 \tag{2.70}$$

It is observed that the pole previously at the origin now moves up to the imaginary axis, i.e. the solution will tend to the steady state solution with $s_1 = i\Omega$ (figure 2.4). By obtaining the residue at this pole, and defining $\Psi_{full} = \Delta_s'/(-\Delta_m')$, the final perturbed flux at the edge of the layer is:

$$\frac{\Psi(r_s,\infty)}{\Psi_{full}} = \frac{1}{(\tilde{\Delta}'(i\Omega)/(-\Delta_m')) + 1} \tag{2.71}$$

It is observed that for $|(\tilde{\Delta}'(i\Omega)/(-\Delta_m'))| \gg 1$ reconnection will be greatly suppressed. It is also worth noting that the above is equivalent to having no equilibrium flow and a rotating corrugation as described in [49].

For the case of $|Q_1| \gg |Q_\Omega|$, it is expected that the initial reconnection rate should remain unchanged from the $\Omega = 0$ case. The decay rate of the solution to its steady state form as $t \to \infty$ will still be dominated by the branch point, but now being oscillatory. Steady state solutions to these equations may be searched for in the limits $Q_\Omega \gg 1$ and $Q_\Omega \ll 1$, the analysis remaining virtually unchanged.

2.1.8   Inclusion of viscosity

The ordering used in [43] neglects viscosity to leading order. The length scales in the boundary layer are shorter than those assumed in section 2.1.3 and ultimately additional terms may become important in this region. A simple version of viscosity is included in the vorticity equation (2.33).

$$\frac{\partial U}{\partial t} + \mathbf{V} \cdot \nabla_\perp U = \nabla_\parallel (\jmath + \jmath_0) + \mu \nabla_\perp^2 U \tag{2.72}$$
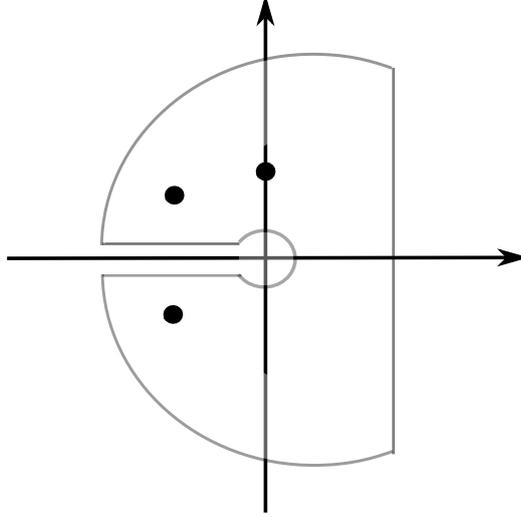
Figure 2.4: The movement of the pole up the imaginary axis with the introduction of equilibrium flow. This demonstrates a different final state of the plasma to a plasma with zero equilibrium flow

with the associated linear layer equation:

$$Q_1 \frac{\partial^2 \varphi_{in}}{\partial x^{*2}} = ix^* \frac{\partial^2 \psi_{in}}{\partial x^{*2}} + P \frac{\partial^4 \varphi_{in}}{\partial x^{*4}} \tag{2.73}$$

The Prandtl number $P = \mu/\eta$. The inclusion of viscosity is seen to raise the order of the differential equation and the relative ordering of P will determine the impact of the viscosity term on the layer. Searching for steady state solutions, the Fourier-Laplaced transformed layer equation takes the form:

$$\frac{\partial^2 \breve{\varphi}}{\partial g^2} + \frac{2Q}{g(Q + g^2)} \frac{\partial \breve{\varphi}}{\partial \breve{g}} - Q(Q + g^2)\breve{\varphi} = 0 \tag{2.74}$$

$$\frac{d^2 \breve{\varphi}}{dg^2} + \frac{2Q_\Omega}{g(Q_\Omega + ig^2)} \frac{d\breve{\varphi}}{dg} + (Q_\Omega^2 - iQ_\Omega g^2(1 + P) - Pg^4)\breve{\varphi} = 0 \tag{2.75}$$

Again analytic approximations for $\Delta'(iQ_\Omega)$ may be derived in the limits $Q \to 0$ and $Q \to \infty$. An order for P is assumed in each of the Q limits. The assumed order determines the dominate contribution of terms in different regions of the

layer. The boundaries determining which terms are dominant in obtaining the constants are displayed in figure 2.5. Of the four regions the Visco-Resistive (VR) and Resistive Inertial (Ri) are constant ψ regimes whereas the Visco-Inertial (VI) and Inertial are non-constant ψ regimes. Ultimately depending on the regime, the structure of the layer changes, with the possibility of multiple layers if neglected terms correspond to higher derivatives in the untransformed layer equations.
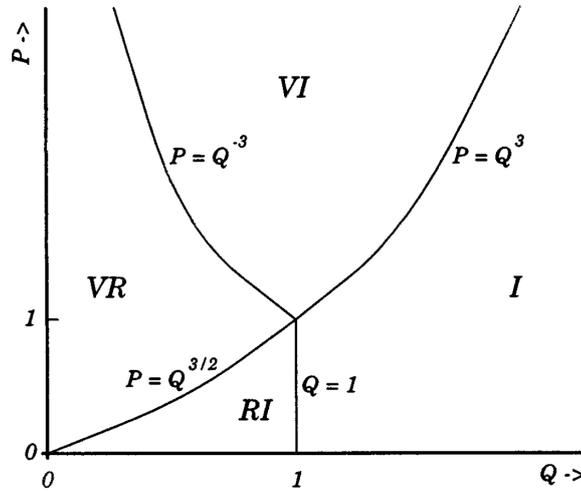
Figure 2.5: The 4 different linear layer asymptotic regimes. (I) Inertial, (RI) Resistive Inertial, (VI) Visco-Inertial, (VR) Visco-Resistive [19]

2.1.9 Torque balance and bifurcation

The flux surface averaged electromagnetic torque acting in the poloidal direction may be written:

$$T_{\theta EM}(r) = \oint \oint r\hat{\mathbf{e}}_\theta \cdot (\mathbf{J}_{eq} + \delta\mathbf{J}_{eq}) \times (\mathbf{J}_{eq} + \delta\mathbf{J}_{eq}) r d\theta R_0 d\phi \qquad (2.76)$$

Or in terms of the normalised variables (neglecting over-bars):

$$T_{\theta EM}(r) = -2(2\pi)^2 \varepsilon m \Im(r\psi^* \nabla^2 \psi) \qquad (2.77)$$

The * in this instance representing the complex conjugate. The flux surface average torque acting in the toroidal direction related to the poloidal torque in a simple manner.

$$T_{\phi EM}(r) = -\frac{n}{m}T_{\theta EM}(r) \tag{2.78}$$

By consideration of equation 2.39 it is straight forward to demonstrate, in the outer region, $T_{\theta EM}(r) = 0$. Physically the bulk plasma is able to displace in such a manner as to avoid inducing eddy currents. However, if the radial integral extends across the layer (assuming a steady state), by consideration of equations 2.49 and 2.71, and assuming a suppressed state $|(\tilde{\Delta}'(i\Omega)/(-\Delta'_m))| \gg 1$:

$$
\begin{aligned}
T_{\theta EM} &= -2(2\pi)^2 \varepsilon m \Im(\frac{1}{\Delta'(i\Omega)}) r_s \Delta'^2_m |\Psi_{full}|^2 \\
&= -2(2\pi)^2 \varepsilon m \Im(\frac{1}{\Delta'(i\Omega)}) r_s \Delta'^2_s |\Psi(a)|^2
\end{aligned}
\tag{2.79}
$$

a radially localised net electromagnetic torque may exist in the vicinity of the rational surface. $|\Psi(a)|$ can be related to the vacuum error field amplitude at the layer [19].

Evidently the electromagnetic toque is produced through a non-linear interaction. However the linear layer equations are still valid to leading order provided that the magnetic islands do not exceed the linear layer width. With the inclusion of non-linear terms the equilibrium (flux surface averaged) profiles may evolve over much larger time scales than those considered in section 2.1.3, the problem becoming one of multiple temporal as-well as spatial scales.

Electromagnetic torque profiles may be obtained for the asymptotic linear layer regimes discussed in the previous section. Torque profiles are displayed in figures for the low (left) and high (right) P cases.

Note that the electromagnetic torque always acts to decrease the plasma velocity in these regimes.

Steady state equilibria may exist if an opposing force acts to balance the electromagnetic force. In toroidal geometry neoclassical forces strongly damp devations in the poloidal velocity away from the unperturbed equilibrium value
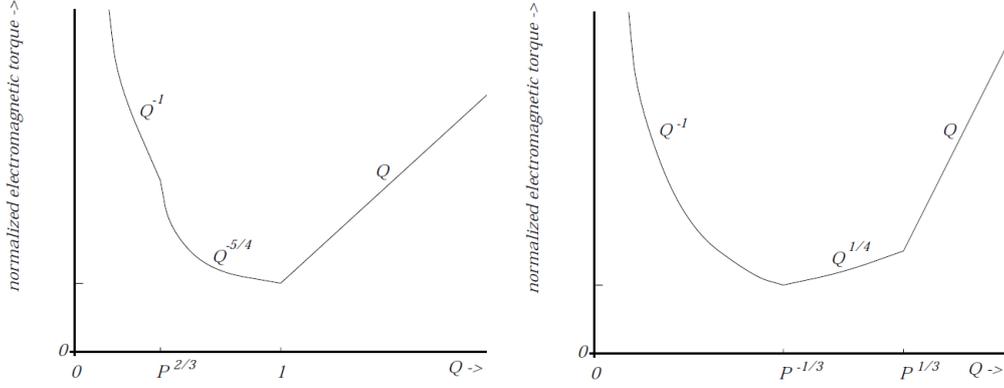
Figure 2.6: Normalised torque curves in the quasi-linear regimes for (a) low viscosity, (b) high viscosity limits. [19]

[55]. Effectively the plasma only undergoes rotation braking in the toroidal direction. The toroidal electromagnetic force is generally balanced by the viscous force (figure 2.7 (left)). However if the perturbation strength is raised above a critical threshold or the equilibrium velocity reduced the system may undergo a bifurcation (figure 2.7 (right)).

2.1.10 Inclusion of diamagnetic effects

A number of interesting features are observed with the inclusion of two fluid effects. The model adopted to the observe two fluid effects is that given in [40], which in turn is a reduction of the model presented in [46].

$$\frac{DU}{Dt} = \nabla_{||}J + \mu\nabla_{\perp}^2 U \tag{2.80}$$

$$\frac{\partial\psi}{\partial t} = -\nabla_{||}\varphi - \eta J + \varrho\nabla_{||}p \tag{2.81}$$

$$\frac{Dp}{Dt} = \varrho\nabla_{||}J \tag{2.82}$$

The system assumes a slab geometry, with cold ions, $T_i = 0$ and a constant electron temperature, T_e. $\varrho = c_s/(\Omega_i a)$ is a measure of the ion Lamor radius mea-
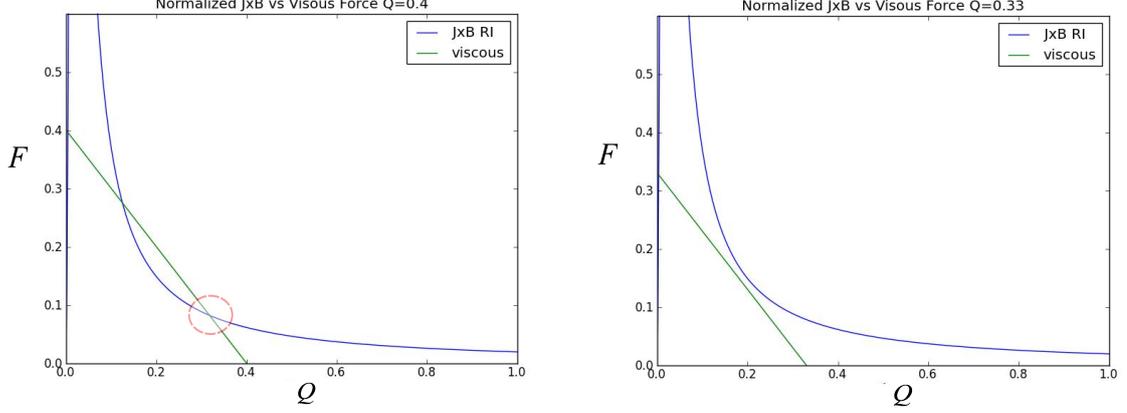
Figure 2.7: Normalised force (F) against normalised rotation frequency (Q) (a) The balance of $\mathbf{J} \times \mathbf{B}$ (blue) and viscous forces (green) (the red circle displays the new equilibrium position). (b) A bifurcation scenario in which the viscous force cannot balance the $\mathbf{J} \times \mathbf{B}$ force.

sured at the electron temperature. $c_s = T_e/m_i$ is the ion sound speed measured at the electron temperature.

The equilibrium electron pressure profile introduces an equilibrium electron diamagnetic velocity profile. The linearised layer equations may be rearranged to obtain the following form:

$$Q_\Omega^2 \frac{\partial^2 \tilde{\varphi}_{in}}{\partial x^{*2}} = x^* \frac{\partial^2 \tilde{\psi}_{in}}{\partial x^{*2}} + iPQ_\Omega \frac{\partial^4 \tilde{\varphi}_{in}}{\partial x^{*4}} \tag{2.83}$$

$$\frac{\partial^2 \tilde{\psi}}{\partial x^{*2}} = iK(x^*)(Q_\Omega - Q_D)(\tilde{\psi}_{in} - x^* \tilde{\varphi}_{in}) \tag{2.84}$$

$$K(x^*) = \frac{1}{1 - iR^2 x^{*2}/Q_\Omega} \tag{2.85}$$

with $R = \varrho/\epsilon$

Two interesting features occur in Ohm's law. The first is the presence of the electron diamagnetic rotation frequency, Q_D. In the 2-field case presented previously a resonance in the final reconnected state was observed to occur at $Q_\Omega = 0$. For the current case two resonances occur. One at $Q_\Omega = 0$ and the other at $Q_\Omega = Q_D$. The later resonance is referred to as the electron resonance.

If ion diamagnetic terms were introduced three resonances would occur. In the 2-field case these resonances all overlap. The effect of the electron resonance on the torque profile can be observed in figure 2.8. The plasma may now brake towards either the resonance depending on it's initial state. However, it was shown numerically in [56] and semi-analytically in [41] that particle diffusivity knocks out all but the electron resonance.

The second interesting feature is the spatial and frequency dependence of the conductivity $K(x^*, Q_\Omega)$, giving rise to the possibility of a conductivity channel. However, this document will not be concerned with the later feature. Chapter 3 makes use of the former.

A very similar analysis may be performed on the 3-field model as was done for the 2-field model, revealing a number of different possible regimes (figure 2.9).
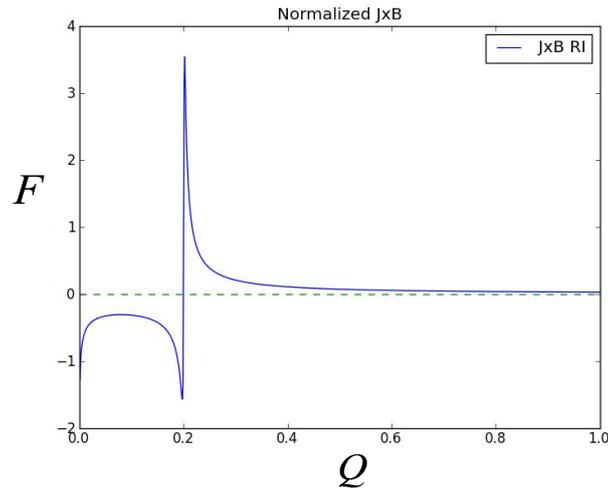
Figure 2.8: Normalised $\mathbf{J} \times \mathbf{B}$ (F) force against normalised rotation frequency (Q) displaying resonances at zeros in the electron and ion rotation frequencies
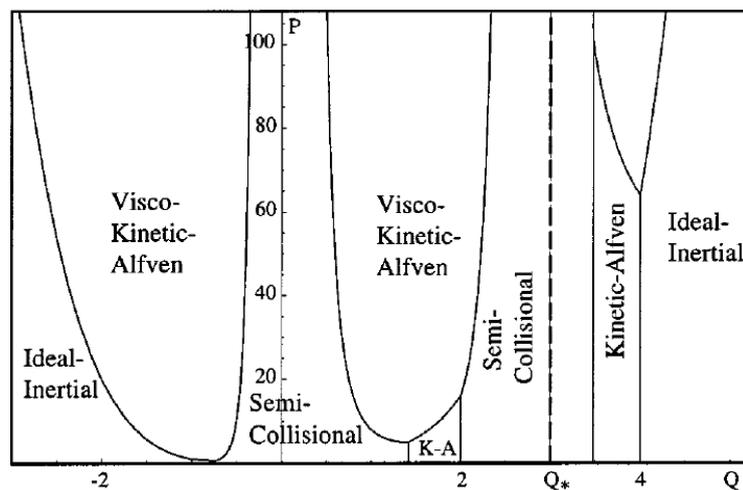
Figure 2.9: Linear regimes boundaries in the diamagnetic slab model [40]

Chapter 3

Numerical Modelling

A range of numerical modelling has been carried out to simulate the effects of RMPs on a plasma. A number of methods exist for categorising the modelling performed. Geometry is one such categorising method and is used here to split the results into slab, cylindrical, toroidal results.

The response of a plasma to harmonics which are resonant with a particular surface, is sufficiently radially localised that many of the features of the response may be examined in slab geometry. The slab geometry has the particular advantage that numerical results can often be tested against analytic asymptotic approximations or semi-analytic models. Reconnection dynamics at rational surfaces underpin how a plasma responds to a resonant harmonic and analytic models have been proposed (see section 2.1.6) and tested by specially designed codes for inviscid [53] [57] and viscous [54] reduced MHD equations.

Two fluid slab modelling has been performed in [56] to test the semi-analytic quasi-linear predictions of [40], and with the diamagnetic terms turned off the predictions of [19]. The modelling showed the expected plasma braking towards the zero in the electron rotation profile. However, disagreement existed between modelling and theory about plasma braking towards the ion and guiding centre resonances (see section 2.1.10). The semi-analytic results used of [41] subsequently showed that the ion and guiding centre resonances disappear with the introduction of particle diffusivity, which was retained in [56], but not in [40].

Both kinetic [58] and two-fluid simulations [39] have been performed for modelling the effects of RMPs in cylindrical geometry. As opposed to the slab model,

multiple resonant surfaces are introduced. DIII-D like profiles and parameters have been tested in the models. Both fluid and kinetic models displayed strong suppression of magnetic islands in the pedestal region. A region at which the RMPs could penetrate more easily existed around a region at which the perpendicular electron rotation was zero. A disadvantage of these cylindrical models is that the edge current profiles must be modified to account for the divergence near the separatrix.

The toroidal case has been modelled using the single fluid resistive MHD equations in [59]. Non-linear effects were not included in the model so plasma braking could not be examined. Instead the magnitude of the plasma response was measured with the variation of a number of different parameters.

Numerical modelling in this chapter is performed in slab geometry and a number of tests are analysed against the results of linear layer physics. A number of aspects are considered in this chapter that have been overlooked in previous analysis. The specifically designed 1-D and 2-D reconnection dynamics codes used in [53], [57], and [54] use a very large number of grid points in the radial direction, and as such the linear layer is well resolved. In more general 3-D codes, with multiple rational surfaces, only a limited no of grid points may be designated to the region surrounding each rational surface for numerical economy considerations. The question then remains as to how many grid points are required to properly resolve the layer. This is of importance in RMP simulations, as the $\mathbf{J} \times \mathbf{B}$ braking force will not be accurately reproduced if the layer is not resolved properly. This will affect both magnetic field penetration dynamics and the bifurcation thresholds.

The code used for performing the numerical calculations is the BOUT++ code. Modifications had to be applied to the code in order to correctly incorporate a more general class of boundary conditions. This is essential for the using the code to model RMP and error field type problems.

The chapter is split into a number of sections. The initial section is devoted to a brief introduction of the BOUT++ code as well as a summary of boundary conditions used in the code. The inviscid Taylor problem is then used to rigorously test the BOUT++ codes ability to handle reconnection problems. These are the first rigorous test of the BOUT++ code for reconnection problems. The

inviscid Taylor problem is further used to test the amount of radial grid packing required to produce accurate reconnection results, and which regime determines the amount of radial grid packing required. This is a point which has been overlooked by other authors. Sections 3.3 and 3.4 both introduce equilibrium flow. The final suppressed states are compared against analytic approximations. Furthermore section 3.4 highlights the importance of allowing sufficient radial domain space in the outer region to avoid the presence of current sheets at the radial boundaries. The presence of current sheet modifies the boundary conditions away from those which are intended leading to incorrect bifurcation threshold and final state equilibrium comparisons. Finally the discussion section points out the relevance of testing linear layer analysis, firstly as a first step to check numerical codes, before turning on additional non-linear terms. Secondly as important step for comparing experimental and numerical displacement measurement data [59], which can be used to help validate terms used in numerical models. And finally, as Tokamaks increase in size, it is predicted that island dynamics will move from the non-linear Rutherford regime into the quasi-linear regimes [19] (i.e. it is expected that the response at rational surfaces to error fields in ITER will be in the quasi-linear regimes). Validating the linear response of the plasma is an important step in validating the $\mathbf{J} \times \mathbf{B}$ braking force in these quasi-linear regimes.

3.1 The BOUT++ code

The BOUT++ code is object oriented C++ code, which can evolve an arbitrary set of equations in a curvilinear coordinate system. The BOUT++ framework provides a user friendly environment allowing the vast majority of parallel communication, and differential geometry to be separated from the basic user environment. Operator overloading allows for simple handing of data sets and the use of mathematical operators is intuitive and clear.

The equilibrium quantities are introduced via the use of a predefined input file, and the chosen metric tensor specified in the user environment. The coordinate system used in all the simulations in this chapter use a equilibrium magnetic field aligned coordinates. A description of the field aligned coordinate system implemented in BOUT++ code is given in [60] and [61]. The instabilities of

interest are expected to be elongated along the field line, the coordinate system used exploiting this for numerical economy.

Although the code has been benchmarked against a number of test cases [60], it has not been benchmarked for reconnection type problems. For a mixture of simplicity and for the ability to test against analytical results, the benchmarking in this chapter is performed using a sheared slab geometry. The slab is both periodic in the poloidal, θ, and toroidal, ϕ, directions to mimic a radially localised region in tokamak or toroidally periodic cylindrical geometry (figure 3.1). The cut is taken such that a rational surface is at the centre of the radial domain, unless otherwise stated the rational surface will be the q = 3 surface.
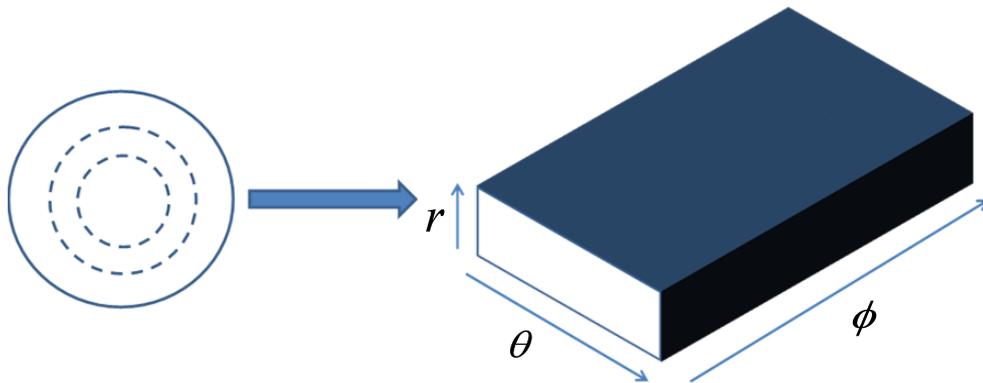
Figure 3.1: slab approximation from cylindrical geometry

3.1.1 Boundary Conditions

The BOUT++ code has a number of predefined commonly occurring boundary conditions (Dirchlet, Neumann, etc) which may be selected as options in an input file. However, these boundary conditions must be chosen self constantly to avoid steep gradient regions and numerical difficulties at the edge of the domain boundaries. The nature of the forced reconnection problem required that non-standard BOUT++ boundary conditions be defined. A number of features in which the BOUT++ code dealt with boundary conditions through the inverse Laplacian operator had to modified to accommodate the particular set of boundary conditions used.

In its standard format the BOUT++ uses 2 boundary cells in its non-periodic (flux coordinate) direction, which enclose the remaining grid cells (figure 3.2). A resonant perturbation is applied to both radial boundaries, equivalent to a corrugation in perfectly conducting wall, by applying the condition $\psi = \tilde{\psi} cos(m\theta - n\phi)$ to the inner boundary cells. The ψ perturbation applied to both radial boundaries is the same to maintain leading order symmetry in the problem. The current density boundary condition applied to both grid cells is a linearised version of:

$$\mathbf{B} \cdot \nabla(\jmath + \jmath_0) = 0 \tag{3.1}$$

which is the analytic form for the leading outer region presented in section 2.1.4. The outer boundary cell for the ψ condition is then set the be consistent with 3.1, using a 2nd order central differencing scheme.

The inner cell for the φ boundary condition is set via the analytic outer region condition (linearised version of):

$$\mathbf{B} \cdot \nabla(\varphi + \varphi_0) = 0 \tag{3.2}$$

which is self consistent with the ψ boundary condition with $\partial \psi / \partial t = 0$ (i.e. applied through a step function). The outer φ boundary cell is set to be consistent with the vorticity boundary condition $U = 0$. These boundary conditions are self consistent for the slab model, and the method of application across the two boundary cells was found to give the smoothest transition to the remainder of the numerical domain.
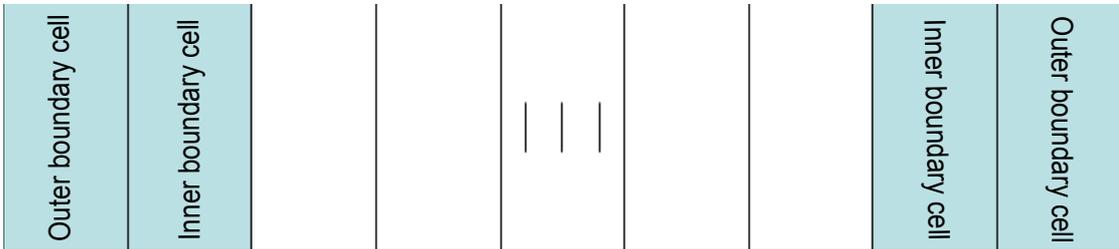
Figure 3.2: A row of grid cells in the x direction displaying the relative location of the inner and outer boundary cells

The validity of the boundary conditions is reliant on the form for the outer region being a good approximation. It was found that maintaining the ratio of the layer width to radial domain size of ~ 0.1 gave a smooth transition to the boundary region. With an increased ratio, current and vorticity sheets tended to start to form between the boundary and internal grid cells, especially when equilibrium plasma rotation was increased.

3.2 The inviscid Taylor problem

Under the appropriate transformation the equilibrium configuration used is the same as that described in [53], [57] (to leading order). Initial simulations were performed for a slab with a constant equilibrium j_0 profile. The equilibrium poloidal magnetic field and q profile used are displayed in figures 3.3 and 3.4 respectively. The toroidal magnetic field is constant, $B_\phi = 6.14\,T$, while the poloidal magnetic field has the functional form $B_\theta(x) = B_\theta(0) - Ax$. The radial domain is $-a_{slab} \leq x \leq a_{slab}$, with $a_{slab} = 0.05m$. The layer width is typically chosen ~ 0.1 of the domain width. Additional parameters associated with the equilibrium are as follows:

$$
\begin{aligned}
R_0 &= 10.0m \\
a &= 1.0m \\
\varepsilon &= \frac{a}{R_0} = 0.1 \\
s &= \frac{a}{q(r_s)}\frac{dq}{dr}\Big|_{r_s} = 1.33
\end{aligned}
$$

The boundary of the plasma at either side of the radial domain is assumed to be a perfectly conducting wall. The resonant perturbation is applied to the plasma by a small displacement to the wall.

Normalised leading order analytic estimates of the outer region solution may be obtained by inserting $j_0' = 0$ and additional equilibrium parameters into equation 2.39 (section 2.1.4). Figure 3.5 displays both the mode solution, $\hat{\psi}_m$ (black), and the shielded, $\hat{\psi}_s$ (blue). The red line is the vacuum solution. A guide for the
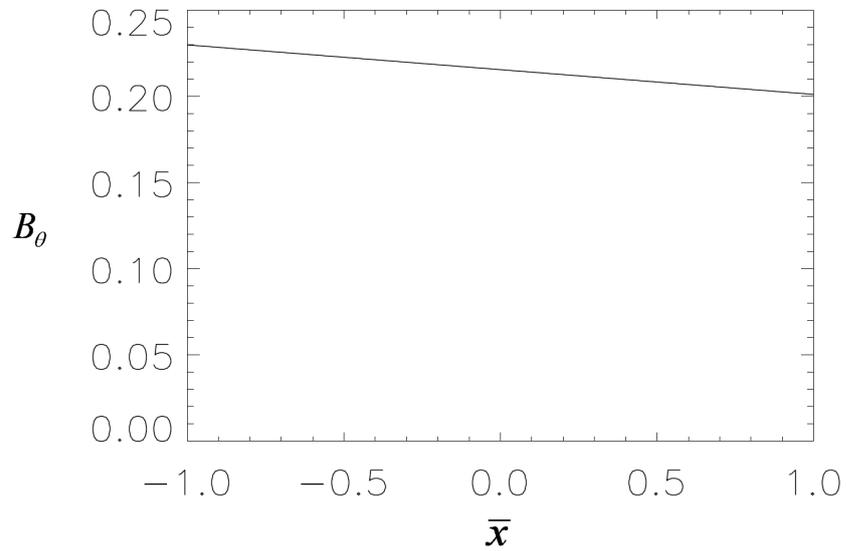
Figure 3.3: The linear B_θ profile used in the inviscid Taylor problem.
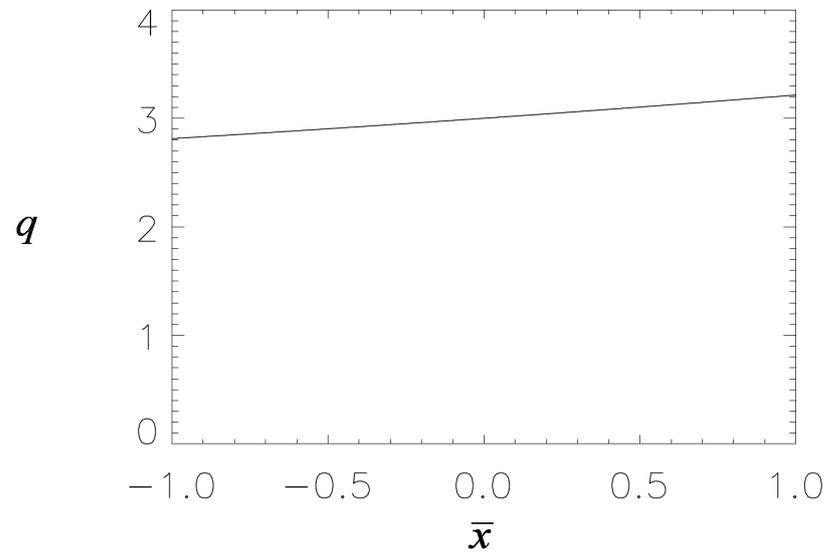
Figure 3.4: The q profile corresponding to the linear B_θ profile

expected temporal evolution of the outer region is shown in figure 3.6. Δ'_m and Δ'_s are easily calculated for such a profile, the analytic forms and values given by:

$$\Delta'_m \;\; = \;\; -\frac{2k_\perp}{tanh(k_\perp a)} = -2.015 \tag{3.3}$$

$$\Delta'_s \;\; = \;\; \frac{2k_\perp}{sinh(k_\perp a)} = 1.993 \tag{3.4}$$
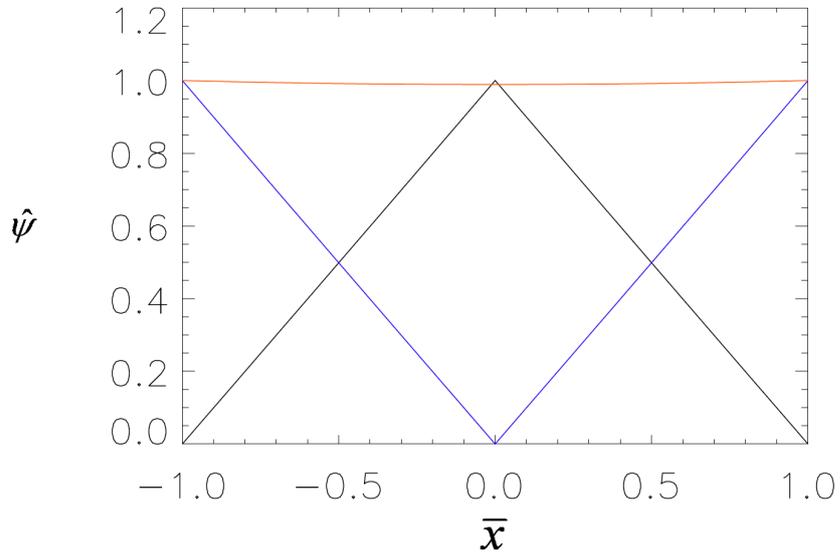
Figure 3.5: The outer region analytic solutions for the linear B_θ profile. $\hat{\psi}_m$ (black) is the mode solution and $\hat{\psi}_s$ (blue) is the shielded solution. The red curve is the normalise vacuum profile.

Upon initial application of the perturbation, shear Alfven waves develop in the outer region which are damped relatively quickly, giving rise to the qualitatively expected profiles displayed in figures 3.7 and 3.8 for $\jmath$ and φ respectively. It was explained in section 2.1.6 that the amount of reconnection can be quantified by measuring the radial magnetic flux at the rational surface $\hat{\psi}(0, t)$. It was further explained that at the rational surface the current density, $\jmath(0, t)$, is proportional to the rate of reconnection, $\partial\hat{\psi}/\partial t$. The expected temporal shape of $\jmath(0, t)$ for $t \ll \tau_E$ (blue) and $t \gg \tau_E$ (green) (τ_E being defined as in section 2.1.5) can be
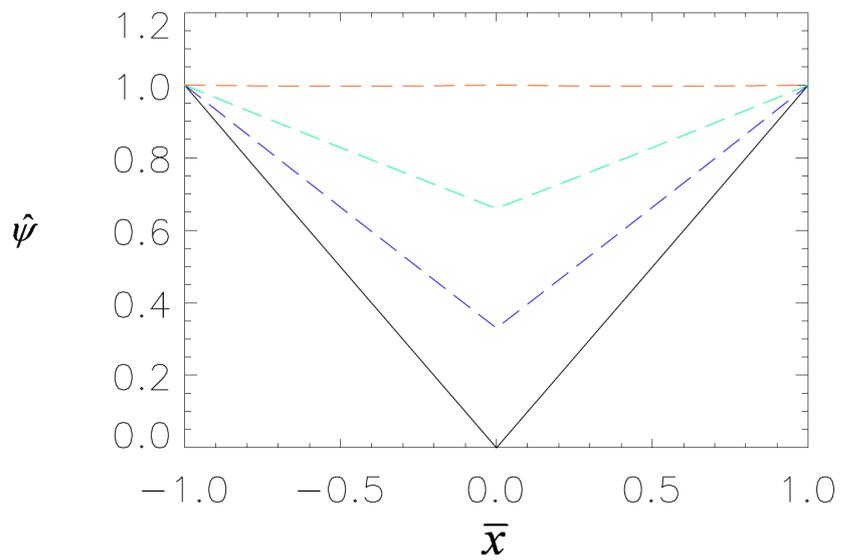
Figure 3.6: A qualitative picture of the expected temporal evolution of the normalised ψ profile. The solid black line is the expected $t = 0$ profile, whilst the red curve is the expected final reconnected state. The blue (earlier) and turquoise (later) are intermediate states.

calculated from 2.56 and 2.62, and is shown in figure 3.9. A numerically obtained BOUT++ profile with a slightly different parameters, but the same macroscopic qualitative features, is displayed in figure 3.10. A peak is expected to occur in the normalised time at $t \sim \tau_E$ (red vertical line)($t^{norm} \sim 1$), corresponding to the transition from the inertial (I) to the resistive inertial regime (RI) (as defined in section 2.1.6 and corresponding to the 1st peak in 3.10). In the limit $t \ll \tau_E$, $\jmath(0,t) \propto t$ (and is independent of resistivity). It is expected that the value of $\jmath(0,t)$ at this peak should scale $\sim \eta^{-1/3}$. The BOUT++ results are tested against the predicted scaling and the results displayed in figure 3.11.
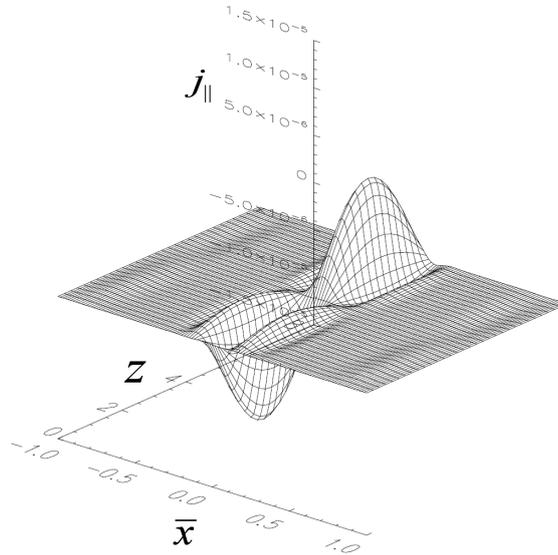
Figure 3.7: A demonstration of the expected outer region behaviour for the current density profile. $\bar{x}$ is the normalised radial coordinate, whilst z is the slab angle corresponding to the toroidal angle.

The decay dynamics of the layer current density in the resistive inertial regime is governed by the time scale τ_c. The current density, $\jmath(0,t)$, is expected to overshoot its final value crossing the time axis (blue vertical line in figure 3.9), corresponding in a maxima in the reconnected flux, $\psi(0,t)$. By examination of the asymptotic forms for the perturbed flux, equations 2.60 and 2.61, it is expected that time taken, t^{cross}, for the $\jmath(0,t)$ profile to cross the temporal axis should scale as $\sim \eta^{-3/5}$. The results of the BOUT++ code (crosses) are tested against
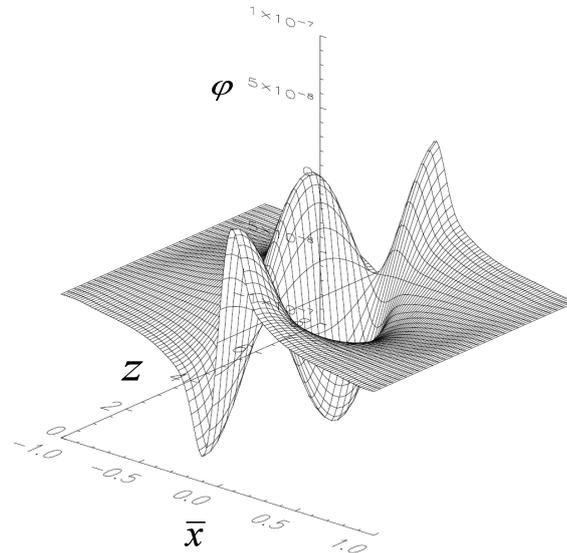
Figure 3.8: The qualitatively expected φ profile. $\bar{x}$ is the normalised radial coordinate, whilst z is the slab angle corresponding to the toroidal angle.
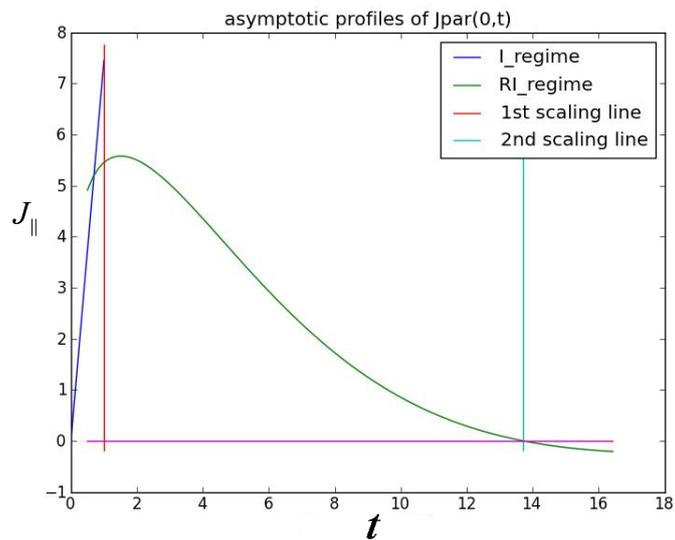
Figure 3.9: Analytic asymptotic profiles for $\jmath(0,t)$ in the inertial (blue) and resistive inertial (green) regimes
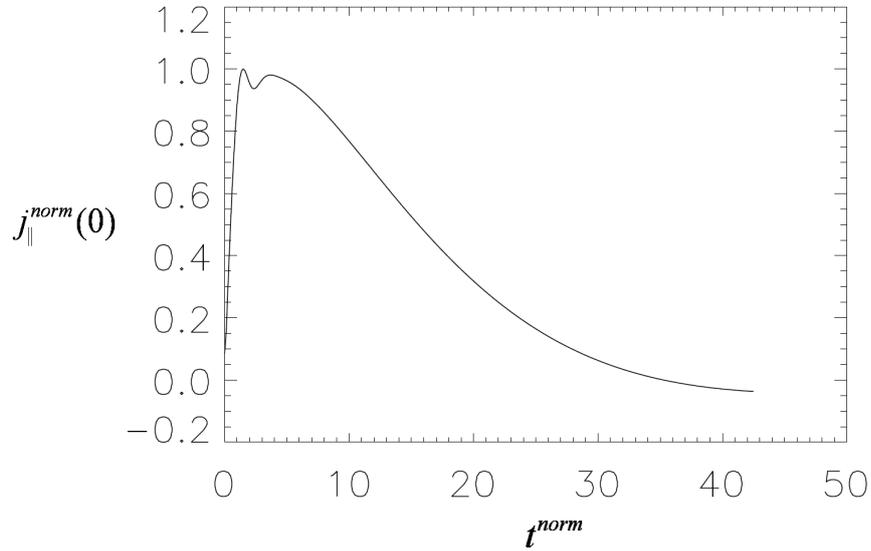
Figure 3.10: A typical BOUT++ profile for $\jmath(0, t)$ displaying the same qualitative behaviour as the analytic case. The temporal variable is normalised to τ_E. For the particular case shown $\eta = 5.0e^{-8}$.
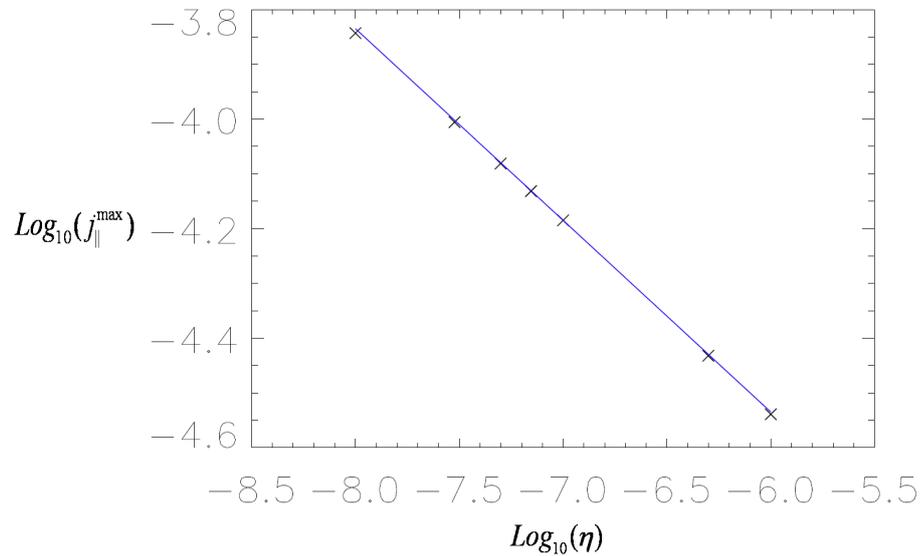
Figure 3.11: Scaling of the maxima in the reconnection rate for the inertial to resistive inertial transition (the solid line is the expected scaling from analytical results and has a gradient of -0.33)

the analytic scaling (solid blue line) and are displayed in figure 3.12.

Two peaks in the reconnection rate are observed in figure 3.10. The first occurs at the transition between the inertial and resistive inertial regimes. The second, slightly into the resistive inertial regime. There was some dispute as to which peak in the reconnection rate should have the largest absolute magnitude. Ultimately, the dispute was resolved numerical in [57]. The relative magnitude of the two peaks was found to be dependent on resistivity (more correctly ϵ, however the equilibrium remained unchanged in the BOUT++ scaling performed). The absolute value of the reconnection rate of the second peak is predicted to scale as $\sim \eta^{-2/5}$. Both scalings are reproduced in figure 3.13, a clear crossing point observed in the range of resistivities tested.
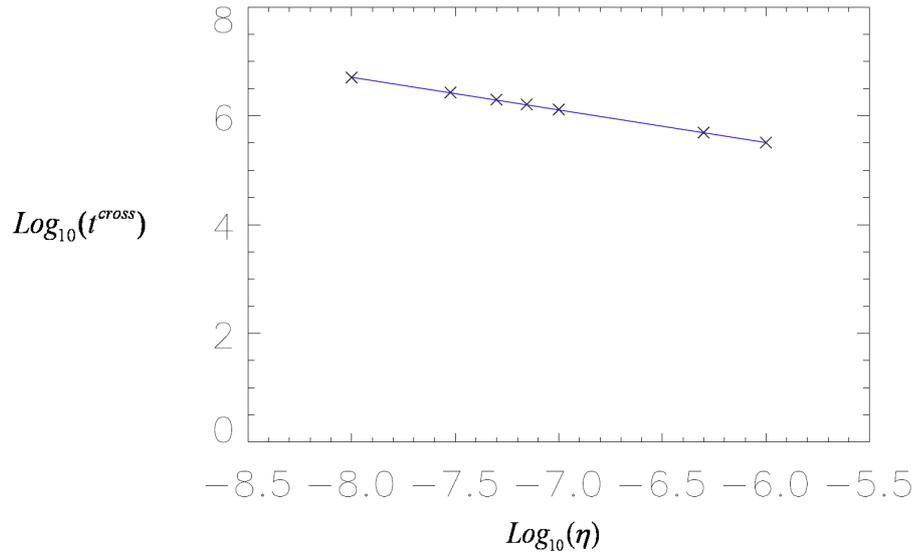
Figure 3.12: Scaling for the time to the maxima in the amount of reconnection (or the axis crossing point in the reconnection rate). The solid line is the analytic predicted scaling with a gradient of -0.6.

An interesting question which has yet to touched upon by previous authors, when considering rational surfaces is, 'What is the amount of radial grid packing required to produce accurate results in the vicinity of the rational surface?. The inviscid Taylor problem is ideal for testing the amount of radial grid packing which is required to obtain an accurate representation of the inner layer. This is
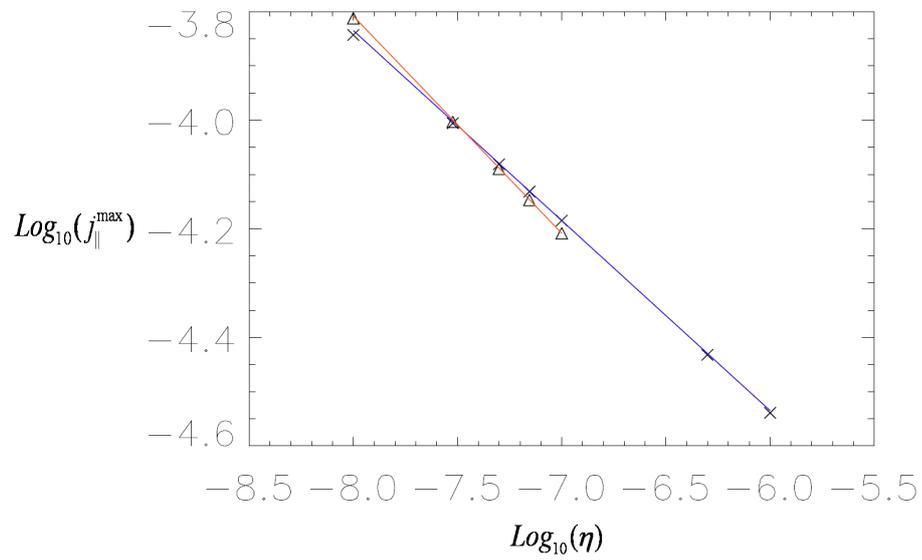
Figure 3.13: The scaling of magnitude of both peaks in the $\jmath(0,t)$ profile. The crosses are the BOUT++ results corresponding to the peak at the Inertial (I) to Resistive Inertial (RI) transition (first peak) with the blue line the analytic comparison. The triangles are BOUT++ results for the peak in the RI regime and the red line the analytic comparison.

an important question as it provides a balance between numerical economy and numerical accuracy. Numerical economy will be of great importance in multiple layer systems. An indication of the minimum number of grid points required to represent the actual solution with sufficient accuracy is therefore essential for these large scale computations. In reality the following procedure should be tested on every new equation set which alters the dynamics of the layer (for example the layer may contain sub-layers, with the inclusion of higher derivative terms, which may need to be resolved). An example of the effect of insufficient grid packing on the reconnection dynamics can be observed in figure 3.14. The figure displays the reconnection rate against time for a range of grids in the radial domain ($nx = 41, 51, 61, 91, 121, 151$), for a particular value of η ($\eta = 1e^{-7}$ for this case). It is observed that as the number of radial grid points increases, the solutions, $j_{\parallel}(0,t)$, tend to converge towards a common solution, $j_{\parallel}^{(conv)}(0,t)$. It is assumed that this common solution is the actual solution. Similar simulations are performed for a range of values for η ($\eta = 1 \times 10^{-8}, 5 \times 10^{-8}, 1 \times 10^{-7}, 5 \times 10^{-7}, 1 \times 10^{-6}$).
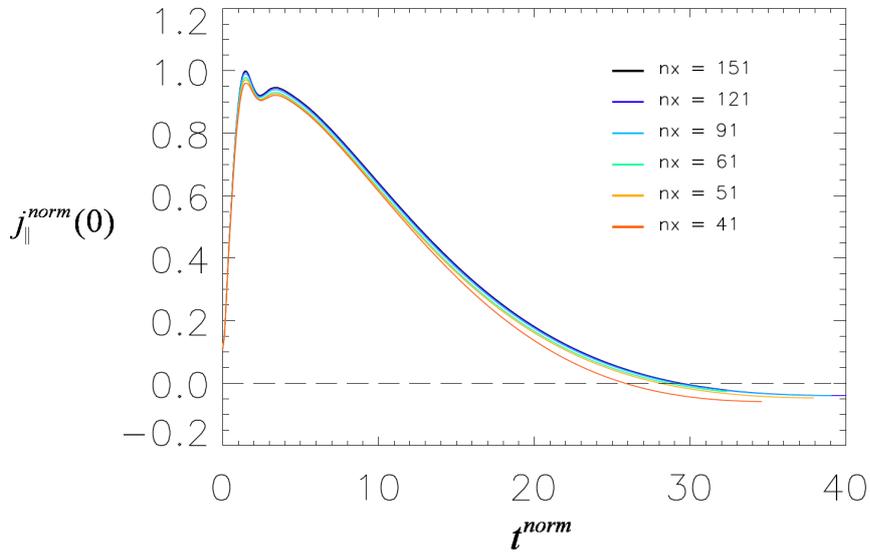
Figure 3.14: normalised $j_{\parallel}(0)$ vs normalise time. Time is normalised against τ_E (See section 2.1.5). nx is the number of radial grid points across the domain. $\eta = 1 \times 10^{-7}$ for this particular case.

An indication of the relative error of the solution, for a particular radial grid

packing, is measured at two different times. The first measure is the value of $j_{\parallel}(0)$ peak at the transition from the inertial to resistive inertial regime. Figure 3.15 displays the fraction $j_{\parallel}(0)/j_{\parallel}^{(conv)}(0)$ at this peak, against the number grid points in the radial domain $(j_{frac}^{max}j_{\parallel}(0)/j_{\parallel}^{(conv)}(0))$. For each value of the resistivity, simulations were carried out with an increasing number of grid points until the gradient of $j_{\parallel}(0)/j_{\parallel}^{(conv)(0)}$ against nx was sufficiently small (The assumed value used for $j_{\parallel}^{(conv)}(0)$ was the $j_{\parallel}(0)$ value for the simulation with the most number of grid points at that time). The solution was then deemed to have converged. It is observed that the relative error at this first peak, for a particular radial grid pack, appears to be independent of the resistivity (The crosses for each value of the resistivity, overlay each other in all cases when the same value of nx was used). Evidently the absolute error increases with decreasing η, as can be deduced from examining both figures 3.11 and 3.15, and will scale as $\eta^{-1/3}$. Hence, if a limit is set by the relative error, then a minimum number of grid points is required to reproduce the peak with sufficient accuracy. This minimum number appears to be independent of the resistivity.

The second measure is the time taken, t_{cross}, for the $j_{\parallel}(0,t)$ solution to cross the time axis. Figure 3.16 displays the quantity $t_{cross}/t_{cross}^{(conv)}$ against the number of radial grid points, for a range of resistivities ($t_{frac}^{cross} = t_{cross}/t_{cross}^{(conv)}$). Again $t_{cross}^{(conv)}$ is taken to be the time to cross for the largest value of the radial grid points tested. The number of radial grid points is then increased until the the gradient of $t_{cross}/t_{cross}^{(conv)}$ against nx becomes sufficiently small. It is observed that the relative error is no longer independent of resistivity, and that as the resistivity decreases the required number of of grid points increases. Attempts were made to obtain data for nx = 61 and 71 for the $\eta = 1e^{-8}$ case, however the solution diverged away from the actual solution to a sufficient extent, that the temporal axis was no longer crossed. It is interesting to note in figure 3.16 that the relative error for both $\eta = 1 \times 10^{-6}$ and $\eta = 5 \times 10^{-7}$ cases remain approximately the same until the number of radial grid points drops below $nx = 41$. It is possible that this error is actually due to the error accumulated in the inertial regime which has caused the solution to slightly alter trajectory. The relative error for $\eta = 1 \times 10{-7}$ also appears to tend towards the same values as $\eta = 1 \times 10^{-6}$ and $\eta = 5 \times 10^{-7}$ with a sufficient number of grid points. For all three of these

resistivities the solution also appears to converge for the same number of grid points as $j_\parallel(0)$ peak error analysis (figures 3.15 and 3.16).

The above would imply that there is a minimum required radial grid point packing. The minimum is set by the requirements of an accurate representation of the inertial regime, and the transition between the inertial and resistive inertial regimes. Above a threshold value in the resistivity, the minimum grid packing set by the inertial regime requirements are sufficient to produce accurate representations into the resistive inertial regime. However, once the resistivity drops below the threshold value, increasing radial grid packing is required, with decreasing resistivity, to ensure convergence in the resistive inertial regime.
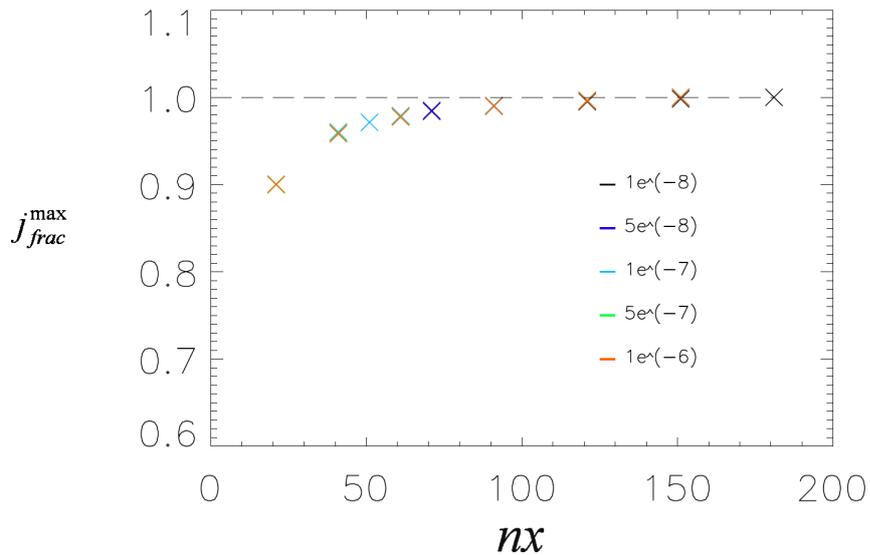
Figure 3.15: $j_\parallel(0)/j_\parallel^{(conv)}(0)$ at the inertial to resistive inertial transition peak, against the number of radial grid cells used. Curves are displayed for $\eta = 1 \times 10^{-6}$, 5×10^{-7}, 1×10^{-7}, 5×10^{-8}, 1×10^{-8}.

3.3 The inclusion of equilibrium flow

Equilibrium flow is included in the model by the inclusion of an equilibrium φ_0 profile with a constant radial gradient. The same equilibrium magnetic field
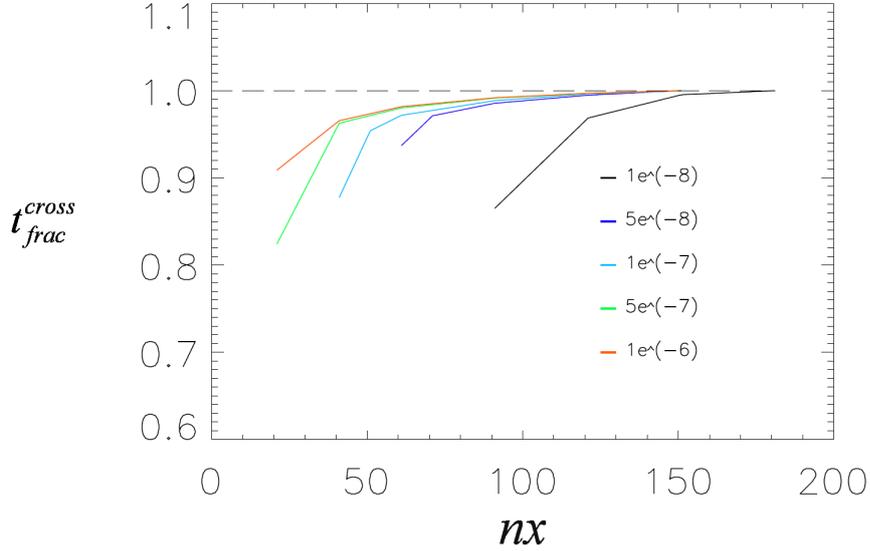
Figure 3.16: $t_{cross}/t^{conv}_{cross}$ against the number of radial grid cells used. Curves are displayed for $\eta = 1 \times 10^{-6}, 5 \times 10^{-7}, 1 \times 10^{-7}, 5 \times 10^{-8}, 1 \times 10^{-8}$.

parameters are used as in the previous subsection (section 3.2). The BOUT++ results are compared against the time asymptotic, $t \to \infty$, analytic results of section 2.1.7. With the presence of equilibrium flow a relative phase shift exits between the mode and shielded solution. A time asymptotic shielding current density profile remains. Figure 3.17 displays the final phase shifted current profile for the case of $Q_\Omega = 0.1$. Referring to section 2.1.7 Q_Ω is rotation frequency of the mode as seen by the plasma, normalized to τ_E.

Figures 3.18 - 3.21 display the time evolution of the quantity $|\Psi(r_s, t)/\Psi_{full}|$ (black solid line) for $Q_\Omega = 0.0, 0.3, 0.5, 0.7$ respectively (Ψ_{full} refers to the fully reconnected state in the absence of plasma flow. i.e. that solution for which the current sheet at the rational surface no longer exists). $|\Psi(r_s, t)/\Psi_{full}|$ is therefore a measure of the extent of magnetic field penetration at the rational surface. The time asymptotic analytic results are displayed by the dashed lines and are calculated using equation 2.71 using the asymptotic form for $\Delta(iQ_\Omega)$, $Q_\Omega \ll 1$. It is worth noting that because the asymptotic analysis is carried out in the limit $Q_\Omega \ll 1$, it is likely that the analytic approximations and numerical results will be in increasing better agreement as the limit is approached. The

oscillatory nature of the dynamic solutions is predicted by expanding the integral of equation 2.70 in a similar manor to equation 2.62, and is qualitative agreement with the results observed in the figures (no quantitative test was performed for the dynamic solution).
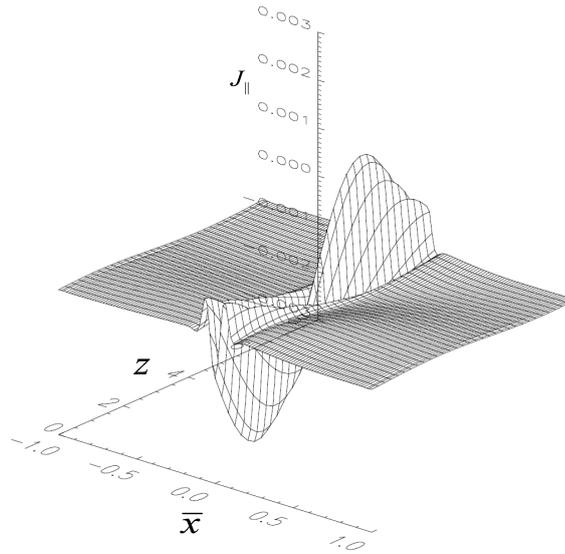
Figure 3.17: The time asymptotic current density profile with the inclusion of equilibrium flow ($Q_\Omega = 0.1$). $\bar{x}$ is the normalised radial coordinate, whilst z is the effective toroidal angle in the slab geometry. The phase shifted current density in the layer partially screens the radial magnetic field from reaching its fully reconnected state.

3.4 Inclusion of an equilibrium current gradient and viscosity

The equilibrium profile in now changed to include an equilibrium current gradient, $j_0' \neq 0$. The toroidal magnetic field remains unchanged, but the poloidal magnetic field has a profile $B_\theta = B_\theta(r_s) - A\tanh(x/L_x)$ (figure 3.22). The corresponding q profile is displayed in figure 3.23. The profiles are chosen so the plasma is now closer to marginal tearing stability to contrast with the previous case, the
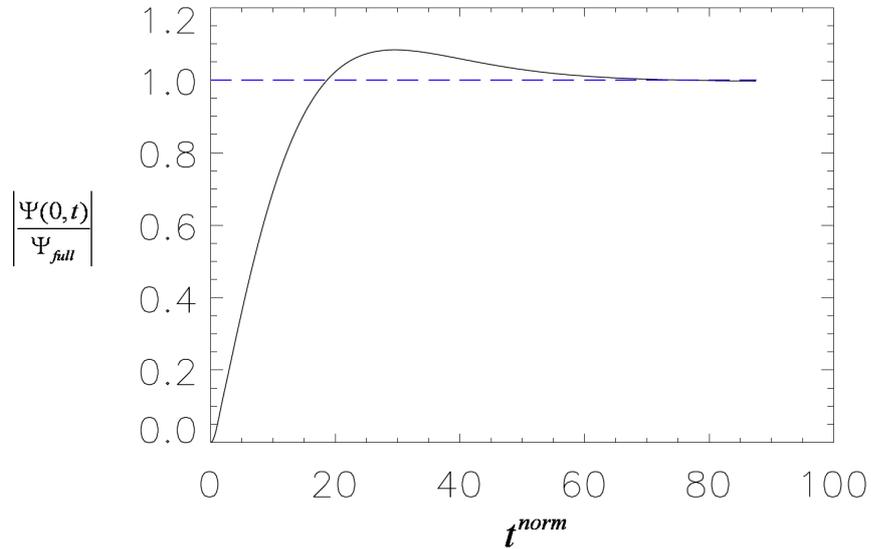
Figure 3.18: Temporal profile of the normalised reconnected flux (solid) at the rational surface and the steady state analytic comparison,$Q_\Omega = 0$. An over shoot is observed corresponding to the crossing of the temporal axis by the $\jmath_\parallel(0,t)$ profile referred to in section 3.2.
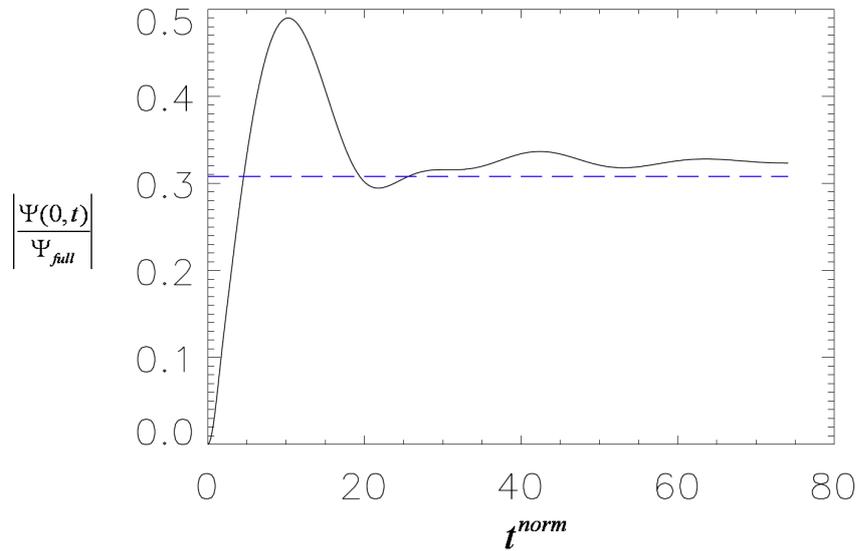
Figure 3.19: Temporal profile of the normalised reconnected flux (solid) and the steady state analytic approximation comparison,$Q_\Omega = 0.3$
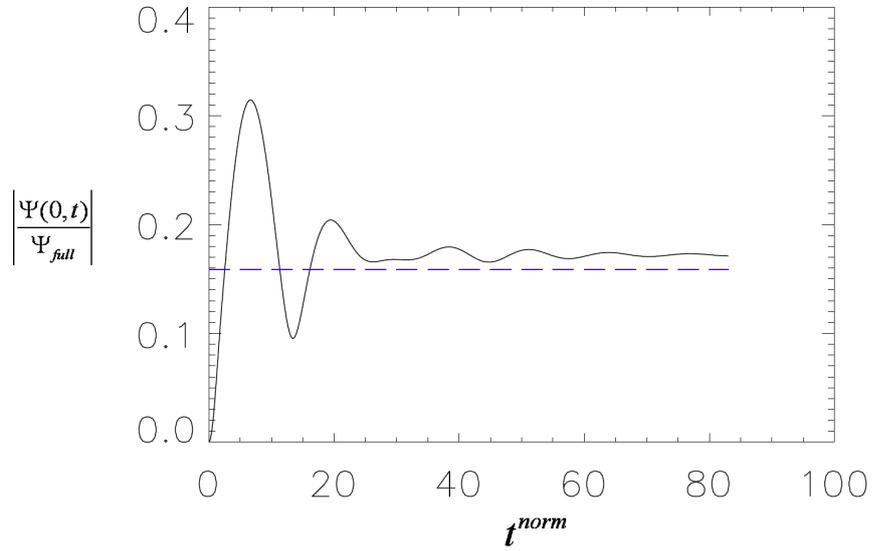
Figure 3.20: Temporal profile of the normalised reconnected flux (solid) and the steady state analytic approximation comparison, $Q = 0.5$
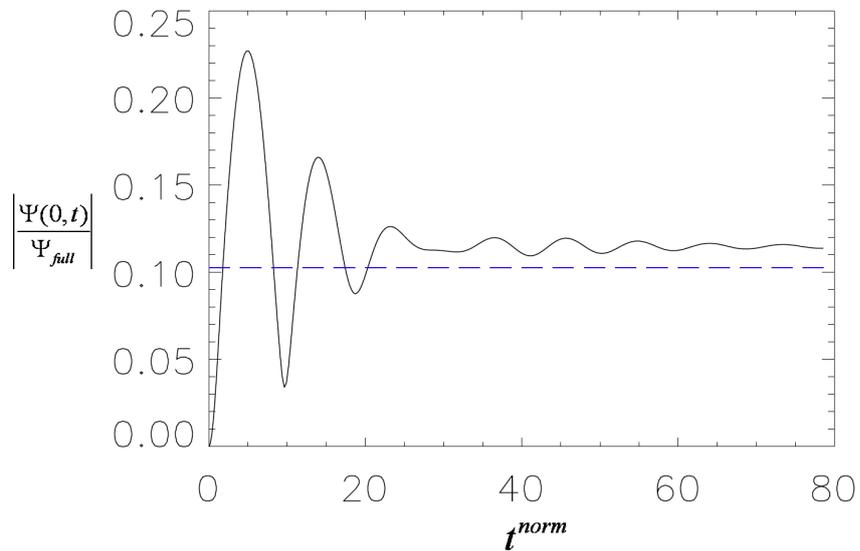
Figure 3.21: Temporal profile of the normalised reconnected flux (solid) and the steady state analytic approximation comparison, $Q_\Omega = 0.7$

amplification of the vacuum solution, Ψ_{full}/Ψ_v, is expected to be large for this scenario. The present configuration provides a more general test of the outer region solution, than in the previous subsection. It also allows a more general form of the boundary conditions to be tested. $\hat{\psi}_m$ and $\hat{\psi}_s$ profiles are displayed in figure 3.24, and are calculated by solving the outer solution (see section 2.1.4) differential equation:

$$\frac{\partial^2 \psi}{\partial x^2} - (k_\perp^2 + L_x^2 cosh^2(\frac{x}{L_x}))\psi = 0 \tag{3.5}$$

with the appropriate boundary conditions for the mode and shielded solutions. The mode and shield tearing indexes can then be calculated for the equilibrium.

$$\Delta_m' = -0.124 \qquad\qquad \Delta_s' = 2.826 \tag{3.6}$$
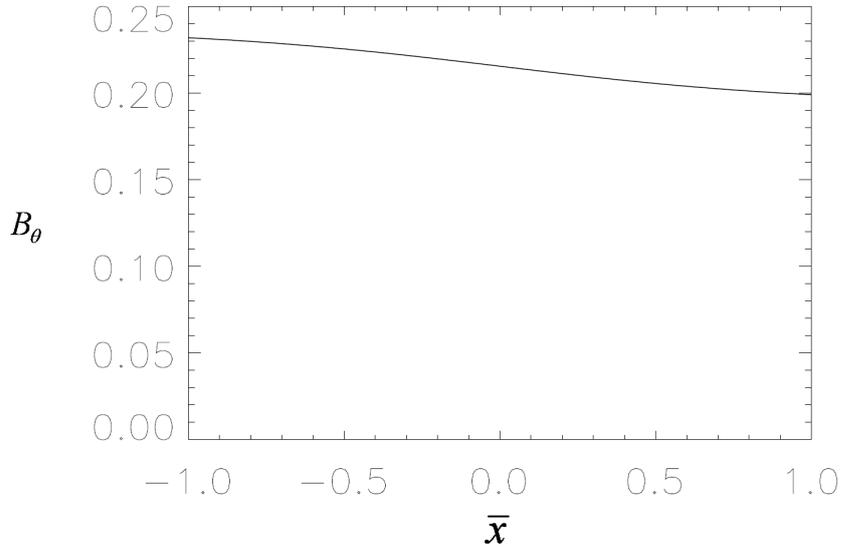
Figure 3.22: The tanh B_θ profile

Characteristic layer widths, $(\eta/k_{par}')^{1/3}$, were chosen to be ~ 0.1 of the characteristic length L_x. If the characteristic layer width was chosen to be substantially greater than this value, it was found that sheet currents formed at the boundaries of the radial domain. This was found to be increasingly more of a problem for sim-
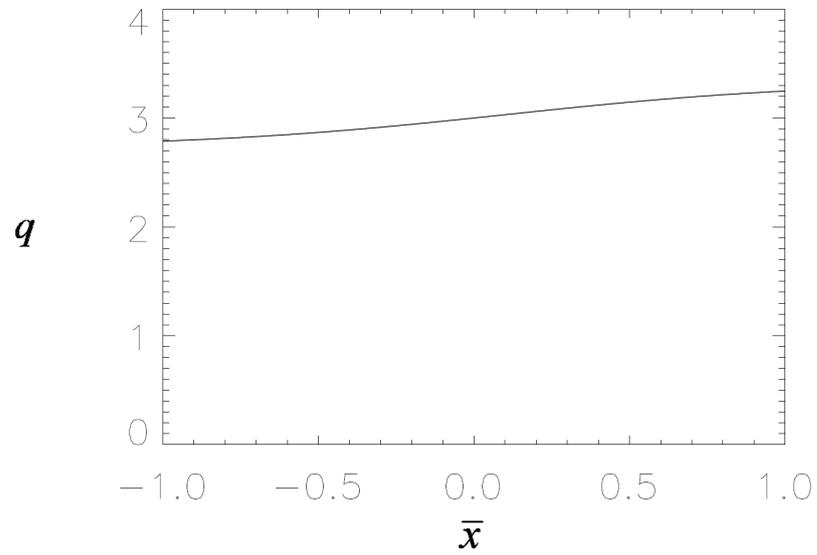
Figure 3.23: The corresponding q profile for the tanh B_θ profile
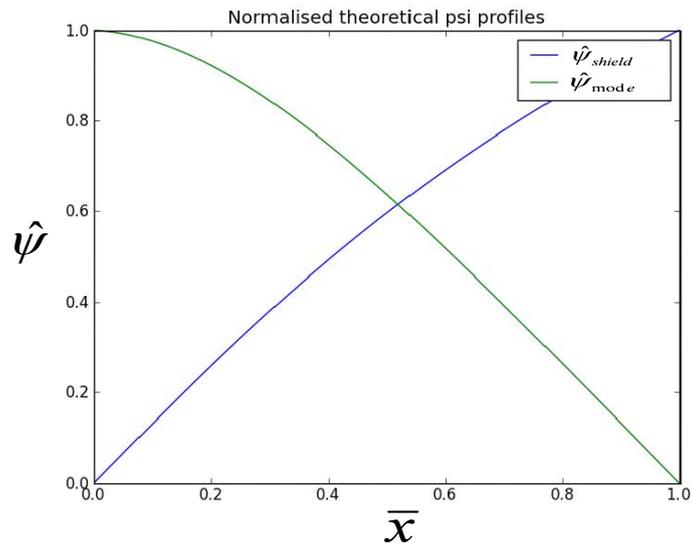
Figure 3.24: ψ_m (green) and ψ_s (blue)

ulations performed at higher rotation frequencies for which the actual layer width
(not the characteristic layer width) increases. For the simulations performed the
characteristic layer width was reduced, by altering either η or k'_{par} until the range
of simulations performed had smoothly matching boundaries. The boundaries
are set to the leading order outer region analytic approximation, which becomes
increasing more accurate the further away from the boundary layer the solution
is. Sheet currents set up at the boundary are therefore likely to be due to the
boundary layer still maintaining an impact on the outer region for the domain
size chosen. The perturbed current in the outer region is no longer expect to
be zero. The outer region was tested against the neighbouring equilibria solu-
tion (figure 3.25), the results being in good agreement (see section 2.1.4). Figure
3.25 displays a typical outer region numerical solution (black solid line). Note
that there is a smooth join to the boundary conditions for this example. The
red curve represents the analytic outer region approximation calculated by solv-
ing 2.39. It is noted that the analytic approximation becomes increasing more
accurate moving away from the boundary layer.

Simulations were performed with equilibrium flow and the addition of a small
amount of perpendicular viscosity. Similar dynamic profiles are obtained as for
figures 3.18 - 3.21. The final reconnected states, $t \to \infty$, for the BOUT++
simulations are summarised in figure 3.26 (red dots). The blue solid curve is the
analytic estimates in the resistive inertial regime.

3.4.1   Summary and Discussion

For the first time rigorous testing of the BOUT++ code has been performed
for reconnection type problems. The parallel current density at the rational
surface is proportional to the reconnection rate. Three different scalings were
performed. The first scaling measured the magnitude of $j_\parallel(0,t)$ at the peak
between the inertial and resistive inertial regimes, against resistivity. The second
scaling measured the magnitude of $j_\parallel(0,t)$ at the peak in the resistive inertial
regime, against resistivity. Finally the third scaling measured the time taken for
the $j_\parallel(0,t)$ profile to cross the temporal axis, against resistivity. All three scaling
were found to be in excellent agreement with the analytic predictions. A cross
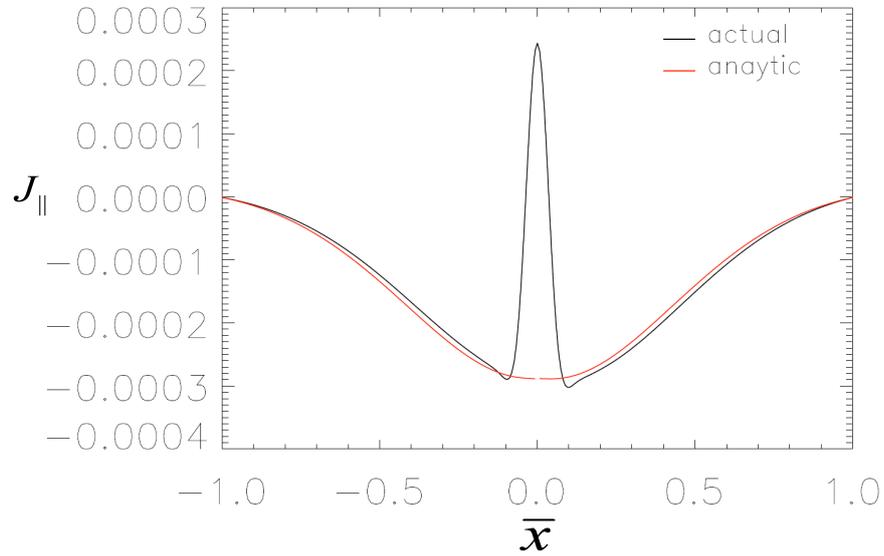
Figure 3.25: $\jmath$ from BOUT++ (black) and the outer region analytic comparison (red)
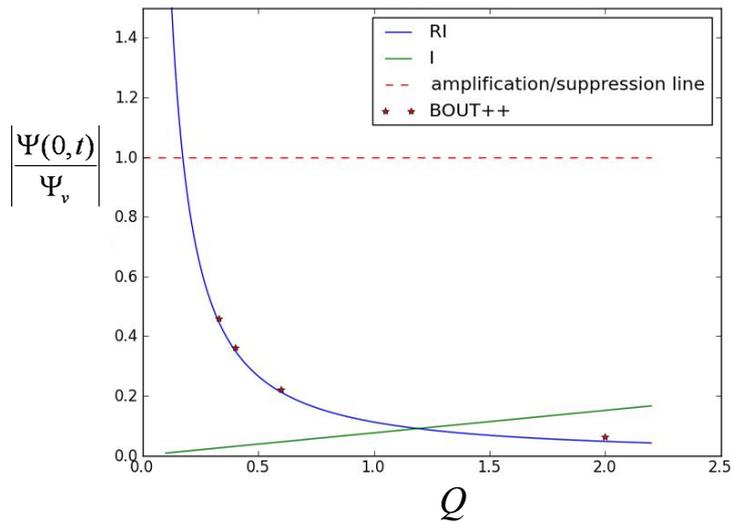
Figure 3.26: The final steady state BOUT++ results (red stars) and the resistive inertial analytic comparison (blue)

over point for the relative magnitude of the of the two $j_\parallel(0,t)$ peaks was also found in agreement with the results in [57].

Other authors, who were originally testing the validity of the analytic approximations, used 1-D or 2-D codes for which large number of grid cells could be packed in the radial direction. When considering 3-D codes with multiple rational surfaces, a trade off must be considered between numerical economy and numerical accuracy. A test was performed, which to the authors knowledge is the first of its kind when considering rational surface dynamics. The test set out to determine which section of the reconnection process required the most amount of grid packing, in order to obtain a numerical solution which was within acceptable limits of the actual solution. Ultimately it was found to be dependent on the resistivity. If a threshold in the relative error was taken to determine acceptable limits, then it was found that the inertial regime set an absolute minimum for the amount of radial grid packing required. The relative error was found to be independent of resistivity in this regime. However, the value of the resistivity then determined whether the relative error in the resistive inertial regime remand within acceptable limits. For high enough values of resistivity, the solution in the resistive inertial regime remained within the acceptable limits (i.e. the grid packing threshold was determined entirely by the inertial regime). Once the resistivity dropped below a critical value, then further radial grid packing was required in the resistive inertial regime. After this critical point, further decreasing the resistivity required additional increases in the grid packing. Ensuring the correct dynamics occur at the rational surface is essential not only for the dynamic reconnection type problem tested (i.e. obtaining correct magnetic island sizes etc.), but more generally for all RMP and error field problems in which boundary layers occur at the rational surfaces (i.e. obtaining the correct final suppressed reconnected states for sections)

Additional testing of the BOUT++ code was performed with the addition of an equilibrium velocity profile. The BOUT++ dynamic solutions were found to be in qualitative agreement with the predictions of analytic theory (no quantitative test was performed). The final suppressed states where tested quantitatively against the analytic asymptotic approximations in the limit $Q_\Omega \ll 1$, and found to be in good agreement. The analysis was then extended with the addition

of an equilibrium current gradient and perpendicular viscosity. Yet again both the BOUT++ dynamic profiles were found to be in qualitative agreement, and the final suppressed reconnected states in quantitative agreement, with analytic theory in the asymptotic limit $Q_\Omega \ll 1$. The accurate reproduction of linear layer suppressed states is a crucial step in ensuring that the non-linear $\mathbf{J} \times \mathbf{B}$ force, which is responsible for plasma braking, is correctly modelled in quasi-linear regimes. This is essential for obtaining accurate values of the perturbed magnetic field required to cause bifurcation, and for establishing the correct new equilibrium should bifurcation not occur. The importance of the quasi-linear regimes is twofold. Firstly they provide an important testing phase for island dynamics, before the island size exceeds the linear layer width and enters the non-linear regimes. Secondly because as the size of Tokamaks increase, it is estimated that the plasma response due to an error field will move from the non-linear Rutherford regime into quasi-linear regimes [19].

In addition the accurate reproduction of linear layer physics is an essential step for the comparison between the measured and modelled plasma displacement. Measurements of the plasma displacement provide a mechanism for comparing experimental and numerically modelled results, which can be an important step in validating proposed physical mechanisms and models. This area is expanded upon in [59].

A substantial amount of time was spent in ensuring that the boundary conditions were accurately reproduced in the simulations. This involved modifying the BOUT++ code to enable it to incorporate the more general class of boundary conditions. Experimenting with novel ways of implementing the boundary conditions to ensure that sheet currents were minimised between the guard and internal cells (especially with the introduction of plasma flow). Finally the boundary conditions are based on the outer region leading order analytic approximations. It was found to be necessary to check that the boundary layer width was sufficiently small, such that the numerical solution had enough radial domain to converge to the analytic solution. Again failure to allow a sufficient outer region radial domain resulted in the presence of unacceptably large current sheets between the guard and internal grid cells. This was a very important issue to solve for both RMP and error field studies. Magnetic perturbations are applied through the boundary

conditions. The presence of unintentional sheet currents leads to the boundary conditions differing from those desired. This will either lead in incorrect final state equilibrium, incorrect bifurcation thresholds, or numerical instability and a termination of the numerical run.

Chapter 4

Simplified multi-surface model with differential flow

4.1 Model motivation

An experimental observation presented in section 1.2.8.1 was that in the low collisionallity regime, a surface at which the perpendicular electron rotation, $\omega_{\perp e}$, is zero, appears to be required for ELM suppression. Close to this surface the electron perpendicular rotation will be small. Current layer theory would suggest that if a rational surface, with a given vacuum perturbation strength applied to it, were to be moved sufficiently close to the surface of $\omega_{\perp e} = 0$, then a bifurcation would occur.

Layer theory in the vicinity of a single rational surface is complex, and subject to many variable parameters depending on the plasma conditions in the region of interest. However, a basic understanding of many of the essential features of the 2-field model can be gained by studying simple induction motor theory. The theory involves a rotating conductor moving in a viscous fluid with an applied magnetic perturbation. The resulting torque balance curves are very similar to those of the constant ψ regimes presented in section 2.1.9. In particular the induction motor theory is closely related to the visco-resistive regime in quasi-linear tokamak theory [19]. As tokamak size continues to increase, it is predicted that rational surfaces subject to error fields will move from the Rutherford regime

into the visco-resistive regime.

Realistic models of Tokamak RMP experiments must use multiple rational surface models, since RMP coils produce magnetic spectrums with a range of harmonics. The move to modelling multiple rational surfaces is further complicated by the interaction between surfaces. RMP simulations with multiple rational surfaces have previously been carried in [39] and [59], [41]. Although attention was drawn to the region at which $\omega_{\perp e} = 0$ in [39] and [41], because of the increased penetration of the magnetic field in the vicinity of this region. No detailed analysis of the interaction between rational surfaces in this local region was considered. [56] considers the detailed interaction of two rational surfaces in the context of error fields, and describes how bifurcation thresholds are altered in the due to the interaction between surfaces. However, this analysis is carried out assuming that both surfaces are in the core plasma and does not consider the region around $\omega_{\perp e} = 0$. In this chapter a novel model is put forward to analyse the interaction between rational surfaces due to differential rotation. In the second half of the chapter particular attention will be focused on using the model to analyse the region around the $\omega_{\perp e} = 0$ location and to the authors knowledge this is the first time such an analysis has been carried out. The model utilizes many of the similarities between Tokamak plasma braking theory and induction motor braking theory, to reduce the number of variables involved. As will become apparent in this chapter, this enables clarity in identifying key parameters and physical mechanisms, whilst not detracting from the essential physics involved.

The model is first used to look at the interaction between two rational surfaces connected by differential rotation. Diamagnetic terms are not switched on so the electromagnetic forces on each surface causes the plasma to brake towards the zero in the ion velocity. In particular, the model used allows for graphing of equilibria in what will be know as ω space. The development of ω space allows for an increased understanding and classification of types of equilibria, and the bifurcation thresholds involved. A space labelled ψ space will also be used to analyse bifurcation thresholds in multi-rational surface system. Although discovered independently ψ space was first used for this purpose in [56]. Hender and Fitzpatrick [56] provides an indication that the qualitative features of the model proposed in this chapter agree with previous work.

Diamagnetic terms will then be introduced into the model, which is then utilised to look at the interaction between two rational surfaces around the radial location at which $\omega_{\perp e} = 0$. This is the first time that such an analysis has been carried out. In particular bifurcation theory is extended, to include a new class of equilibrium states and bifurcation thresholds. The unique shape ψ space diagram produced in this scenario may provide an explanation for the range of 'penetration thresholds' observed in low collionality RMP experiments [36]. Furthermore the particular proposed model allows the effect of radially moving the rational surface location on bifurcation thresholds to be examined. It will be shown that by moving rational surfaces across the location at which $\omega_{\perp e} = 0$, so called 'bifurcation windows' can be produced with the same qualitative features as the q_{95} windows observed in experiments [31].

The remainder of the chapter proceeds as follows. First a brief introduction to induction motor theory is given. Then in section 4.3 a novel model is put forward to analyse the interaction of multiple rational surfaces in the presence of differential rotation. Bifurcation analysis is performed on a two layer system for a problem relevant to error field analysis in Tokamaks and the results are displayed in both ω and ψ space. The ψ space bifurcation thresholds are found to be in qualitative agreement with those produced in [56]. The analysis is then expanded to incorporate diamagnetic effect, firstly the single layer system, then this is extended for the two layer system. For the first time bifurcation theory is then extended for rational surfaces either side of the location of $\omega_{\perp e} = 0$.

4.2   A summary of the single layer induction motor results

Figure 4.1 outlines the induction motor model as described in [15]. For simplicity no variation is assumed to occur in the z direction (i.e. $\partial/\partial z = 0$). The following is a brief description of the system and the assumptions applied to it.

A rotating set of coils exists at radius r_c, with rotation frequency ω_c.

- Assumption: The coil set produces a magnetic field with only a single poloidal harmonic, m.
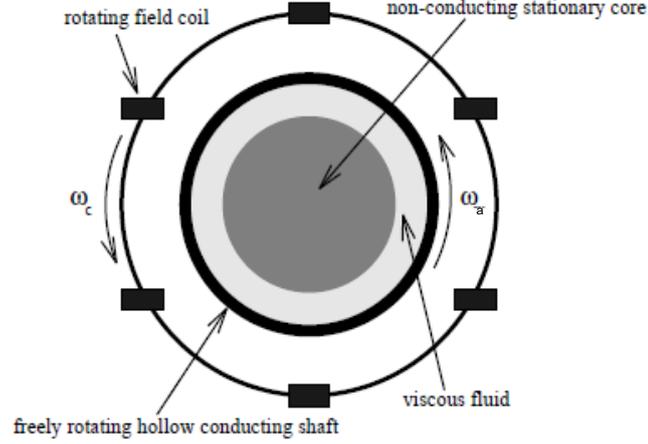
Figure 4.1: Components of the induction motor model [15]

A rotating cylindrical conducting armature exists with radius r_a.

- armature thickness $= \delta_a$

- It is assumed $0 < \bar{\delta} = \delta/r_a \ll 1$ and serves as an expansion parameter.

- armature angular frequency $= \omega_a$

- a constant resistivity is assumed, η

- currents induced in the armature are assumed to have the same poloidal frequency, m, as the applied field, although phase changes may occur.

A non-conducting stationary core exists with radius $r_a - d$.
A non-conducting viscous fluid exists between the core and the armature.

- The viscosity, μ, is assumed constant.

The magnetic field is made up of contributions from currents in the coil and induced currents in the armature. The magnetic field and current have the form:

$$\delta \mathbf{B} = \nabla \psi \times \hat{\mathbf{e}}_z \tag{4.1}$$

$$\mu_0 \delta \mathbf{J} = \nabla \times \delta \mathbf{B} = -\nabla^2 \psi \hat{\mathbf{e}}_z + \delta \mathbf{J}_\theta \tag{4.2}$$

with an assumed steady state form for ψ:

$$\psi(r, \theta, t) = \tilde{\psi}(r) e^{im(\theta - \omega_c t)} \tag{4.3}$$

Outside the coil and armature the solution must obey:

$$\nabla^2 \psi = 0 \tag{4.4}$$

while in the armature the B field evolution equation can be obtained from Ohm and Faraday's Laws:

$$\mathbf{E} + \mathbf{V} \times \mathbf{B} = \eta \mathbf{J} \tag{4.5}$$

$$\frac{\partial \mathbf{B}}{\partial t} = -\nabla \times \mathbf{E} \tag{4.6}$$

The evolution equation for ψ is obtained by taking the $\hat{\mathbf{e}}_r \cdot$ component of the above.

$$-im\omega_c \psi + im\omega_a \psi = \frac{\eta}{\mu_0} \nabla^2 \psi \tag{4.7}$$

with $\mathbf{v} = r\omega_a \hat{\mathbf{e}}_\theta$.. Defining the slip frequency as $\omega = \omega_a - \omega_c$:

$$im\omega\psi = \frac{\eta}{\mu_0} \nabla^2 \psi \tag{4.8}$$

Expanding the right hand side and using the change of variables, $\overline{x} = (r - r_a)/\delta_a$:

$$i\bar{\delta}^2 \frac{\mu_0}{\eta} r_a^2 m\omega\tilde{\psi} = \left(\frac{d^2}{d\bar{x}^2} + \frac{\bar{\delta}}{(1 + \bar{\delta}\bar{x})} \frac{d^2}{d\bar{x}^2} - \frac{m^2 \bar{\delta}^2}{(1 + \bar{\delta}\bar{x})^2} \right) \tilde{\psi} \tag{4.9}$$

In the limit $\bar{\delta} \to 0$, $\overline{x}$ fixed, the leading order term has the form of a resistive slab.

$$i\bar{\delta}^2 \frac{\mu_0}{\eta} r_a^2 m\omega\tilde{\psi}_0 = \frac{d^2 \tilde{\psi}_0}{d\bar{x}^2} \tag{4.10}$$

This assumes the quantity $(\mu_0/\eta)r_a^2 m\omega = O(1/\bar{\delta}^2)$ as $\bar{\delta} \to 0$. Using the interme-

diate variable $\overline{x}_\alpha = \alpha \overline{x}$ it is found that equation 4.10 remains leading order and that $\tilde{\psi}$ is approximately constant across the armature if $1 \ll (\mu_0/\eta)r_a^2 m\omega \ll 1/\overline{\delta}^2$ as $\overline{\delta} \to 0$. Converting back to the original variables, defining $\tau = \mu_0 \delta r_a/(2\eta)$ and $\overline{\omega} = \omega \tau$, and integrating across the armature

$$i\overline{\omega} = \frac{r_a}{\Psi_a}[\frac{\partial \tilde{\psi}}{\partial r}]_{r^-}^{r^+} \tag{4.11}$$

with $\tilde{\psi}(r_a) = \Psi_a$.

4.2.1 ψ profiles

The coils can be modelled by a sheet current, at r_c, which produces the particular vacuum perturbation of interest. The expansion of equation 4.4 is Euler's equation with a general solution:

$$\tilde{\psi}(r) = A_1 r^m + \frac{A_2}{r^m} \tag{4.12}$$

For any solution, ψ must remain finite in the limits $r \to 0$ and $r \to \infty$. The vacuum solution has the form:

$$\begin{aligned}
\tilde{\psi}_v(r) &= \Psi_v^{(c)}(\frac{r}{r_c})^m & (r < r_c) \\
\tilde{\psi}_v(r) &= \Psi_v^{(c)}(\frac{r}{r_c})^{-m} & (r > r_c)
\end{aligned} \tag{4.13}$$

The constant $\Psi_v^{(c)}$ is the vacuum $\tilde{\psi}$ value at the coil. A jump discontinuity exists in $d\tilde{\psi}_v/dr$ across r_c, which is proportional to the surface current.

For the rotating armature, with an approximately constant $\tilde{\psi}(r_a) = \Psi_a$ and $\tilde{\psi}_v(r_a) = \Psi_v^{(a)}$ throughout the armature:

$$\begin{aligned}
\tilde{\psi}(r) &= \Psi_a(\frac{r}{r_a})^m & (r < r_a) \\
\tilde{\psi}(r) &= \Psi_a(\frac{r}{r_a})^{-m} + \Psi_v^{(a)}((\frac{r}{r_a})^m - (\frac{r}{r_a})^{-m}) & (r_a < r < r_c) \\
\tilde{\psi}(r) &= \Psi_a(\frac{r}{r_a})^{-m} + \Psi_v^{(a)}(\frac{r}{r_a})^{-m}((\frac{r_a}{r_c})^{-m} - 1) & (r_c < r)
\end{aligned}$$
(4.14)

The combination of equations 4.11 and 4.14, yields an expression for the amplification factor.

$$\Psi_a = \frac{\Psi_v^{(a)}}{1 + i\overline{\omega}}$$
(4.15)

It is noted for the induction motor that the relaxed state, $\overline{\omega} \to 0$, is just that of the vacuum field (i.e. unlike in a plasma the amplification factor is constrained to be ≤ 1).

4.2.2 Torque balance and bifurcation

A component of the electromagnetic (EM) torque will act to reduce the magnitude of the slip frequency.

$$T_{\theta EM} = \int_{r^-}^{r^+} \oint r f_{\theta EM} r d\theta dr$$
(4.16)

The particular form for the EM torque can be obtained by considering equations 4.15 and 4.16 along with the complex conjugate forms.

$$\begin{aligned}
T_{\theta EM} &= -\frac{4\pi m}{\mu_0}\overline{\omega} \mid \Psi_a \mid^2 \\
&= -\frac{4\pi m}{\mu_0}\frac{\overline{\omega}}{1 + \overline{\omega}^2} \mid \Psi_v^{(a)} \mid^2
\end{aligned}$$
(4.17)

The poloidal velocity at the interface of the viscous fluid and a solid object is assumed to be equal. The viscous torque per unit length has the form (with $d/r_a \ll 1$)

$$
\begin{aligned}
T_{\theta VS} &= \int_{r^-}^{r^+} \oint r f_{\theta VS} r d\theta dr \\
&\approx -\frac{4\pi\mu r_a^3}{\tau_a d}(\overline{\omega} + \omega_c) \\
&= -\frac{4\pi\mu r_a^3}{\tau_a d}(\overline{\omega} - \omega_0) \tag{4.18} \\
f_{\theta VS} &= \mu \hat{\mathbf{e}}_\theta \cdot \nabla^2 \mathbf{V} \tag{4.19}
\end{aligned}
$$

ω_0 is introduced to agree with subsequent notation.

Steady state equilibrium points may be determined from balancing the EM and viscous torques, $T_{\theta EM} + T_{\theta VS} = 0$. If the coil current is ramped sufficiently slowly, the system will remain in approximate equilibrium until critical thresholds are crossed. The induction motor system described may undergo a downward bifurcation if $|\ \Psi_v^{(a)}\ | > |\ \Psi_v^{(a)}\ |^{(\downarrow)}$ or an upward bifurcation if $|\ \Psi_v^{(a)}\ | < |\ \Psi_v^{(a)}\ |^{(\uparrow)}$ (figure 4.2 left and right respectively) depending on the system equilibrium position.
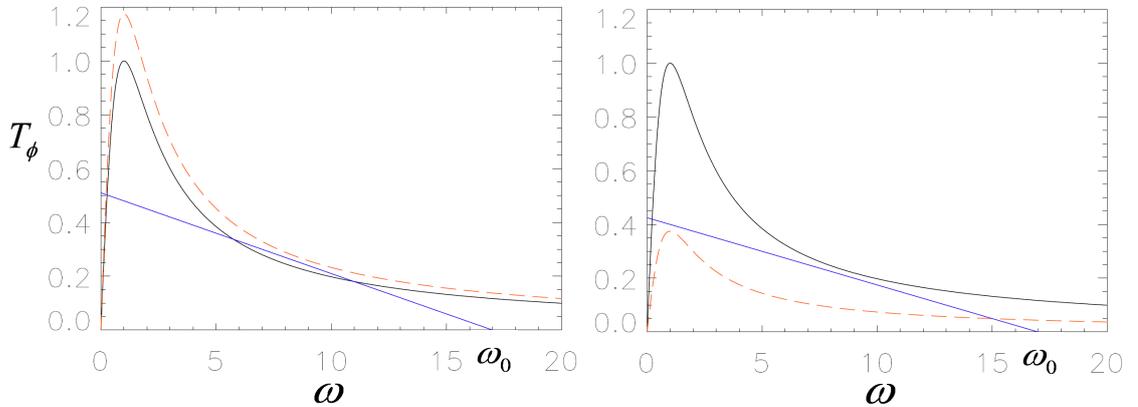
Figure 4.2: (left) The downward bifurcation. $|\ \Psi_v^{(a)}\ | > |\ \Psi_v^{(a)}\ |^{(\downarrow)}$ (red curve). (right) The upward bifurcation. $|\ \Psi_v^{(a)}\ | < |\ \Psi_v^{(a)}\ |^{(\uparrow)}$ (red curve)

4.3 Multiple layers connected by differential rotation

The model presented in the next subsection is in many respects similar to the zero beta 2-field model. The model will be further developed to include similar torque off-sets observed with the inclusion of electron diamagnetic terms in the 3-field models.

4.3.1 Model, assumptions, and normalisations

4.3.1.1 Equilibrium and System
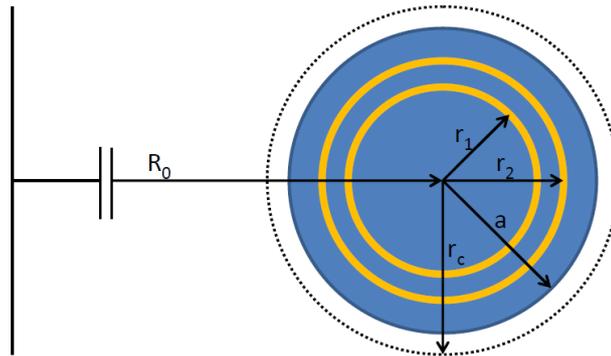
Figure 4.3: Model outline. Conducting surfaces exist at r_1, and r_2. Surface currents representing the RMPs are driven at r_c.

The system consists of a periodic cylinder, with major radius offset R_0, minor radius a, and periodicity length $2\pi R_0$. A collection of 'conducting surfaces' are placed at positions $\{r_1, r_2, ...\}$, with resistivities $\{\eta_1, \eta_2, ...\}$, and thickness $\{\delta_1, \delta_2, ...\}$. However, an assumption is that each 'conducting surface' is only conducting to a single pre-specified harmonic, $e^{i(m\theta - n\phi)}$, appearing as an effective vacuum to all other harmonics. The large aspect ratio assumption, $a/R_0 \ll 1$, is also invoked so that the leading order magnetic field may be written in the form of equation 4.1. Surface currents are driven at radius r_c to produce the particular magnetic perturbations, and so act as an effective set of RMP coils.

A non-conducting viscous fluid exists between the conducting surfaces, extending out to the minor radius. The poloidal velocity is assumed to be zero throughout the equilibrium. Poloidal electromagnetic torques may exist at the conducting surfaces, however the poloidal velocity is assumed to remain zero to reflect the strong parallel viscosity existing in actual tokamak plasmas. The toroidal viscous force per unit volume is assumed to have the simple form:

$$f_{\phi VS} = \mu \nabla^2 V_\phi \qquad (4.20)$$

The viscosity is assumed constant across the plasma purely for simplicity.

An initial equilibrium velocity profile is invoked by applying an effective Neutral Beam Injection torque, T_{NBI}, at a particular radius r_{NBI}. A toroidal viscous torque must exist at this point to balance T_{NBI}, resulting in a jump discontinuity in dU_ϕ/dr across this surface.

$$
\begin{aligned}
T_{\phi VS} &= \mu \int_{r^-}^{r^+} \oint \oint R_0 \nabla^2 V_\phi r d\theta R_0 d\phi dr \\
&= (2\pi R_0)^2 r_{NBI} \mu \left(\frac{dV_\phi}{dr} \big|_{r^+} - \frac{dV_\phi}{dr} \big|_{r^-} \right) \qquad (4.21)
\end{aligned}
$$

Elsewhere, with no perturbations applied, the equilibrium viscous torque is zero. The equilibrium velocity profile (figure 4.4), has the following form:

$$
\begin{aligned}
V_\phi(r) &= C_1^{(i)} & (r < r_{NBI}) \\
V_\phi(r) &= C_1^{(o)} + \frac{C_2^{(o)}}{r} & (r_{NBI} < r < a) \qquad (4.22)
\end{aligned}
$$

$C_2^{(i)} = 0$ so that the velocity remains finite at $r = 0$. The values of the constants are found by considering torque balance, $T_{NBI} + T_{\phi VS}(r_{NBI}) = 0$, and the boundary condition, $V_\phi(a) = 0$.

$$C_2^{(o)} = \frac{r_{NBI} T_{NBI}}{(2\pi R_0)^2 \mu} \tag{4.23}$$

$$C_1^{(o)} = -\frac{C_2^{(o)}}{a} \tag{4.24}$$

$$C_1^{(i)} = C_1^{(o)} + \frac{C_2^{(o)}}{r_{NBI}} \tag{4.25}$$
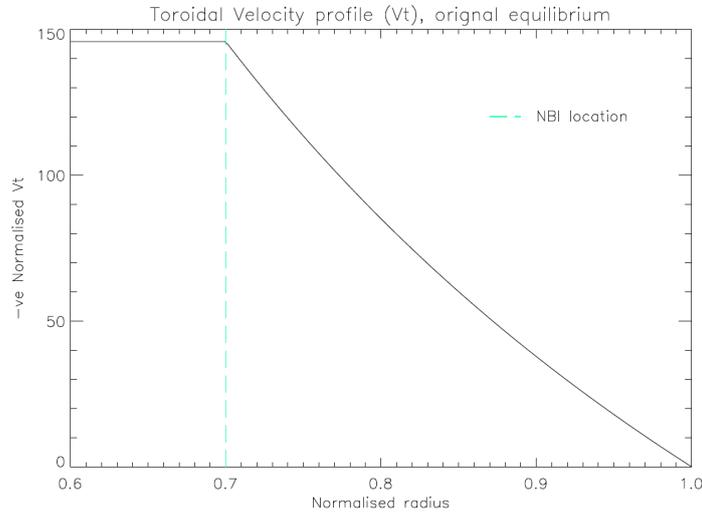
Figure 4.4: The original normalised equilibrium toroidal velocity profile. The effective NBI torque location is displayed.

.

4.3.2   Evolution equation and ψ profiles

Following a similar argument presented in section 4.2, with $\psi_{mn} = \tilde{\psi}_{mn}(r) exp(i(m\theta - n\phi) - \omega_c t)$, the particular conducting surface which responds to the m, n harmonic has an evolution equation:

$$\frac{\partial \psi_{mn}}{\partial t} + \mathbf{V} \cdot \nabla \psi_{mn} = \frac{\eta}{\mu_0} \nabla^2 \psi_{mn} \tag{4.26}$$

This leads to a similar form to equation 4.11.

$$i\omega_{(s)}\tau_{(s)}\Psi_{(s)} = r_{(s)}[\frac{d\tilde{\psi}_{(s)}}{dr}]_{r^-}^{r^+} \tag{4.27}$$

$$\omega = \frac{m}{r_{(s)}}V_\theta - \frac{n}{R_0}V_\phi - \omega_c \tag{4.28}$$

The notation $\psi_{(s)}$ corresponds to the surface at $r_{(s)}$ which is the surface which responds to the m, n harmonic. The constant ψ approximation is also assumed, and for the particular case of interest, $V_\theta = \omega_c = 0$.

The outer region must still obey $\nabla^2\psi = 0$. To leading order in the large aspect ratio approximation the $\tilde{\psi}(r)$ profiles remain the same as those of equations 4.14.

4.3.2.1 Torque Balance

When a magnetic perturbation of a specific harmonic is applied, the rotating conductor, which responds to that particular harmonic, will experience an EM torque. The poloidal EM torque is given by:

$$T_{\theta EM}^{(s)} = (2\pi)^2 R_0 \int_{r^-}^{r^+} r^2 f_{\theta EM}^{(s)} dr \tag{4.29}$$

The toroidal EM torque can be related to the poloidal EM torque via the relation:

$$T_{\phi EM}^{(s)} = -\frac{n}{m}T_{\theta EM}^{(s)} \tag{4.30}$$

Steady state equilibria solutions are searched for, in which the EM torque, $T_{\phi EM}^{(s)}$, at surface r_s, is balanced by a corresponding viscous torque, $T_{\phi VS}^{(s)}$, at that surface. i.e. solutions satisfying the set of equations:

$$\begin{aligned}
T_{\phi EM}^{(1)} &= -T_{\phi VS}^{(1)} \\
T_{\phi EM}^{(2)} &= -T_{\phi VS}^{(2)} \\
T_{\phi EM}^{(3)} &= -T_{\phi VS}^{(3)} \\
etc..&
\end{aligned} \tag{4.31}$$
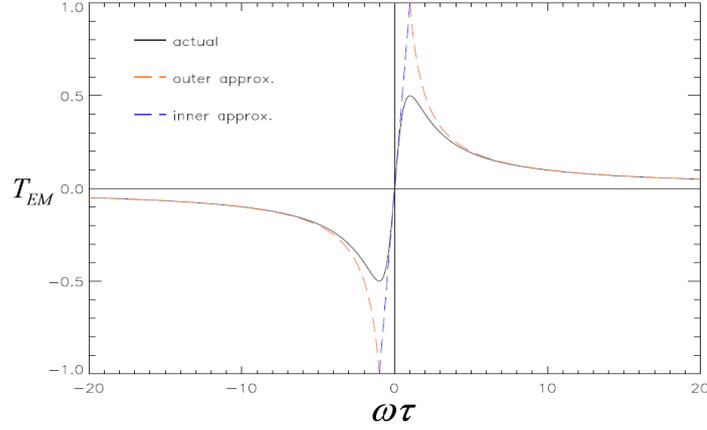
Figure 4.5: Normalised EM torque profile with its $\omega\tau \ll 1$ (inner) and $\omega\tau \gg 1$ (outer) approximations.

The viscous torque at each surface has a similar form to equation 4.21:

$$T_{\phi VS}^{(s)} = -(2\pi)^2 \frac{R_0^2}{r_s} \mu (C_2^{(s+1)} - C_2^{(s)}) \tag{4.32}$$

with constants:

$$C_2^{(s)} = \frac{r_s r_{s-1}}{(r_s - r_{s-1})} (V_\phi(r_{s-1}) - V_\phi(r_s)) \tag{4.33}$$

4.3.2.2 Normalisations

The normalisation scheme adopted is made for ease of comparison between changing physical variables.

Length scales are normalised to the minor radius, a, whilst time scales are normalised to $\tau_n = \mu_0 a \delta_n / \eta_n$. η_n and δ_n are typical values of the resistivity and conductor widths respectively. Additional normalisations are defined as follows:

$$\overline{T}_\phi = \frac{T_\phi \tau_n}{(2\pi)^2 R_0^3 \mu} \tag{4.34}$$

$$\overline{\omega}_s = \omega_s \tau_n \tag{4.35}$$

In the rest of this chapter over-bars will be dropped for ease of notation.

4.3.3   Constraint regions and stable equilibria

For the sections below a two 'rational surface' system is considered. The presence
of the NBI torque is incorporated into the viscous torque at surface 1, by the
addition on an offset term.

$$T_{\phi VS}^{(1)} = (M_{11}\omega_1 + M_{12}\omega_2 - G_1 T_{NBI}) \tag{4.36}$$

$$T_{\phi VS}^{(2)} = (M_{21}\omega_1 + M_{22}\omega_2) \tag{4.37}$$

with the constants $M_{i,j}$ and G_i given by:

$$
\begin{aligned}
M_{11} &= \frac{1}{n_1}\frac{r_2}{(r_2 - r_1)} & M_{12} &= -\frac{1}{n_2}\frac{r_2}{(r_2 - r_1)} \\
M_{21} &= -\frac{1}{n_1}\frac{r_1}{(r_2 - r_1)} & M_{22} &= \frac{1}{n_2}\frac{r_3}{(r_3 - r_2)} \\
G_1 &= -\frac{r_{NBI}}{r_1}
\end{aligned}
\tag{4.38}
$$

The EM torque equations have form:

$$T_{\phi EM}^{(1)} = n_1 m_1 |\Psi_v^{(1)}|^2 \frac{\omega_1\tau_1}{1 + (\omega_1\tau_1)^2} \tag{4.39}$$

$$T_{\phi EM}^{(2)} = n_2 m_2 |\Psi_v^{(2)}|^2 \frac{\omega_2\tau_2}{1 + (\omega_2\tau_2)^2} \tag{4.40}$$

$|\Psi_v^{(s)}|$ is the vacuum perturbation strength measured at r_s, of the harmonic which
interacts with (s). The notation $|\Psi_{vc}^{(s)}|$ is used to represent the vacuum pertur-
bation strength as measured at r_c. The two are simply related for the particular
model.

$$\Psi_{vc}^{(s)} = \Psi_v^{(s)}(\frac{r_s}{r_c})^{-m_s} \tag{4.41}$$

The set of points containing all possible combinations of the relative rotation

frequencies of the two surfaces, will henceforth be referred to as ω space. It is
assumed that there is no EM coupling between surfaces.

Constraint regions displaying the possible locations of steady state solutions
(i.e. those satisfying equations 4.31), can be obtained by plotting all lines of
$T_{\phi EM} = 0$ and $T_{\phi VS} = 0$ onto the same graph in ω space. By consideration of
the signs of $T_{\phi EM}$ and $T_{\phi VS}$ to either side of these lines the constraint region
may be obtained (figure 4.6). The size and relative position of the vertices may
change depending on the constants appearing in the viscous torque equation.
The intersection point of the lines of $T_{\phi VS}^{(1)} = 0$, and $T_{\phi VS}^{(2)} = 0$, is the equilibrium
point of the steady state solution before any external perturbations are applied.
The combination of the positive gradient of the $T_{\phi VS}^{(2)} = 0$ line and that this line
must pass through the origin, only permits steady state solutions to exist in two
quadrants, $\omega_1, \omega_2 > 0$ and $\omega_1, \omega_2 < 0$.
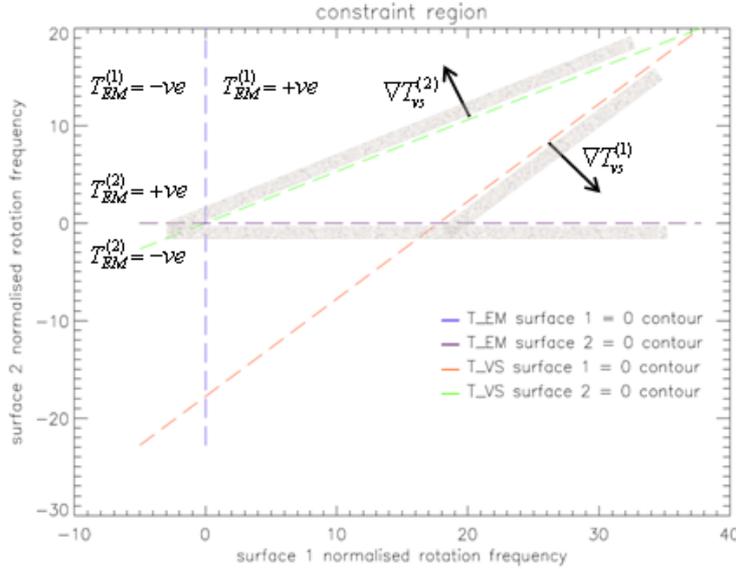
Figure 4.6: Constraint regions of possible steady state equilibria

.

It is assumed that magnetic perturbations are applied over sufficiently large
time-scales, that the system is always in effective equilibrium (This condition is
dependent on the movement of the particular equilibrium point in ω space being
continuous with changing perturbation strength). Curves of $T_{\phi EM}^{(s)} + T_{\phi VS}^{(s)} =$

constant can be plotted in ω space (figure 4.7) revealing lines of $T_{\phi EM}^{(s)} + T_{\phi VS}^{(s)} = 0$ for each surface. Over plotting lines of $T_{\phi EM}^{(1)} + T_{\phi VS}^{(1)} = 0$, and $T_{\phi EM}^{(2)} + T_{\phi VS}^{(2)} = 0$, reveal possible steady state equilibrium solutions at the intersections of the two curves (figure 4.8) (further equilibrium points do exist as will be explained in section 4.3.5). Strictly speaking stability of an equilibrium point should be
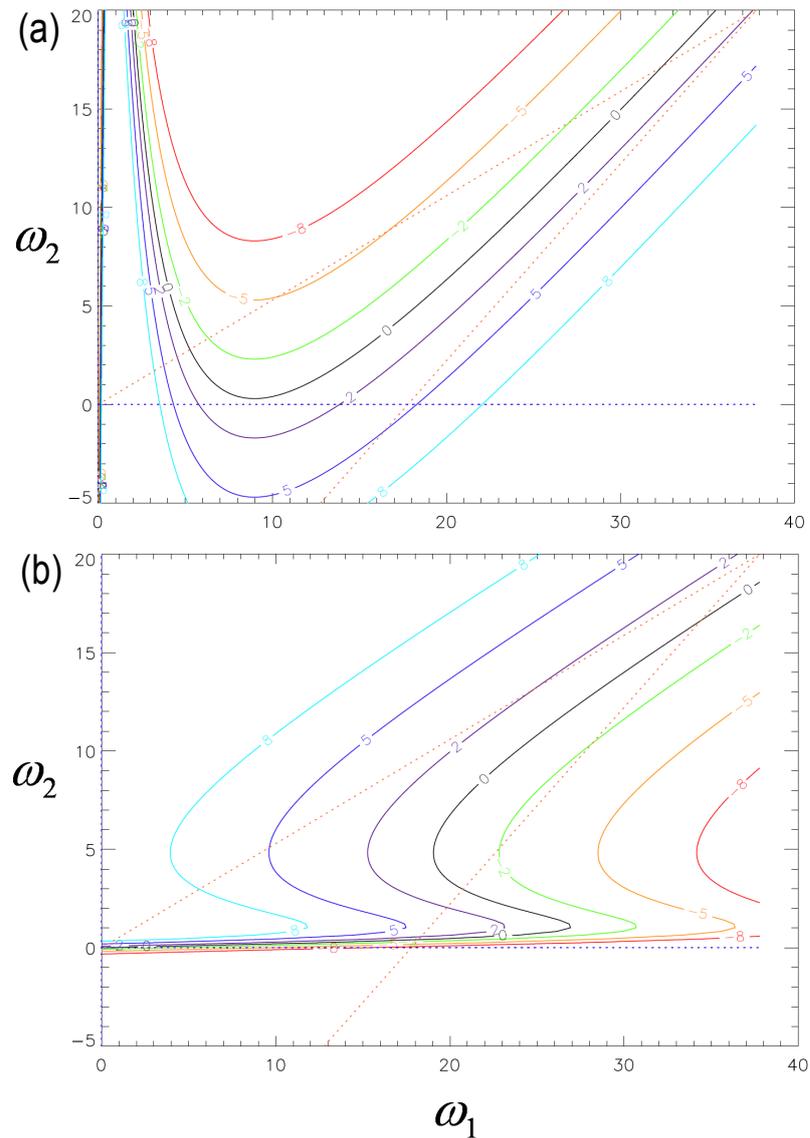
Figure 4.7: (a) curves of $T_{\phi EM}^{(1)} + T_{\phi VS}^{(1)} = constant$. (b) curves of $T_{\phi EM}^{(2)} + T_{\phi VS}^{(2)} = constant$.

deduced from the full system evolution equations. i.e. for each surface momentum equations should be considered of the form:

$$M_s \frac{dV_{\phi(s)}}{dt} = F_{\phi EM}^{(s)} + F_{\phi VS}^{(s)} \tag{4.42}$$

$$F_{\phi VS}^{(s)} = \mu \oint_{A^+} \nabla V_\phi \cdot \hat{n} da + \mu \oint_{A^-} \nabla V_\phi \cdot \hat{n} da \tag{4.43}$$

$$= (2\pi)^2 R_0 r_s \mu (r \frac{\partial V_\phi}{\partial r}|_{r+} - r \frac{\partial V_\phi}{\partial r}|_{r-})$$

The total EM force, $F_{\phi EM}^{(s)}$, is obtained from evolution equation 4.26, a similar form to 4.30 and matching to the outer ψ profiles. M_s is defined $M_s \approx (2\pi)^2 R_0 r_s \delta_s \rho$. The velocity profile for the current model is deduced from the simple diffusion equation.

$$\rho \frac{\partial V_\phi}{\partial t} = \frac{\mu}{r} \frac{\partial}{\partial r} (r \frac{\partial V_\phi}{\partial r}) \tag{4.44}$$

with initial and boundary conditions:

$$\begin{aligned}
\frac{\partial V_\phi}{\partial r}(0,t) &= 0 \\
V_\phi(r_{NBI},t) &= V_{\phi(NBI)}(t) \\
V_\phi(r_1,t) &= V_{\phi(1)}(t) \\
V_\phi(r_2,t) &= V_{\phi(2)}(t) \\
V_\phi(a,t) &= 0 \\
V_\phi(r,0) &= H(r) \tag{4.45}
\end{aligned}$$

Here $H(r)$ is the equilibrium profile under consideration.

However, for the simplified approach applied in this section an equilibrium will be pronounced 'stable', if the sum of the 'steady state' EM torque and viscous torques, calculated in the neighbourhood of ω space surrounding equilibrium point, act to drive the solution back towards the equilibrium point. The relation of the particular 'steady state' forces used to the actual evolution equations is

shown in appendix 1. Figure 4.8 displays the direction the solution would be driven, given a small displacement about the equilibrium point in ω space. Equilibrium points (1) and (3) are considered stable as the torque acts to drive the solution back towards the equilibrium point. Equilibrium point (2) is unstable and solution is driven in the direction of either equilibrium point (1) or (3). Further consideration of these points reveal that stability is dependent on the relative gradients of the lines at the intersection point. For all cases:

$$\frac{d\omega_2}{d\omega_1}\Big|_{(1)} \quad > \quad \frac{d\omega_2}{d\omega_1}\Big|_{(2)} \qquad stable\ point \tag{4.46}$$

$$\frac{d\omega_2}{d\omega_1}\Big|_{(1)} \quad \leq \quad \frac{d\omega_2}{d\omega_1}\Big|_{(2)} \qquad unstable\ point \tag{4.47}$$
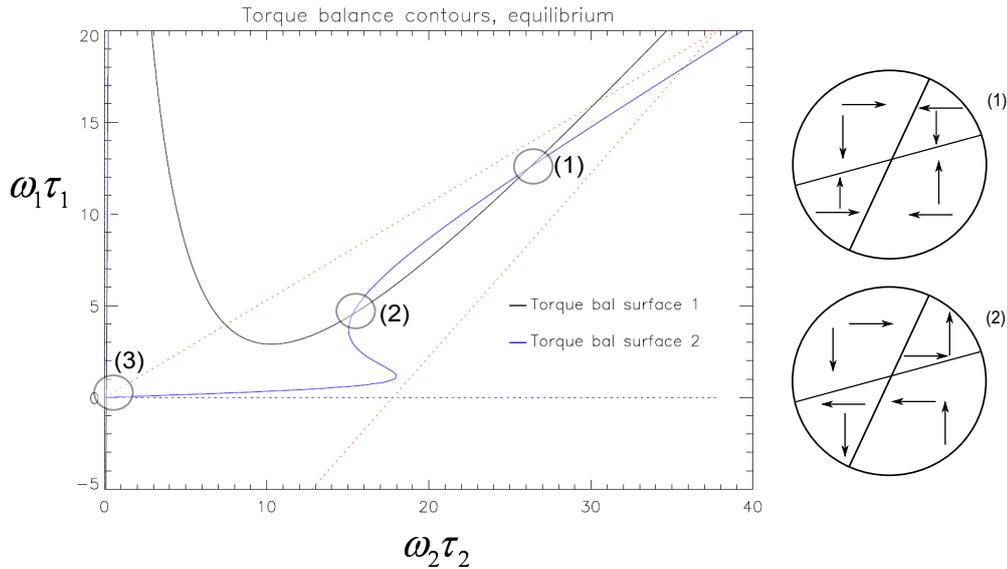
Figure 4.8: (left) Possible equilibrium points. (Right Top/Bottom)direction 'steady state' torque drives solution at equilibrium point (1)/(2)

.

Although considered independently the *psi* space results of the first two surface case presented in this chapter are in qualitative agreement with that considered in [56]. This indicates that the important mechanisms have been retained in both the model and stability analysis considered.

The EM torque at both surfaces acts to decrease the plasma rotation. The rotation decrease is not restricted to the region of the rational surface, but drags down the whole profile. It is in this way that the surfaces are coupled. Figure 4.9 displays the original and new equilibrium velocity profile for particular values of $\Psi_v^{(1)}$ and $\Psi_v^{(2)}$. For the current model, with the condition $r_s > r_{NBI}$, $|U_\phi(r_1)| > |U_\phi(r_2)|$. If $|U_\phi(r_1)| \gg |U_\phi(r_2)|$ then the inner surface may become effectively decoupled from the outer surface, however the outer surface is still dependent on the inner surface. A necessary condition for this assumption to apply is that $r_1 \ll r_2/2$. In the models below $r_{NBI} > a/2$, hence effective decoupling of the inner surface will not occur.
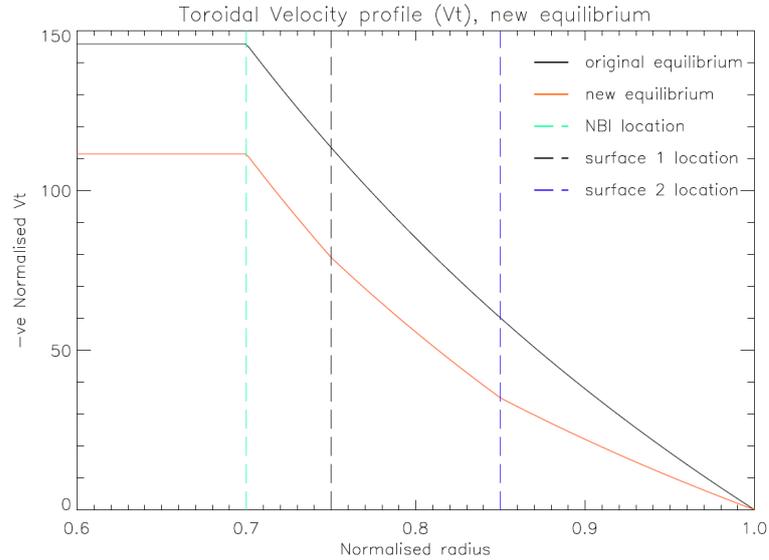
Figure 4.9: normalised toroidal velocity profiles. Profiles include the original equilibrium, and the same perturbation strength applied to the surfaces separately .

4.3.4 Relation to single layer results

It is useful to compare how the normal single layer torque curves relate to ω space and how the general shape of the ω space curves may be understood in terms of the single layer torque curves.

If the applied perturbation only contains a single harmonic, then only one surface will experience a EM torque. For example the case shown in figure 4.10 (lower), a torque is only applied to surface 1. As such any steady state solution must lie on the line of $T_{\phi VS}^{(2)} = 0$. This line intersects lines of constant $T_{\phi EM}^{(1)}$ and $T_{\phi VS}^{(2)}$. Plotting the resulting intersections leads to the usual single layer force balance curve (figure 4.10 (upper)).

The single layer torque curves can also provide insight into the shape of the torque balance curves in ω space. In figure 4.11 the torque balance curve are plotted for surface 2, along 3 locations of constant ω_1. It is seen that the two bends in ω space are due to an 'effective' upward and downward bifurcation. These in turn are due to reduction in the 'effective' ω_0 offset which is controlled by the line of $T_{\phi VS}^2 = 0$. This can be seen by comparing equation 4.37; with its single layer form. The 'effective' ω_0 for each line of constant ω_2 being given by:

$$\omega_0^{eff} = -\frac{M_{12}}{M_{22}}\omega_2 + \frac{G_1}{M_{11}}T_{NBI} \qquad (4.48)$$

A similar analysis follows to obtain the torque balance curves for surface 2.

4.3.5 Bifurcation locusts

It is useful to consider the effect of increasing the perturbation strength on the force balance curves, in ω space, for both surfaces. Figure 4.12 top (bottom) displays lines of $T_{\phi EM}^{(1)} + T_{\phi VS}^{(1)} = 0$ ($T_{\phi EM}^{(2)} + T_{\phi VS}^{(2)} = 0$) for 3 different perturbation strengths. The EM torque increases as the square of the perturbation strength in each case causing a general shift of both turning points away from the $T_{\phi EM} = 0$, $T_{\phi VS} = 0$ intersection.

In single layer analysis the system may undergo a downward bifurcation if the perturbation strength exceeds a critical value, $|\Psi_v|^{(\downarrow)}$. Likewise once a downward bifurcation has taken place, the system may undergo an upward bifurcation if the perturbation strength is reduced below a critical value, $|\Psi_v|^{(\uparrow)}$. Due to the non-linear nature of the EM torque $|\Psi_v|^{(\uparrow)} < |\Psi_v|^{(\downarrow)}$.

Like the single layer system the two layer system may also undergo upward and downward bifurcations. However, a number of possible bifurcation scenarios present themselves for multilayer systems. The downward bifurcation is the
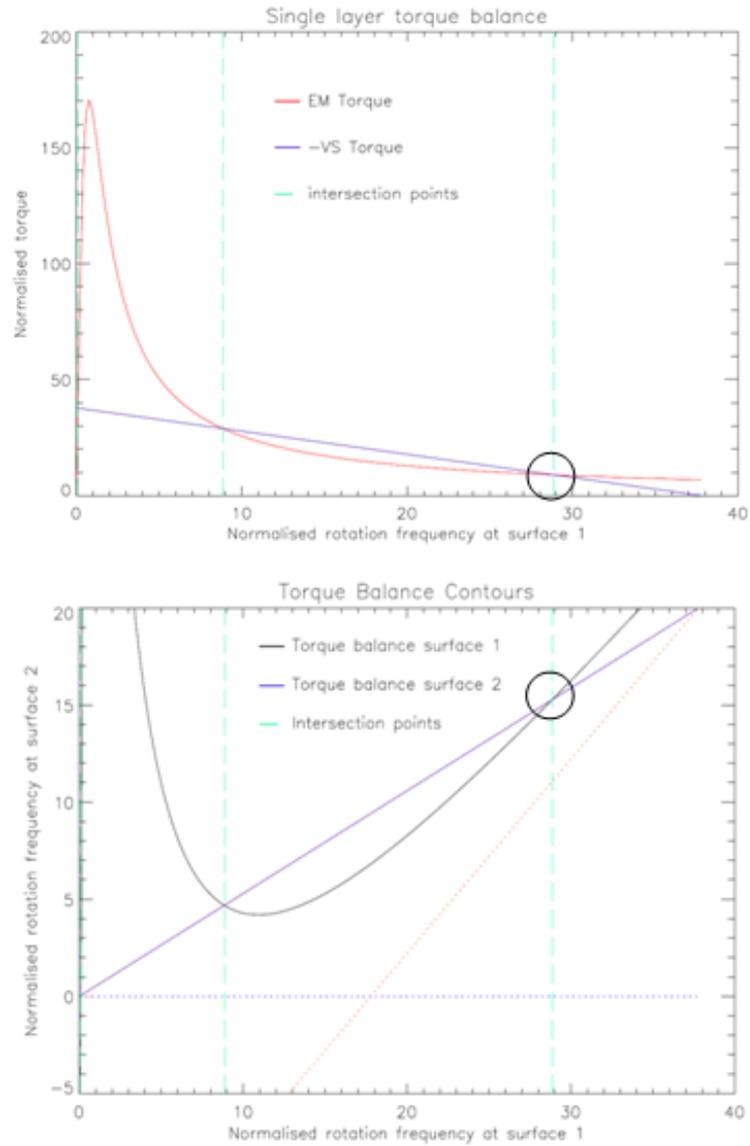
Figure 4.10: Bottom: ω space with a perturbation only applied to surface 1. Top:
The corresponding torque curve corresponding to the usual single layer case
.
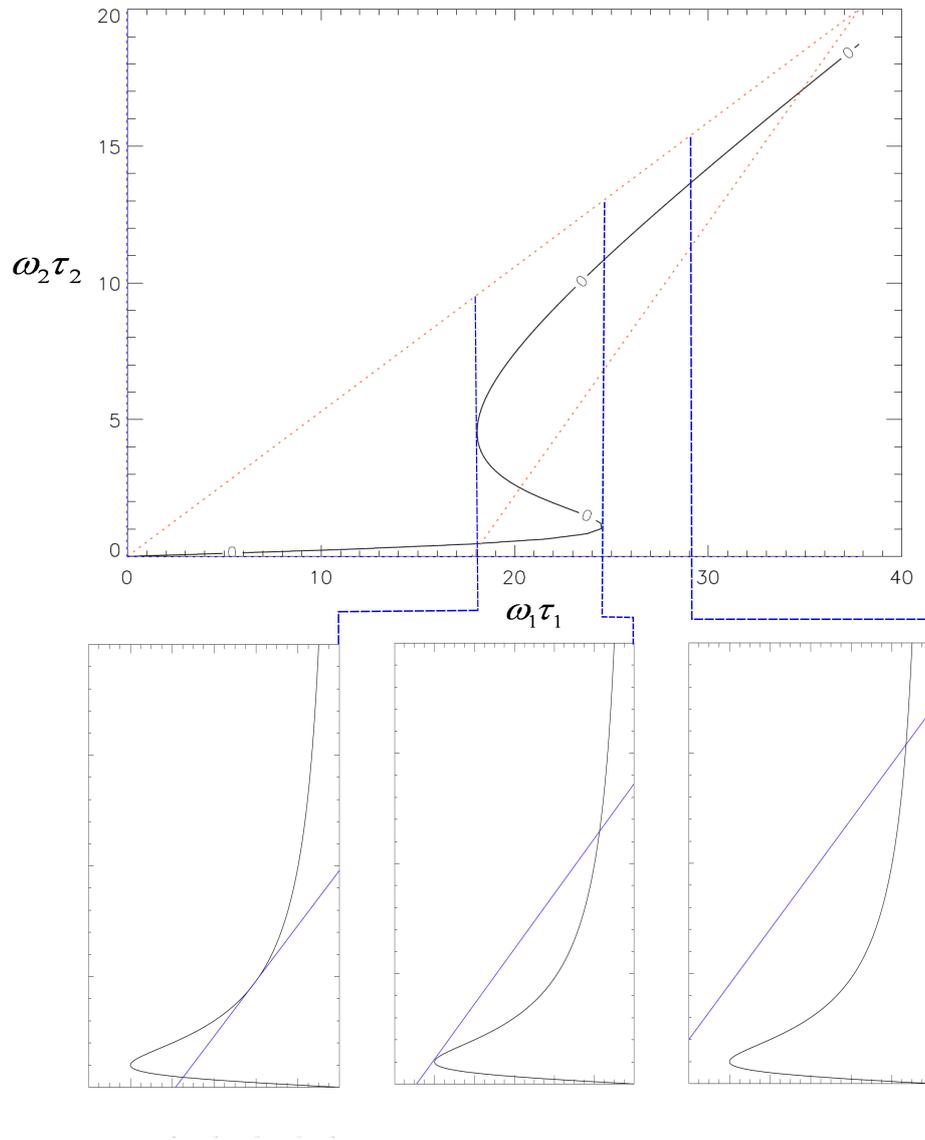
Figure 4.11: Cross-sections of the EM and -ve viscous torque profiles thorough ω space, at selected positions of $\omega_{(1)} = constant$

.
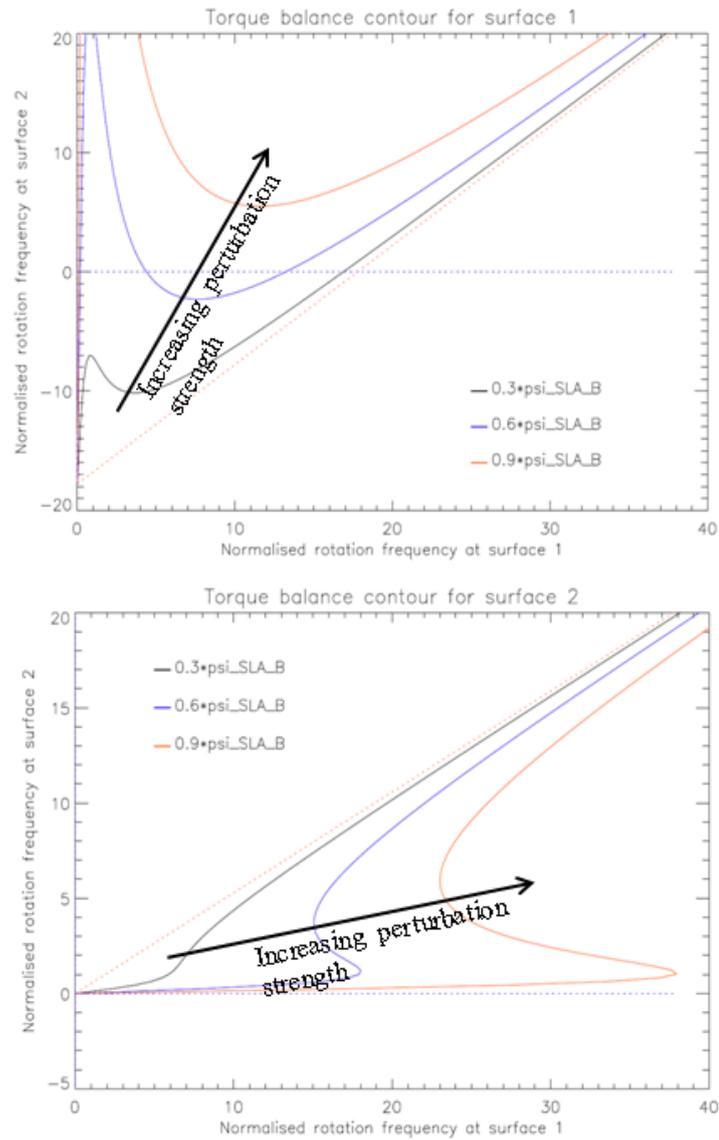
Figure 4.12: Bottom: The effect of increasing perturbation strength on the force balance curves in ω space. Top surface 1. Bottom: surface 2
.

focus of this subsection, the upward bifurcation being expanded upon in a later subsection. As the perturbation strength is increased on either, or both, surfaces, equilibrium point (1) and (2) (figure 4.8) approach each other. If the perturbation strength is further increased, the equilibrium points will merge, then the two curves will separate (figure 4.13 top) allowing for no intersection, and therefore no equilibrium in this region. At this point the system undergoes a downward bifurcation to equilibrium point (3). The corresponding change in the toroidal velocity profile is shown in figure 4.13 bottom. In this scenario both surfaces have bifurcated.

A different bifurcation scenario is displayed in figure 4.14. Again two intersection points merge and then are lost. However, another stable equilibrium exists at position (4). Examination of the force imbalance in various regions of ω space suggests that the system will bifurcate to the intermediate equilibrium point, and this is the approach adopted in the model. In this scenario it is only the outer surface which bifurcates. The corresponding toroidal velocity profile is shown in figure 4.14 bottom. It is noted that due to NBI offset, a critical perturbation strength must be applied to surface 1 before a scenario 1 bifurcation can occur. In addition a system in a scenario 2 bifurcated state may undergo a further bifurcation to the scenario 1 state if the perturbation strength applied to surface 1 is further increased. A upward bifurcation from a scenario 2 state back to the equilibrium (1) state is also possible if the perturbation strength at surface 2 is sufficiently decreased.

The motion of the torque balance curves in figure 4.12 suggests, that the perturbation strength applied to surface 1, required to cause a downward bifurcation from equilibrium (1) will change depending on the perturbation strength applied to surface 2 (and vice versa). It also suggests that the co-ordinate in ω space at which the bifurcation occurs will also be dependent on the perturbation spectrum. Finding the bifurcation point for a range of applied perturbation strengths at each surface reveals a locust of stability in ω space (figure 4.15). The intersection of this locust with the lines of $T_{\phi VS}^s = 0$ are the single layer bifurcation points.

Another locust is obtained by plotting the relative perturbation strengths in ψ space (figure 4.16). Each axis of this plot is normalised to the single layer
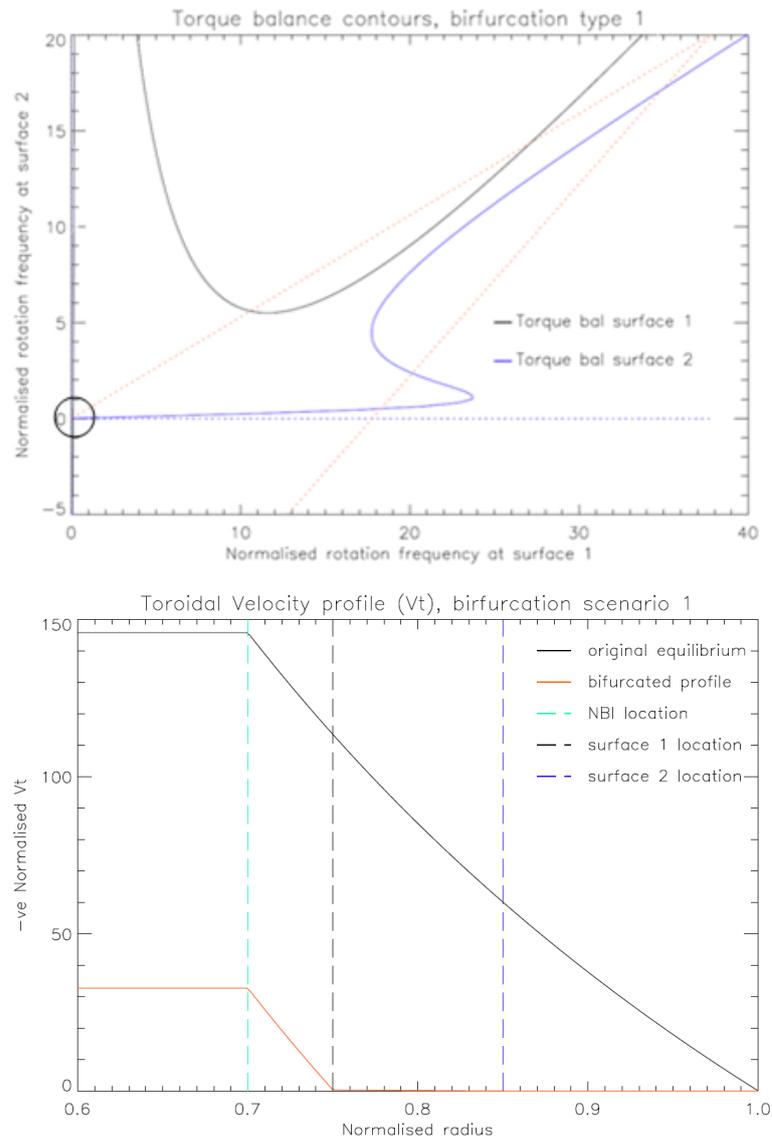
Figure 4.13: Bottom: Top: ω space displaying a bifurcation at both surfaces.
Bottom: The corresponding velocity profile
.
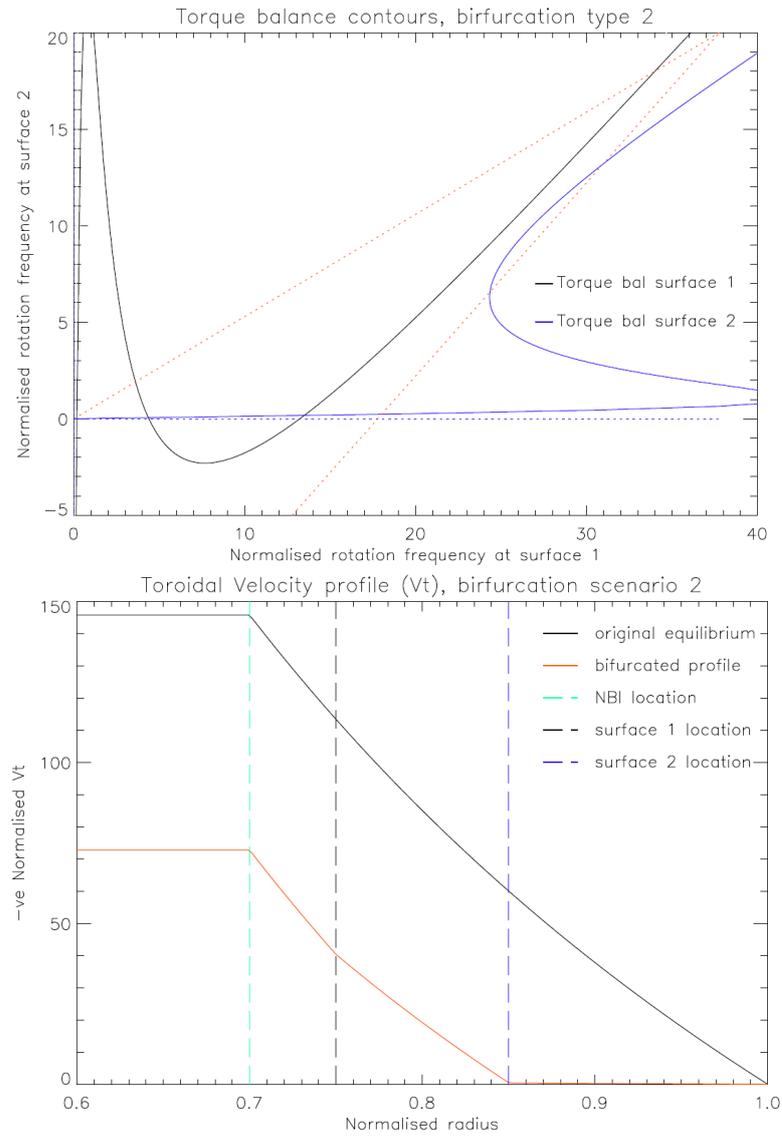
Figure 4.14: Bottom: Top: ω space displaying a bifurcation at the outer surfaces.
Bottom: The corresponding velocity profile
.
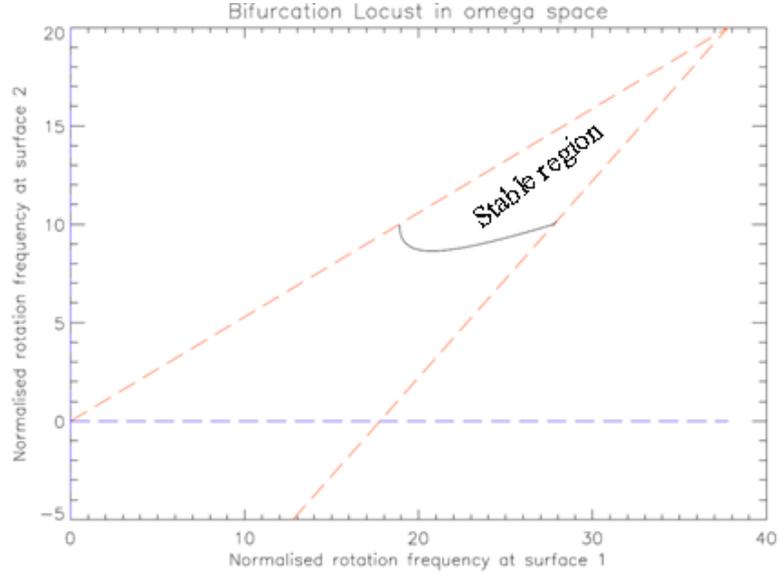
Figure 4.15: The Locust of stability to a downward bifurcation in ω space
.

bifurcation ψ magnitude at that surface. The maximum perturbation strength, of
a particular harmonic, which may be applied to either surface before bifurcation
is that of the single layer case (as should be expected). Clear regions are displayed
indicating which downward bifurcation scenario will initially occur depending on
which region of the threshold curve is crossed.

4.3.6 Inclusion of a diamagnetic offset

The analysis above is similar to that of the 2-field system section 2.1.9. However,
theory suggests that the EM torque will act to drive a single layer towards the
zero in the perpendicular electron velocity section (2.1.10). A simplified version
of this effect is included in the present model by adding an effective 'electron
diamagnetic velocity', $\mathbf{V}^{(dia)}$, to the ψ evolution equation.

$$\frac{\partial \psi_{mn}}{\partial t} + \mathbf{V}_e \cdot \nabla \psi_{mn} = \frac{\eta}{\mu_0} \nabla^2 \psi_{mn} \qquad (4.49)$$

$$\mathbf{V}_e = \mathbf{V} + \mathbf{V}^{(dia)} \qquad (4.50)$$
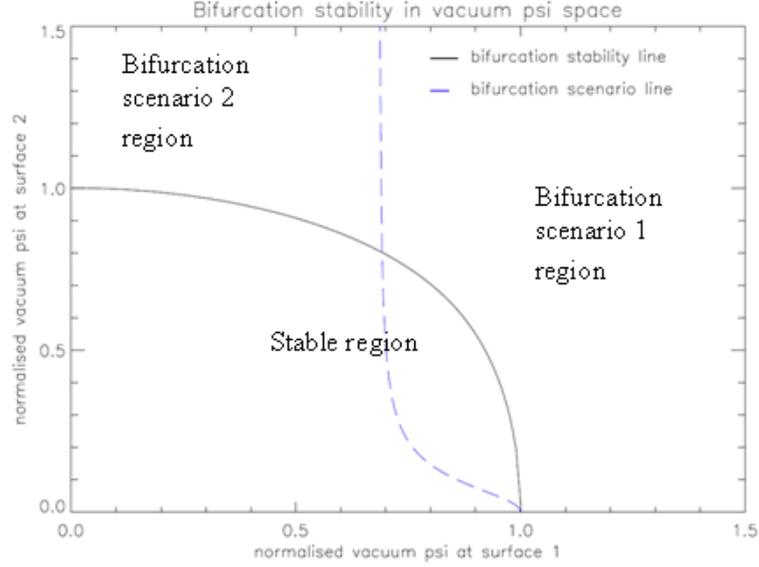
Figure 4.16: The Locust of stability to a downward bifurcation in ψ space. Also
shown is the region of each bifurcation scenario

.

The particular region of interest is the radial neighbourhood surrounding $\mathbf{V}_{\perp e} =$
0, and, it is assumed that this neighbourhood lies just outside the steep pedestal
gradient region. Two conducting surfaces will be considered each responding to
harmonics with the same toroidal mode number, $n = n_1 = n_2$. For simplicity
the electron diamagnetic velocity will contain only a toroidal component, and be
considered constant and non-evolving.

The perpendicular electron rotation frequency is defined as:

$$\omega_{\perp e} = -\frac{n}{R_0} V_{\phi e} = \omega_\perp - \omega_{\perp e}^{(dia)} \tag{4.51}$$

corresponding to $(1/i)\mathbf{V}_e \cdot \nabla$ at the rational surfaces and zeroing when $\mathbf{V}_{\perp e} = 0$.

The above definitions lead to the desired off-set in the EM torque.

$$T_{\phi EM}^{(s)} = n_s m_s |\Psi_v^{(s)}|^2 \frac{\omega_{\perp e(s)} \tau_s}{1 + (\omega_{\perp e(s)} \tau_s)^2} \tag{4.52}$$

To relate to the previous analysis it is considered advantageous to initially
solve for $\omega_{\perp e(s)}$ and not $\omega_{\perp (s)}$. The viscous torque equations are modified accord-

ingly.

$$T_{\phi VS}^{(1)} = (M_{11}\omega_{\perp e(1)} + M_{12}\omega_{\perp e(2)} + (M_{11} + M_{12})\omega_{\perp e}^{(dia)} - G_1 T_{NBI}) \quad (4.53)$$

$$T_{\phi VS}^{(2)} = (M_{21}\omega_{\perp e(1)} + M_{22}\omega_{\perp e(2)} + (M_{21} + M_{22})\omega_{\perp e}^{(dia)}) \quad (4.54)$$

The constant value of the diamagnetic offset is chosen such that $\omega_{\perp e} = 0$ occurs at a particular radial position, $r_{\perp e}$, before any perturbations are applied.

$$\omega_{\perp e}^{(dia)} = -n(1 - \frac{r_{\perp e}}{a})\frac{r_{NBI}}{r_{\perp e}}T_{NBI} \quad (4.55)$$

It is re-iterated that although the radial position at which $\omega_{\perp e} = 0$ may change when perturbations are applied, $r_{\perp e}$ only refers to that position when the perturbations are not applied, and remains constant. Updating the viscous torque equations:

$$T_{\phi VS}^{(1)} = (M_{11}\omega_{\perp e(1)} + M_{12}\omega_{\perp e(2)} - H_1 T_{NBI}) \quad (4.56)$$

$$T_{\phi VS}^{(2)} = (M_{21}\omega_{\perp e(1)} + M_{22}\omega_{\perp e(2)} - H_2 T_{NBI}) \quad (4.57)$$

$$H_1 = n(M_{11} + M_{12})(1 - \frac{r_{\perp e}}{a})\frac{r_{NBI}}{r_{\perp e}} + G_1 \quad (4.58)$$

$$H_1 = n(M_{21} + M_{22})(1 - \frac{r_{\perp e}}{a})\frac{r_{NBI}}{r_{\perp e}} \quad (4.59)$$

4.3.7 The single layer diamagnetic case

Before proceeding with the 2 layer analysis, a single layer case is examined whereby a conducting surface is incrementally moved radially outwards, or radially inwards over the radial domain, Δr, centred at, $r_{\perp e}$. In this scenario, at each radial location, the necessary vacuum perturbation amplitude at the conducting surface, $|\Psi_v^{(s)}|$, and at the coil, $|\Psi_{vc}^{(s)}|$, that is required to induce both an upward and downward bifurcation is recorded. At steady state the latter value can be related to the surface current at the coil location, r_c, necessary for supplying the vacuum perturbation.

The radial width of the contraction/expansion domain is restricted so that it is small compared to $r_{\perp e}$ ($\Delta r/r_{\perp e} \ll 1$). The following notation is used for representing the radial position of the conducting surface, r_1, and the plasma

edge, a.

$$r_1 = r_{\perp e}(1 + \epsilon_1) \tag{4.60}$$

$$a = r_{\perp e}(1 + \epsilon_3) \qquad (\epsilon_3 > 0) \tag{4.61}$$

Assuming $|\epsilon_1|, |\epsilon_3| \ll 1$, a leading order approximation for the downward bifurcations values $|\Psi_v^{(1)}|^{(\downarrow)}$ can be obtained.

$$|\Psi_v^{(1)}|^{(\downarrow)} = \frac{|\epsilon_1|}{2(\epsilon_3 - \epsilon_1)^{1/2}} \frac{(\mu \tau_{(r_{\perp e})})^{1/2}}{m_1} |T_{NBI}| \tag{4.62}$$

$$\tau_{(r_{\perp e})} = \frac{\delta_1 r_{\perp e} \mu_0}{\eta} \tag{4.63}$$

The analytic approximations for the downward bifurcations are displayed with their numerical counterparts in figure 4.17. The corresponding numerical results for the upward bifurcation thresholds, $|\Psi_v^{(1)}|^{(\uparrow)}$, are presented in figure 4.18. It is noted that for a downward bifurcation, $|\Psi_v^{(1)}| > |\Psi_v^{(1)}|^{(\downarrow)}$, while for an upward bifurcation, $|\Psi_v^{(1)}| < |\Psi_v^{(1)}|^{(\uparrow)}$. It is of further note that at specific radial location either side of $r_{\perp e}$, $|\Psi_v^{(1)}|^{(\downarrow)} \to |\Psi_v^{(1)}|^{(\uparrow)}$. No bifurcation threshold exists inside this region.

The relation to the vacuum perturbation amplitude thresholds at the coils, $|\Psi_{vc}^{(1)}|^{(\downarrow)}$, $|\Psi_{vc}^{(1)}|^{(\uparrow)}$, is displayed in figure 4.19. Both $|\Psi_{vc}^{(1)}|^{(\downarrow)}$ and $|\Psi_{vc}^{(1)}|^{(\uparrow)}$ are plotted on the same graph for this case. Two scenarios are envisioned with the aid of this plot. In the first the conductor radius has an initial value $r_1 < r_{\perp e}$ and a value of $|\Psi_{vc}^{(1)}|$ such that is it below $|\Psi_{vc}^{(1)}|^{(\downarrow)}$ at that radius (red dashed line). The conductor is then expanded, whilst maintaining $|\Psi_{vc}^{(1)}|$ constant. At position $(1r)$ the system undergoes a downward bifurcation. Continuing the radial expansion the surface passes $r_{\perp e}$, at which point the EM torque changes direction, and eventually the system undergoes an upward bifurcation at (2r).

In the second scenario the same value of $|\Psi_{vc}^{(1)}|$ is maintained and the conductor positioned at the final location in scenario 1. The conductor is then contracted, the system undergoes a downward bifurcation at position (1l) and then an upward
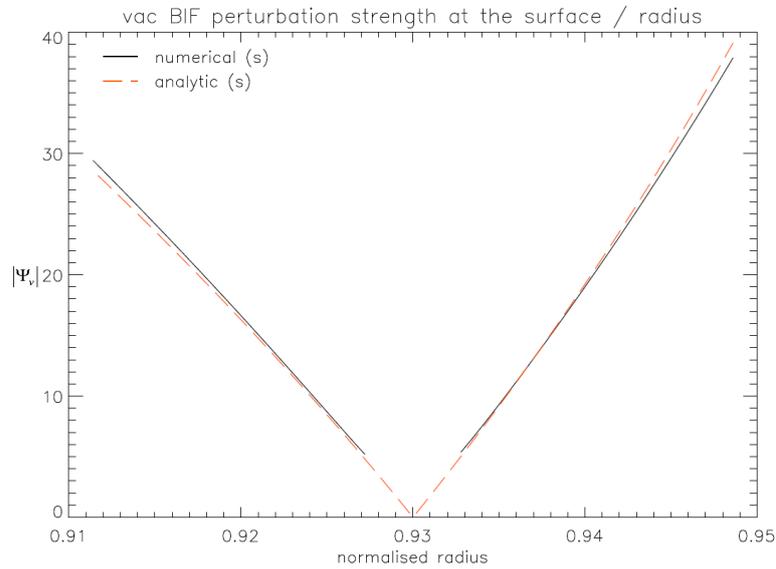
Figure 4.17: The $|\Psi_v|$ threshold, at selection of conductor radii, required to induce a downward bifurcation ($r_{\perp e} = 0.93$).
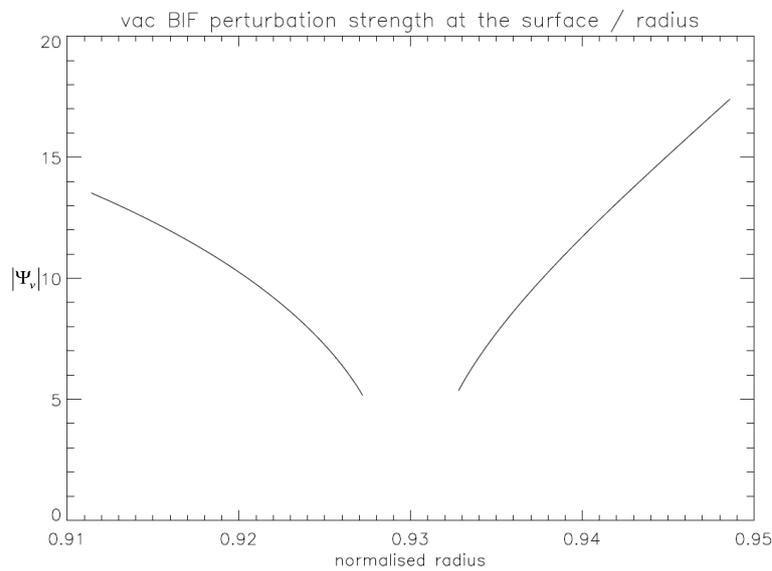
Figure 4.18: The $|\Psi_v|$ threshold, at selection of conductor radii, required to induce an upward bifurcation ($r_{\perp e} = 0.93$).

bifurcation at position (2l).

There are a number of points of note. The width and radial onset of the 'bifur-
cation windows' changes depending on the direction of travel across the surface of
$\omega_{\perp e} = 0$. The width of the 'bifurcation window' in both directions increases with
increasing $|\Psi_{vc}^{(1)}|$ (figure 4.20). Finally, there exists a critical threshold amplitude
below which no bifurcation occurs (an example case is the green dashed line in
figure 4.19).
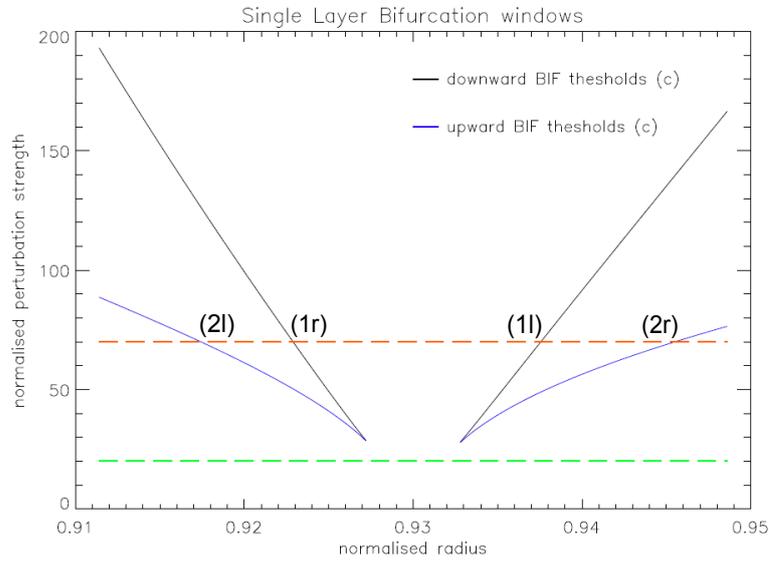
Figure 4.19: Bifurcation windows. The points $(1r)$ and $(2r)$ represent the down-
ward, then upward bifurcation points for the expanding surface. The points $(1l)$
and $(2l)$ represent the downward, then upward bifurcation points for the con-
tracting surface.

4.3.8 The constraint regions

For a system in which the conducting surfaces are positioned such that $r_1 <
r_{\perp e} < r_2$, the shape of the constraint region changes from that of subsection
4.3.3 (figure 4.21). This change reflects the fact that the EM torques will act in
opposite directions. Again the initial equilibrium is at the intersection of the line
of $T_{\phi VS}^{(1)} = 0$ and $T_{\phi VS}^{(2)} = 0$.
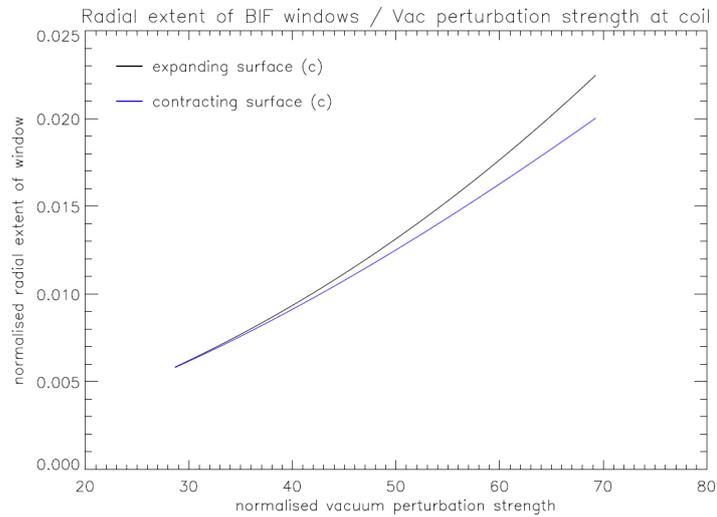
Figure 4.20: radial extent of bifurcation window against vacuum perturbation strength at the coil, for both the expanding and contracting surface.
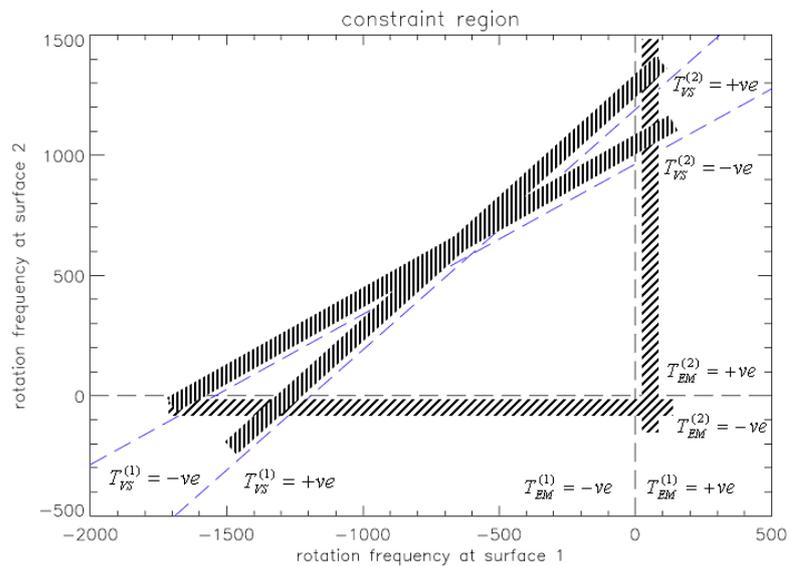
Figure 4.21: The region in which solutions obeying steady state torque balance may exist. The axes correspond to the perpendicular rotation frequency

The significance of the new constraint region, as compared to the previous case, is that one of the torque balance curve is effectively flipped with respect to the other, leading to a different range of possible equilibrium points (figure 4.22).
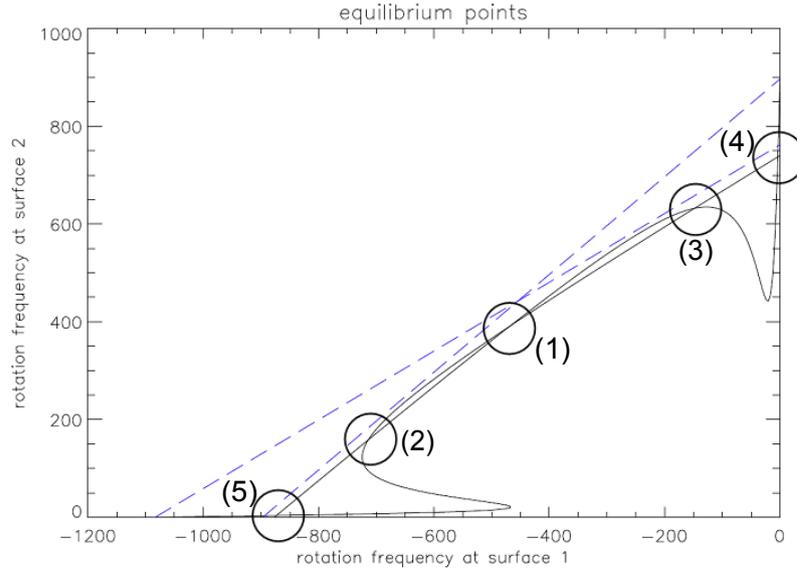
Figure 4.22: Equilibrium points for two surface straddling the $\omega_{\perp e}$ position.

Applying the same rules of stability as applied in section 4.3.3 it is found the equilibrium positions (1), (4), and (5) are stable equilibrium points, whilst (2) and (3) are unstable equilibrium points. Although the positions of the different equilibrium points will slightly alter (and some-times merge or disappear) as $|\Psi_v^1|$ and $|\Psi_v^2|$ are changed, there is in general a collection of points for each equilibrium position where by the type of intersection remains distinct. These collections of points will be referred to as equilibrium regions $(1), (2), (3), (4), (5)$ corresponding with the type of equilibrium shown in figure 4.22. Equilibrium region (1) is that region in which the system starts before perturbations are applied, and the system will remain in this region until the either the onset of bifurcation, or in certain circumstances the merging of two stable equilibrium regions.

An equilibrium point/region (6) also exists, the significance and formation of which will be expanded upon in the next subsection.

4.3.9 Bifurcation locusts for the diamagnetic case

Figure 4.23 displays how the single layer bifurcation case relates to the diamagnetic case in ω space.
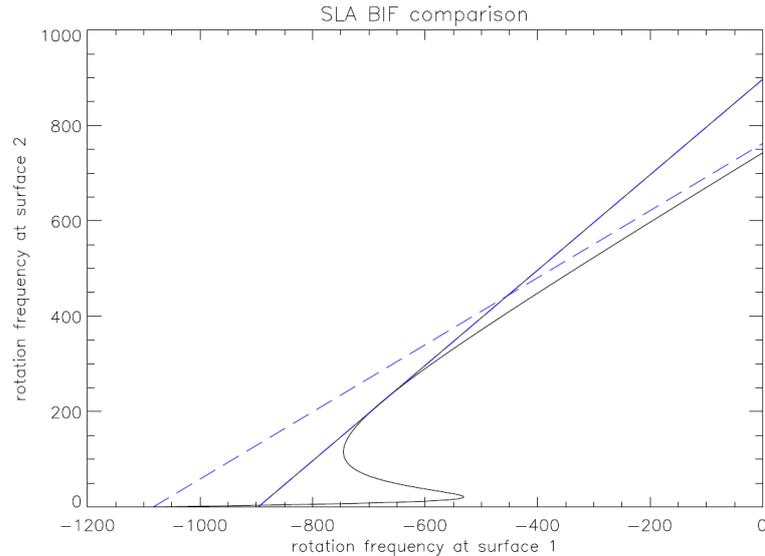
Figure 4.23: The single layer bifurcation as portrayed in ω space.

For the two surface case, with one surface either side of the $\omega_{\perp e} = 0$ surface, the toroidal EM torques act in opposite directions at each surface. Indeed the surfaces now act to help stabilize each other again downward bifurcations. In the previous case (section 4.3.5) it was shown that a maximum perturbation strength, for a particular harmonic, necessary to cause a downward bifurcation was achieved in the single layer case. However, by examination of figure 4.23 and 4.24 it is evident that for the present case the single layer case will provide a minimum perturbation strength, for each harmonic, to induce a downward bifurcation.

Similar downward bifurcation locusts can be drawn in ψ space for the current case (figure 4.25) as were displayed in section 4.3.5 (note this is a downward bifurcation out of equilibrium region (1)).

The cusp, which occurs at the maximum perturbation threshold strength for either harmonic, represents a transition in the direction in which the system is
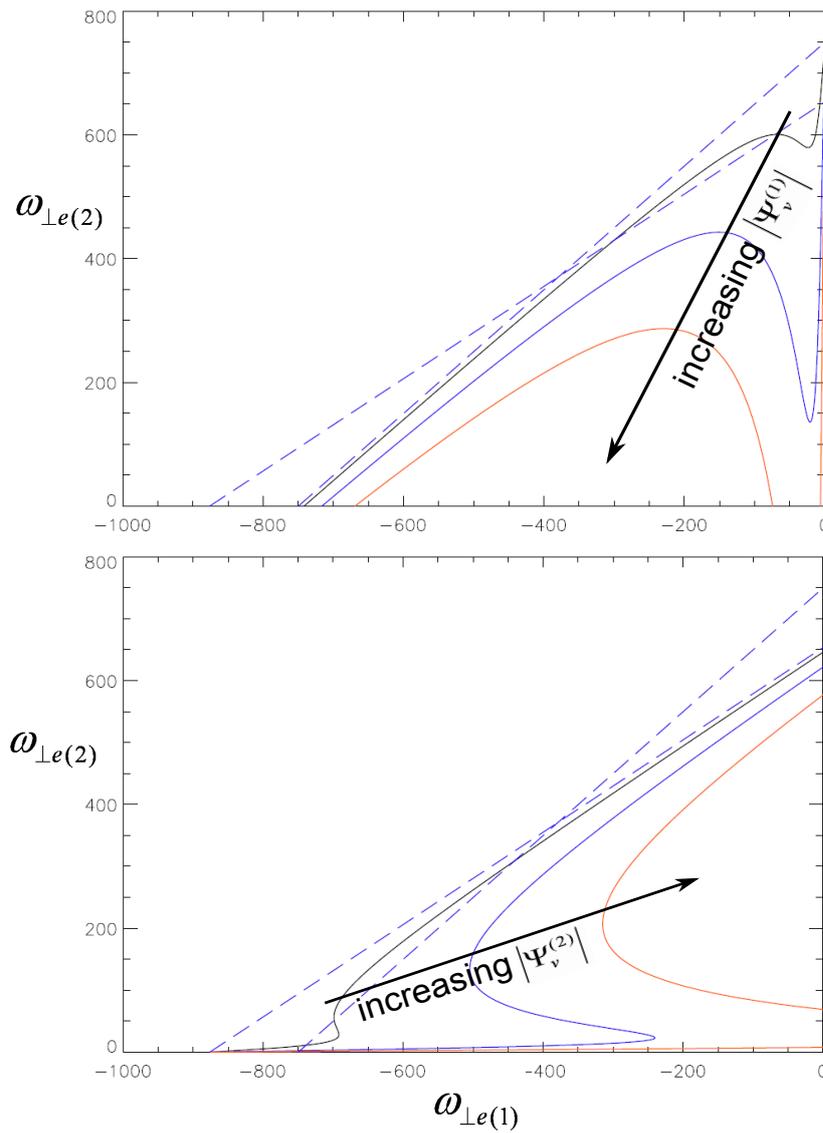
Figure 4.24: The effect of increasing the perturbation strength on the torque balance curves for the diamagnetic case. Top: surface 1. Bottom: surface 2
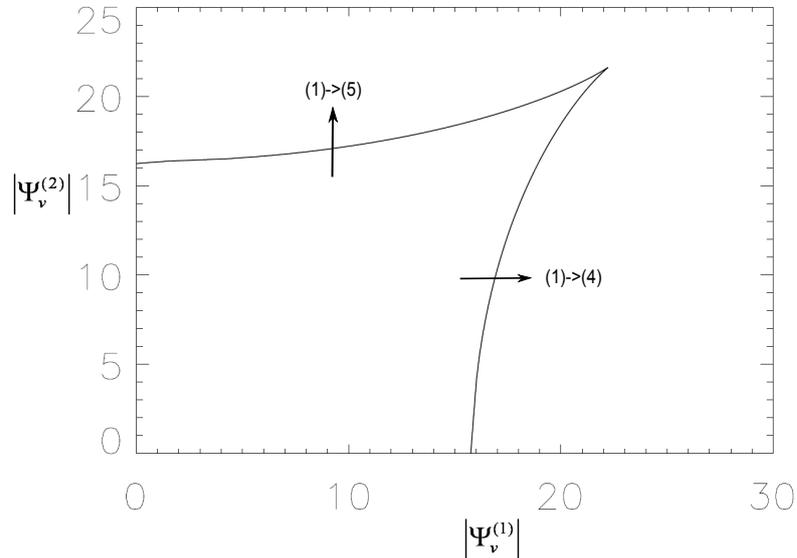
Figure 4.25: The ψ locust for the diamagnetic case, revealing two possible bifurcation roots.

driven. A path though ψ space which crosses the upper boundary will cause the system to be driven from equilibrium region (1) (figure 4.22) towards equilibrium region (5). A path which crosses the right hand boundary will be driven from equilibrium point (1), towards equilibrium region (4). Again this should really be determined from the full system evolution equations but in this simplified analysis this convention will be taken. An example of bifurcation scenario (1) $\rightarrow$ (5) and (1) $\rightarrow$ (4) is displayed in ω space in figures 4.26 (a) and (b) respectively.

ψ spaces can also be obtained for systems bifurcating from equilibrium region (5) (figure 4.27) and equilibrium region (4) (figure 4.28). Bifurcations are induced by crossing the threshold lines in the direction indicated. The threshold curves in both cases will continue indefinitely towards an asymptote at constant $|\Psi_v^{(1)}|$ in figure 4.27 and $|\Psi_v^{(2)}|$ in figure 4.28. There are a number of possible bifurcations which can occur from either of these equilibrium regions, and these may be considered as upward, downward or 'transition' bifurcations. These results along with the respective asymptotes are summerized in figure 4.29. If the threshold is crossed from either equilibrium region (4) or (5) such that the threshold overlaps with the locust from region (1), then there may be a transition from regions
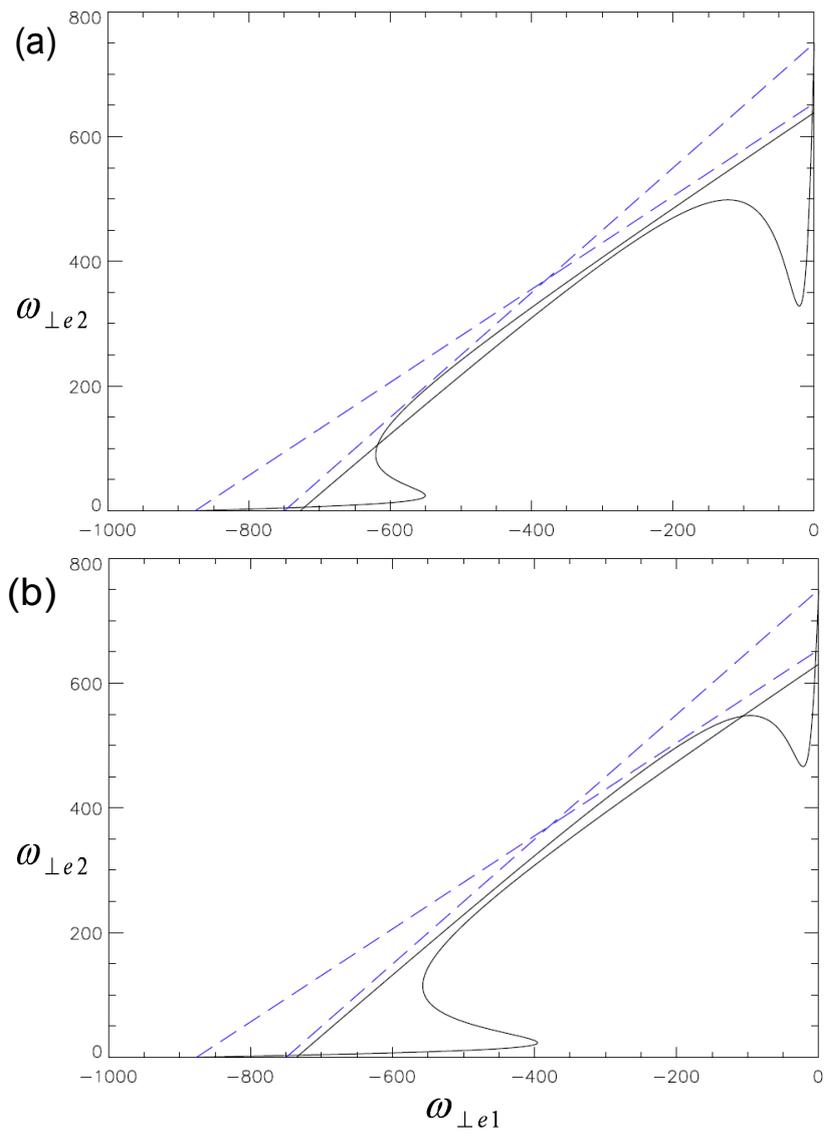
Figure 4.26: Bifurcation from equilibrium region 1 in ω space. Top: a $(1) \rightarrow (4)$ bifurcation. Bottom: A $(1) \rightarrow (5)$ bifurcation

$(4) \rightarrow (1)$ or $(5) \rightarrow (1)$. These are considered as upward bifurcations. If the system is in equilibrium region (4) and the crossing point does not overlap the equilibrium region (1) locust, but overlaps the equilibrium region (5) locust, then there may be a transition bifurcation from $(4) \rightarrow (5)$ (and vice versa it initially in equilibrium region (5)). If no overlap regions exist at the crossing point, the system downward bifurcates to a new equilibrium region (6), a point of which is displayed in ω space in figure (6). Like equilibrium regions (4) and (5), equilibrium region (6) only forms after certain $|\Psi_v^{(s)}|$ thresholds are reached. At this point both surfaces have negligible $\omega_{\perp e(s)}$.
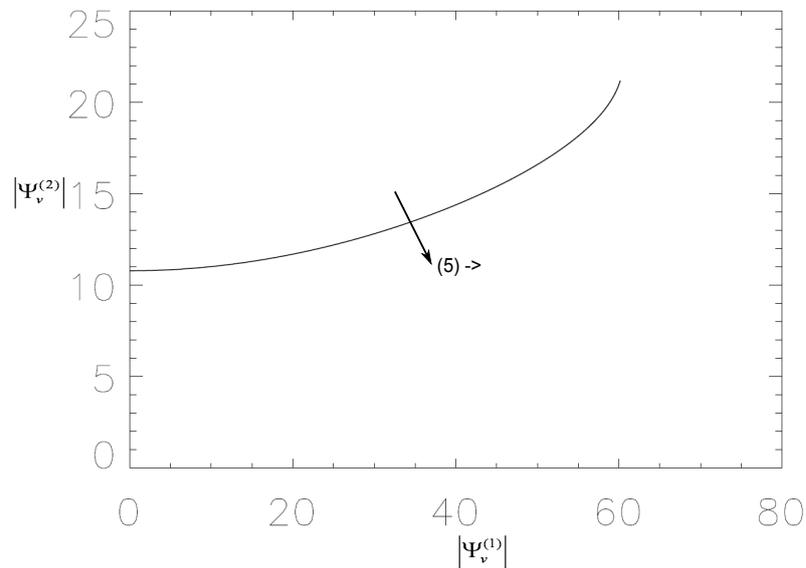
Figure 4.27: The bifurcation locust in ψ space for equilibrium region (5)

Again bifurcation locusts may also be displayed in ω space. As a demonstration case the downward locusts are displayed in figure 4.31. The red x corresponds to the point of the cusp in ψ space. Crossing regions are indicated corresponding to bifurcation scenarios $(1) \rightarrow (4)$ and $(1) \rightarrow (5)$. Similar locusts can be drawn in each region and defines the collection of points for which the 'equilibrium regions' exist.
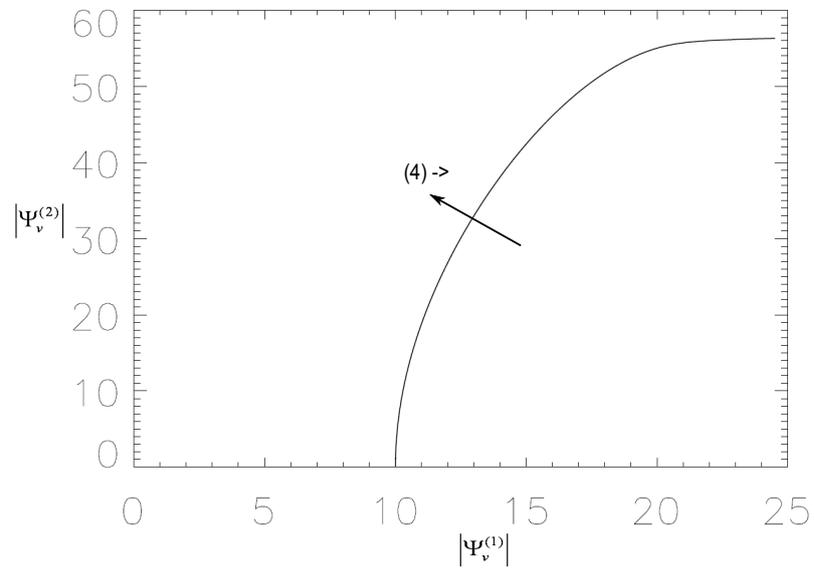
Figure 4.28: The bifurcation locust in ψ space for equilibrium region (4)
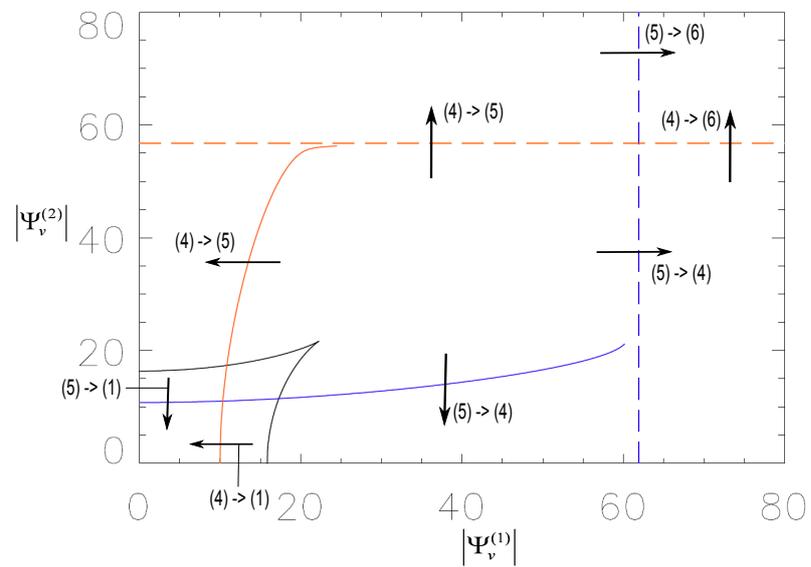
Figure 4.29: The generalised bifurcation map for equilibrium regions (4) and (5)
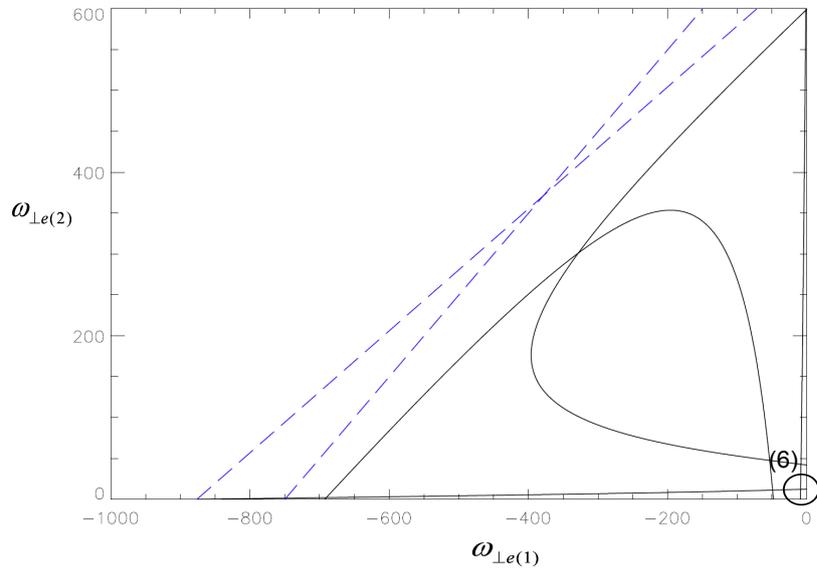
Figure 4.30: Equilibrium point (6)
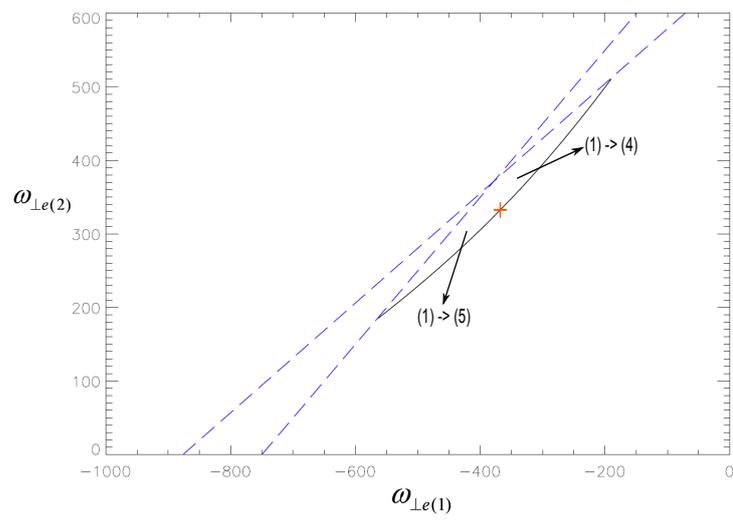
Figure 4.31: change to psi v not vc

4.3.10 The effect of rational surface location

In this subsection a similar analysis is performed to section 4.3.7, whereby the effect of moving rational surface on the bifurcation thresholds is examined. The space referring to the possible positions of both rational surfaces will be referred to as r space. A constraint applied to r space is that $r_{NBI} < r_1 < r_2 < a$. Particular paths through r space are examined. It should be mentioned that the initial equilibrium position of $\omega_{\perp e} = 0$ is $r_{\perp e} = 0.93$. The perturbations applied to both surfaces have a toroidal mode number $n = 3$. The poloidal mode numbers for surface 1 and 2 are $m_1 = 10$ and $m_2 = 11$ respectively.

In the initial analysis one surface is kept at a fixed location whilst the other is incrementally moved. In this analysis $r_1 < r_{\perp e} < r_2$. Figure 4.32 displays the ψ downward bifurcation locusts keeping r_2 fixed whilst moving r_1. The three locusts indicated have radial locations $r_1 = 0.9242$ (black), $r_1 = 0.9205$ (blue), and $r_1 = 0.9186$ (red), i.e. moving away from $r_{\perp e}$ and so to higher initial $\omega_{\perp e}$. Surface 2 is maintained at $r_2 = 0.9395$.
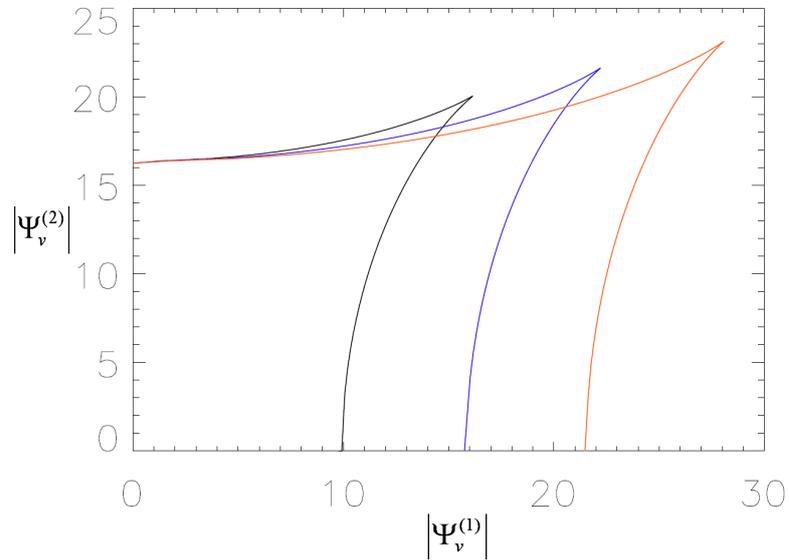
Figure 4.32: Bifurcation locusts in ψ space from equilibrium region (1) at 3 radial locations for surface 1. $r_1 = 0.9242$ (black), $r_1 = 0.9205$ (blue), and $r_1 = 0.9186$ (red). $r_2 = 0.9395$

Figure 4.33 displays a similar analysis this time moving r_2, whilst keeping r_1 fixed. The three locusts have radial locations $r_2 = 0.9358$ (black), $r_2 = 0.9395$ (blue), and $r_2 = 0.9432$ (red), again moving the radial location further from $r_{\perp e}$ and towards higher initial $\omega_{\perp e}$. Surface 1 is maintained at $r_1 = 0.9205$. Note that the blue curves in figures 4.32 and 4.33 are the same.
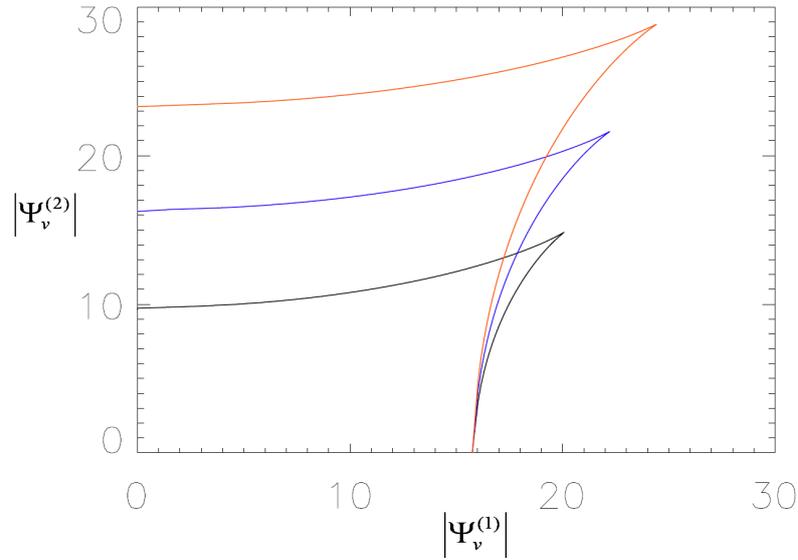
Figure 4.33: Bifurcation locusts in ψ space from equilibrium region (1) at 3 radial locations for surface 2. $r_2 = 0.9358$ (black), $r_2 = 0.9395$ (blue), and $r_2 = 0.9432$ (red). $r_1 = 0.9205$

The corresponding changes in the bifurcation thresholds to equilibrium region (5) and (4) to a movement in the r_1 surface with r_2 fixed are displayed in figures 4.34 and 4.35 respectively. The increments and color coding are the same as for the bifurcation locusts for equilibrium region (1). Figures 4.36 and 4.37 show thresholds with changing r_2, whilst keeping r_1 fixed.

A changing q profile will alter the locations of the rational surfaces, mapping out a particular path through r space. For a demonstration case, a simple q profile functional form is employed ([13]):
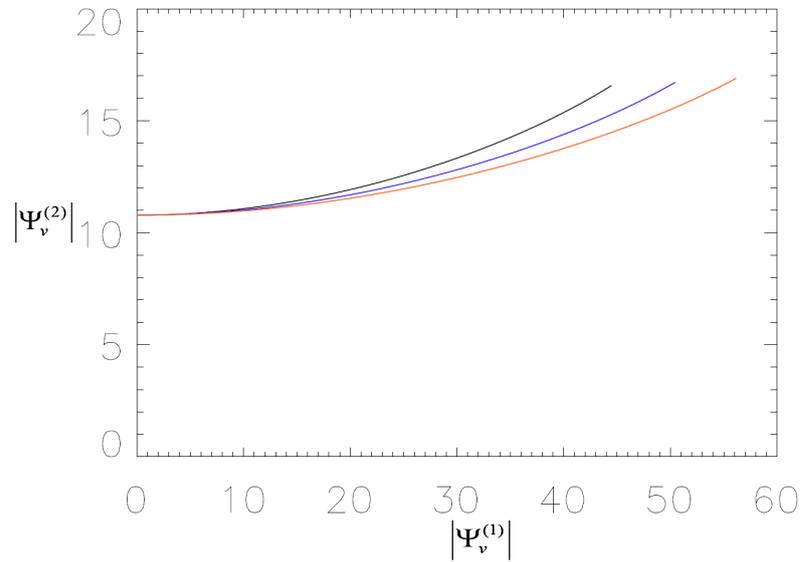
Figure 4.34: Bifurcation locusts in ψ space from equilibrium region (5) at 3 radial locations for surface 1. $r_1 = 0.9242$ (black), $r_1 = 0.9205$ (blue), and $r_1 = 0.9186$ (red). $r_2 = 0.9395$
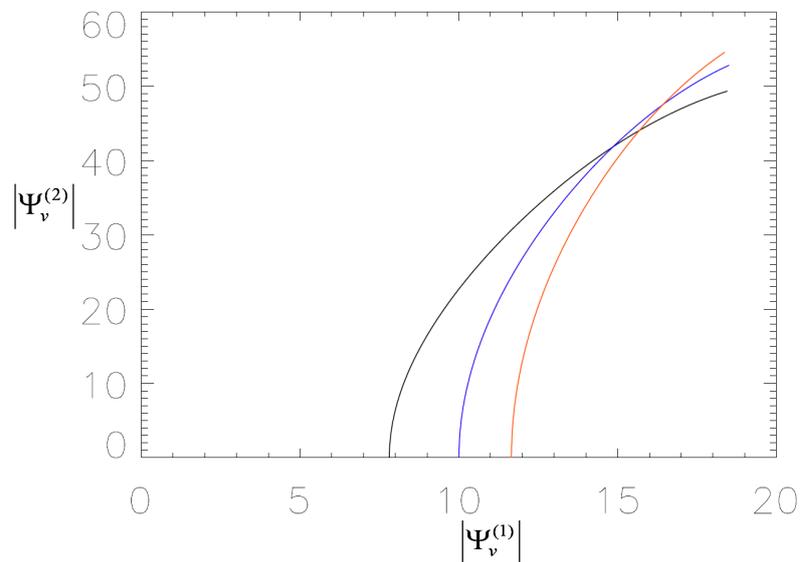
Figure 4.35: Bifurcation locusts in ψ space from equilibrium region (4) at 3 radial locations for surface 1. $r_1 = 0.9242$ (black), $r_1 = 0.9205$ (blue), and $r_1 = 0.9186$ (red). $r_2 = 0.9395$
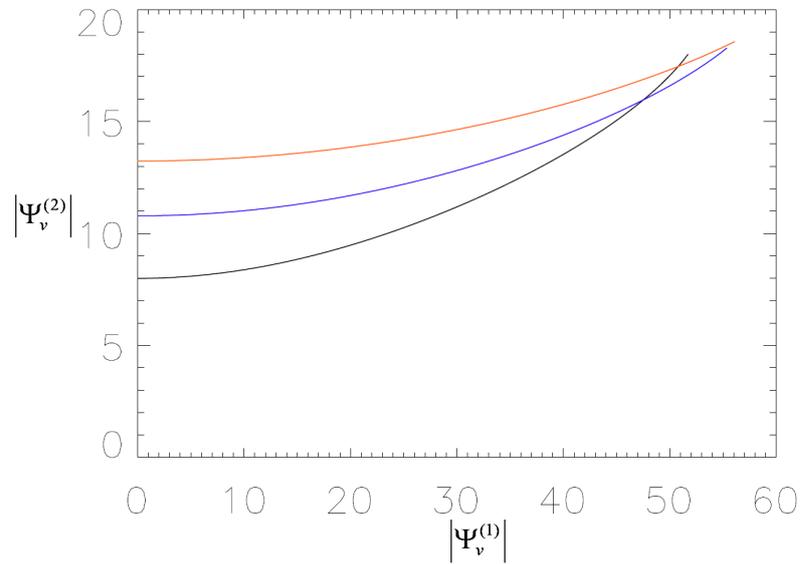
Figure 4.36: Bifurcation locusts in ψ space from equilibrium region (5) at 3 radial locations for surface 2. $r_2 = 0.9358$ (black), $r_2 = 0.9395$ (blue), and $r_2 = 0.9432$ (red). $r_1 = 0.9205$
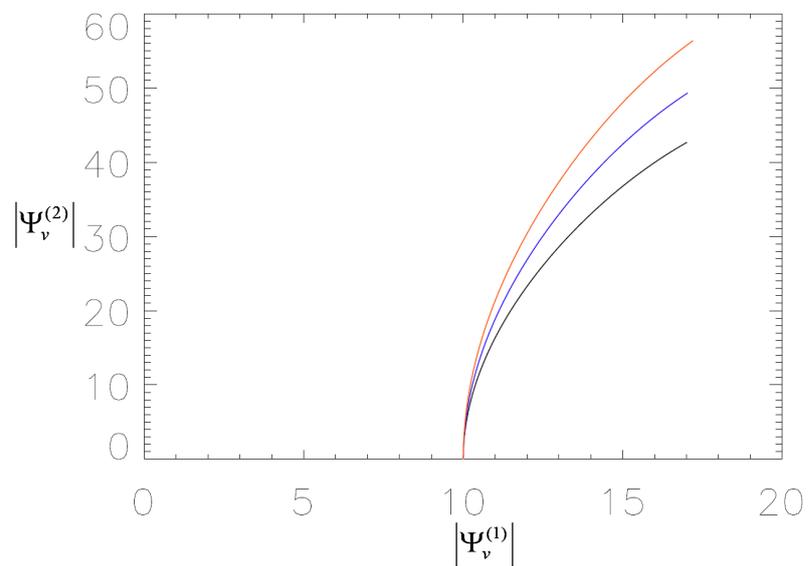
Figure 4.37: Bifurcation locusts in ψ space from equilibrium region (4) at 3 radial locations for surface 2. $r_2 = 0.9358$ (black), $r_2 = 0.9395$ (blue), and $r_2 = 0.9432$ (red). $r_1 = 0.9205$

$$
\begin{aligned}
q(r) &= C_q \frac{r^2}{(1 - (1 - r^2)^4)} \\
C_q &= \frac{2\pi B_\phi}{\mu_0 I_\phi(a) R_0}
\end{aligned}
\tag{4.64}
$$

The q profile is altered by changing the value of C_q, which corresponds to altering either the toroidal field, B_ϕ, or the toroidal current, $I_\phi(a)$. The q profile range and the particular path through r space are displayed in figures 4.38 and 4.39 (solid black line) respectively. Although this q profile is not representive of a H-mode q profile, it serves to illustrate the general concept.
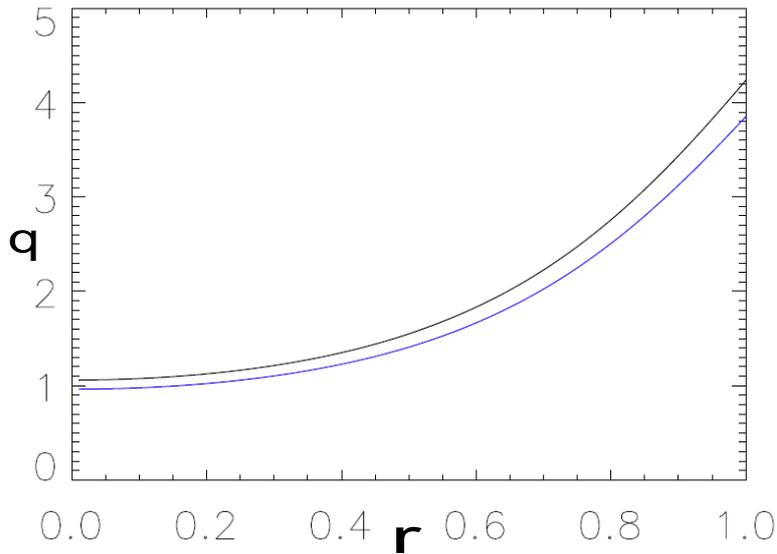
Figure 4.38: The end point of the q profile scan

The ψ space downward bifurcation locusts can be obtained for each point along the path in r space, effectively drawing out a volume of stability along the path. A selection of slices through this volume are displayed in figure 4.40, the colors corresponding to the marked position in figure 4.39. At either end of the path the 10/3 or the 11/3 surface is close to but does not cross the position $\omega_{\perp e} = 0$.

The corresponding thresholds at equilibrium regions (4) and (5) are displayed
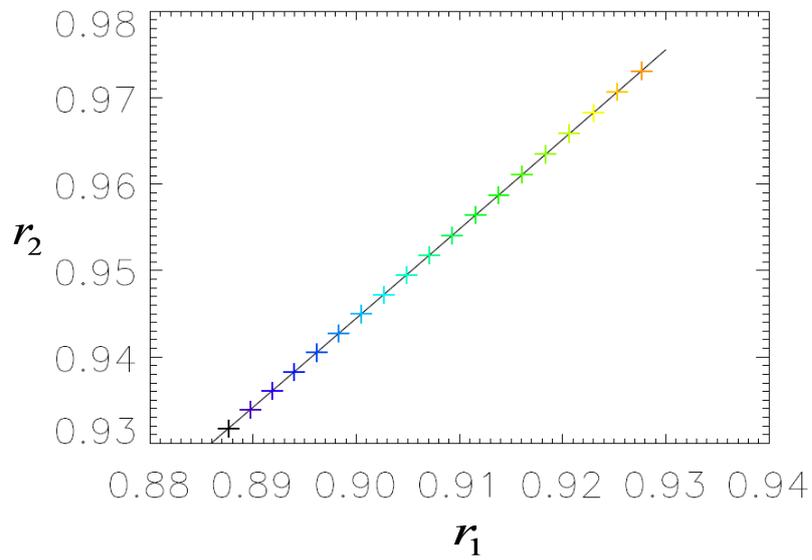
Figure 4.39: the radial path through r space for the q scan and the corresponding
point at which ψ locusts are cut at.
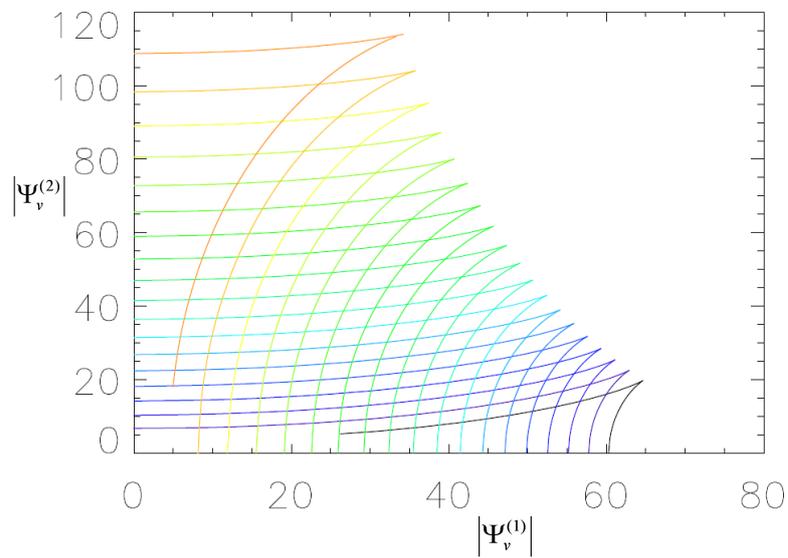
Figure 4.40: Bifurcation locusts from equilibrium region (1) in ψ space for par-
ticular locations in r space

in figures 4.42 and 4.41 respectively. The threshold regions in 4.42 and 4.41 are
only continued to a range which covers the range of the locust from equilibrium
region (1). It is noted that for those locusts which correspond to the end points
in r space, part of the locust appears to be missing. This corresponds to regions
in which threshold lines in the different regions of ψ space meet, and bifurcation
is no longer possible (It also corresponds to a merging of the bifurcation regions
in ω).
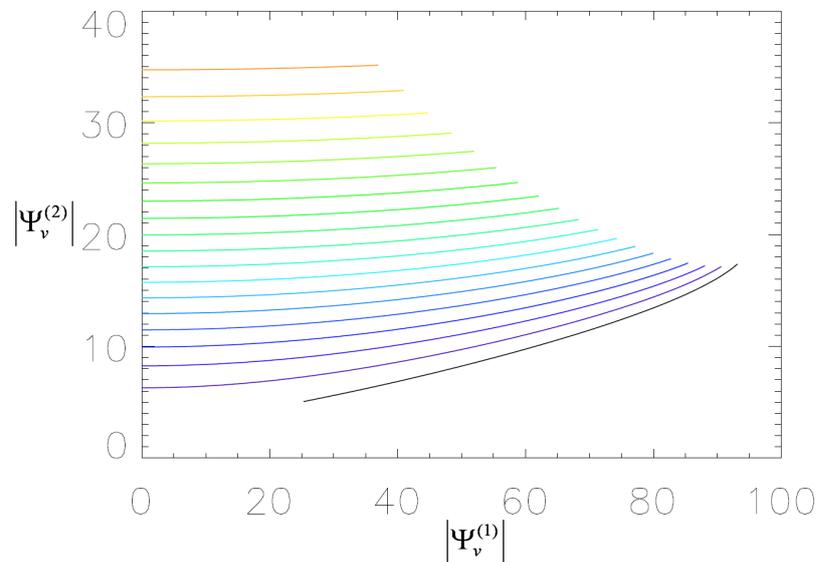
Figure 4.41: Bifurcation locusts from equilibrium region (5) in ψ space for par-
ticular locations in r space

Picking a point in ψ space in figure 4.40, it is clear that this point will only
remain stable to bifurcation to a particular region along the curve in r space. The
direction of movement along the curve in r space will also determine whether a
$(1) \rightarrow (4)$ or $(1) \rightarrow (5)$ bifurcation scenario will take place, corresponding to
the start of a downward bifurcation window similar to that presented in section
4.3.7. The cusps also make clear that the exact ramp path through ψ space may
be important in determining if a certain stable point will be reached.

Likewise figures 4.41 and 4.42 may correspond to the end points of a bifur-
cation window. It is noted from 4.29 that, for more than two surfaces, and the
behaviour bifurcation region (1) locust, that a $(4) \rightarrow (5)$ or $(5) \rightarrow (4)$ type
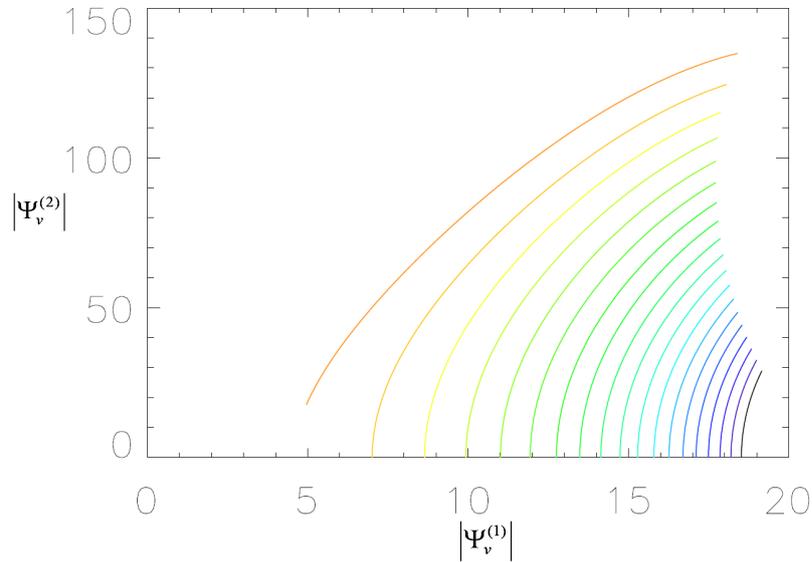
Figure 4.42: Bifurcation locusts from equilibrium region (5) in ψ space for particular locations in r space

bifurcation may be possible, effectively merging one window into the next.

An idea of the relative velocity changes for the diamagnetic case may be obtained directly from the ω space curves. It is useful to compare the magnitude of possible for cases with one rational surface close to the $\omega_{\perp e} = 0$ surface (figure 4.43 lower) and one for which the rational surfaces are approximately equidistant (figure 4.43 upper), both cases about to undergo a $(1) \rightarrow (4)$ bifurcation. The relative jump in ω space for the case with surface 1 close to $\omega_{\perp e} = 0$ is shown to be much smaller than the equidistant case. The jump size, for the case with one surface close, may be greatly increased if the cusp in ψ space is approached (figure 4.40). However, for a realistic ψ spectrum ramp this is thought unlikely to occur.

A detailed discussion of the above results in the context of a comparison with the experimental results of
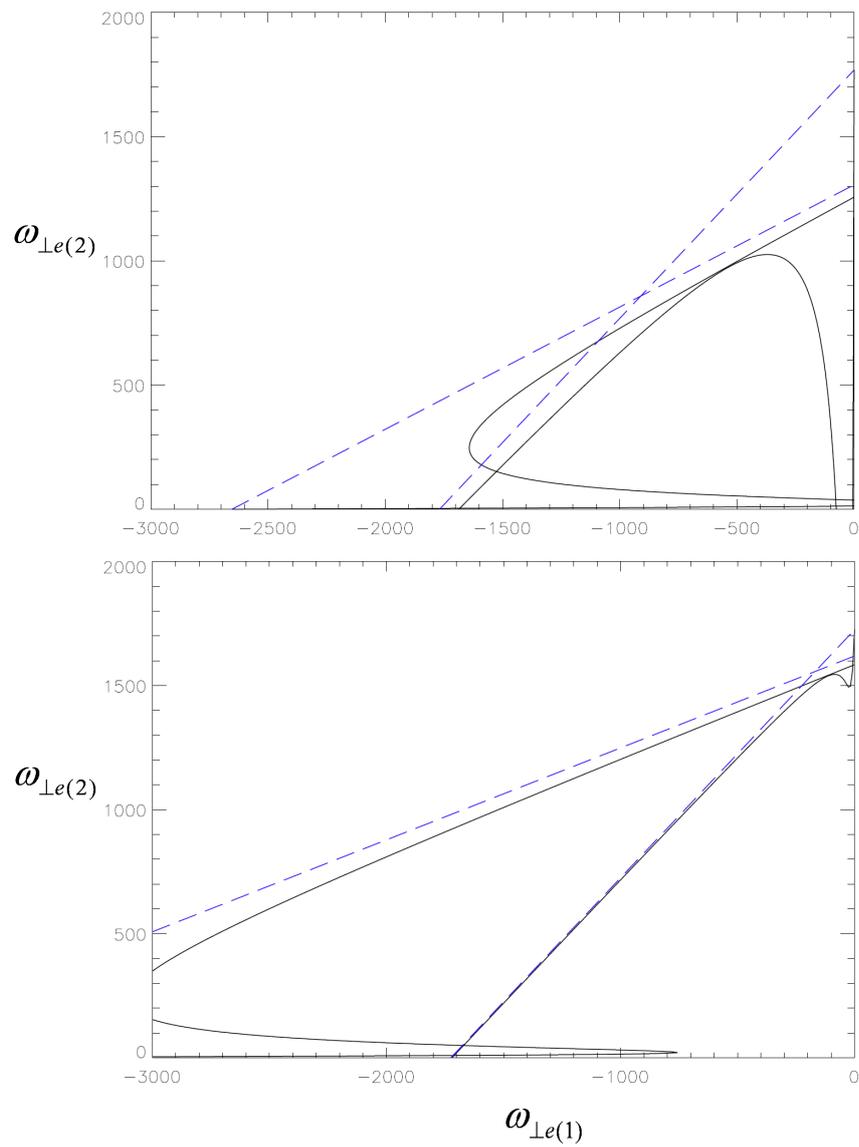
Figure 4.43: The effect of the relative surface location in ω space. Top: surfaces equidistant from $\omega_{\perp e} = 0$. Bottom: surface 1 to $\omega_{\perp e} = 0$ position.

4.3.11 Summary

A novel model has been proposed to analyse equilibrium states of multiple rational surface with differential rotation, subject to magnetic perturbations. A two layer error field type example was considered first to introduce concepts such as ω space and ψ space. Although considered independently displaying bifurcation thresholds in ψ space had already been considered in [56] and in fact provides a validation for the qualitative features of the model proposed in this section.

A diamagnetic off-set was then introduced into the electromagnetic torques at each rational surface. A detailed analysis of possible equilibrium states and bifurcation thresholds was then obtained in the region of the surface of $\omega_{\perp e} = 0$. This is the first time such an analysis has been performed in this region. The radial location of a single rational surface was changed and the bifurcation thresholds obtained to demonstrate the existence of bifurcation windows. In the next chapter these will be shown to have the same qualitative features as the q_{95} windows observed in DIII-D experiments. The model is then extended to a two surface system in which the rational surfaces straddle the position $\omega_{\perp e} = 0$. Due to the torques at each rational surface location acting in opposite directions the possible equilibrium states and bifurcation thresholds are changed from the previously considered two layer case. In the next section the cusp introduced into ψ space will be shown to be a possible explanation for the range of penetration thresholds observed in the DIII-D low collisionality experiments. A move in the relative radial locations of two rational surfaces is then considered, with a particular path chosen to emulate a typical q scan in experiments. This analysis displays the importance on the relative spectrum of the RMP coils as well as the ramp path of these coils through ψ space on the bifurcation thresholds.

Chapter 5

Discussion of Chapter 4 Results

5.1 Comparison with experimental results

In this section the simplified multi-surface model is compared with experimental results, its validity is discussed, and comments made with regards to further work.

It was mentioned that for low collisionality ELM experiments, a surface at which $\omega_{\perp e} = 0$ appears to be a necessary condition to achieving ELM suppression (1.2.8.1). The second half of chapter 4 was devoted to utilizing the simplified model to investigate of the nature of equilibria and bifurcations which may occur around the neighbourhood of this surface, for systems with one and two 'rational surfaces'. To the authors knowledge this is the first time such an analysis has been carried out. The hypothesis is put forward that a bifurcation occurs at one of the rational surfaces straddling the $\omega_{\perp e} = 0$ surface, before ELM suppression occurs. The hypothesis is discussed with the aid of experimental results and the results of chapter 4 to determine if it is realistic.

The single surface case was examined in section 4.3.7. In this section the changes in the upward and downward bifurcation thresholds where examined upon moving the radial location of the surface relative to the initial position of $\omega_{\perp e} = 0$. Ultimately it was found that by crossing the surface of $\omega_{\perp e} = 0$ 'bifurcation windows' existed. A number of interesting features associated with these windows were found.

1. The width of the window increased with perturbation strength.

2. The onset of the window occurred at a greater absolute radial distance from $r_{\perp e}$ with increasing perturbation strength.

3. The radial domain of the window changed depending on the direction of travel of the surface past the $\omega_{\perp e} = 0$ location.

The 1st of these results is certainly in qualitative agreement with the ELM suppression q-windows observed to date. The 2nd result is in agreement with the experimental results presented in figure 5.1. Of further interest is that the onset of q_{95} windows occur relatively close together whilst they end with a much larger gap. At first glance this also appears to be in qualitative agreement with the results of section 4.3.7. However, this is probably somewhat dependent on exactly how the surfaces move with the changing q profile.
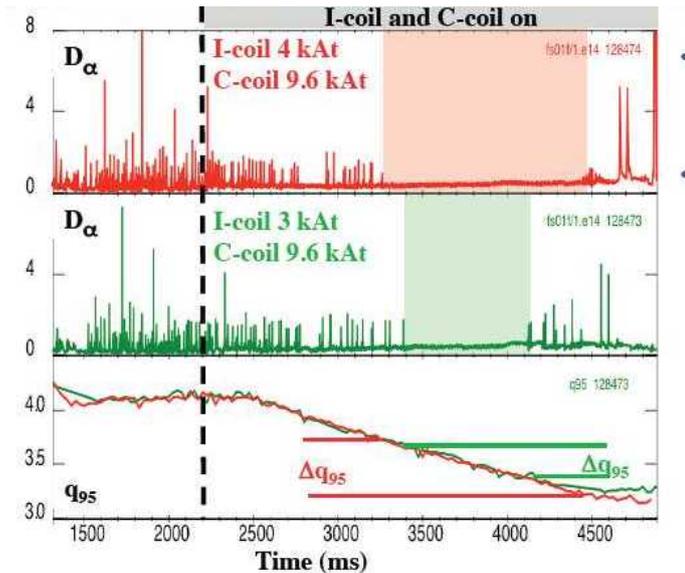
Figure 5.1: q_{95} windows on the DIII-D tokamak, demonstrating an increased window width with increasing perturbation strength. [31]

The author is unaware of a scan which tests the 3rd point. It would appear that this is an experimentally testable prediction and could be tested by scanning up down the q profile close to a known window location (ideally the q profile should be changed by ramping the same variable up or down).

The bifurcation locusts for the diamagnetic offset two layer case were examined in section 4.3.9. Two surfaces were placed at fixed radial locations either side of the surface of $\omega_{\perp e} = 0$ and a downward bifurcation locust (from equilibrium region (1)) obtained in ψ space (figure 4.25 or 5.2). An interesting change was observed in the general shape of ψ space as compared to that obtained in section 4.3.5. This was found to be due relative change in the direction of the EM torque between the two surfaces.
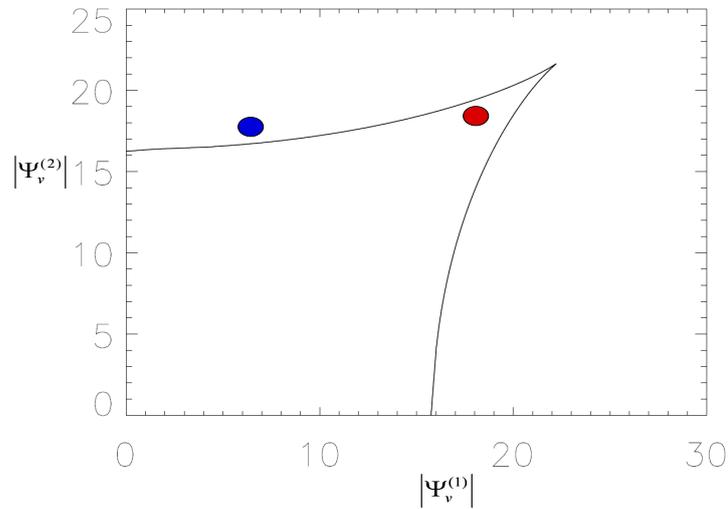
Figure 5.2: Points in ψ space demonstrating that bifurcation may occur at a lower absolute amplitude due to oppositely directed torque about the $\omega_{\perp e} = 0$ surface.

The shape of the ψ space locust provides a possible explanation for the results observed in [20] (figure 5.3). Clear ELM suppression is observed for the spectrum labelled 'both I-coil rows', whereas ELM suppression is not observed for the spectrum labelled 'external C-coil row', even though the absolute magnitude of the applied field is larger in the latter case. If the spectrum plot labelled 'external C-coil row' were to lie at the red point in figure 5.2, whereas the spectrum plot labelled 'both I coils' lies at the blue point, then both spectrum points would be consistent with the hypothesis that the system bifurcates before ELM suppression is observed.

Upon writing this document toroidal velocity profiles for the diamagnetic off-set case have not been obtained, the code created for chapter 4 having to
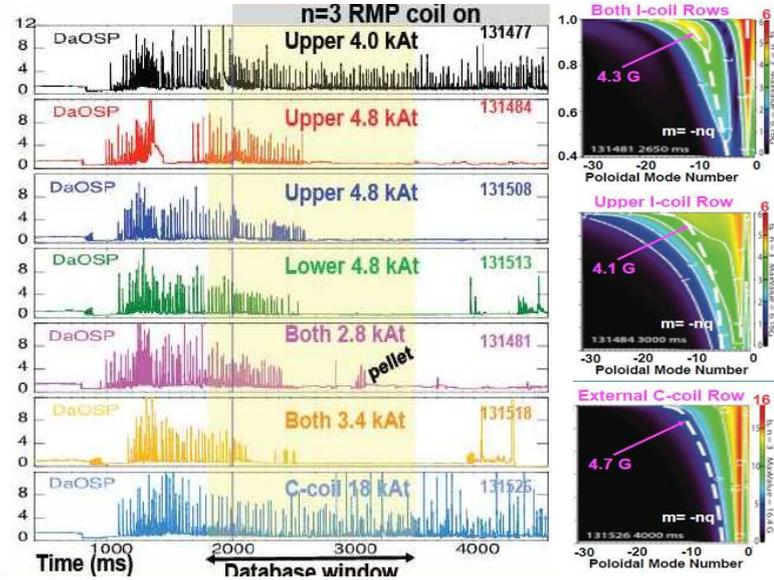
Figure 5.3: Results from the DIII-D tokamak demonstrating that suppression is dependent on the applied spectrum, and not only the perturbation amplitude [36]

undergo a re-model for the diamagnetic case. However, information about the velocity profiles may be obtained from ω space. For a general system with many rational surfaces, those surfaces with radial positions which lie inside the $\omega_{\perp e} = 0$ surface will experience an EM torque which will act to slow the toroidal velocity, whilst surfaces lying outside the location of $\omega_{\perp e} = 0$ will experience an EM torque which acts to increase the toroidal velocity. The two surface system is unlikely to qualitatively reflect experimental results in a bifurcated state. If the inner surface bifurcates there are no further inner surfaces maintaining drag on the core profile, and vice-versa if the outer surface bifurcates. This may be observed from the ω space equilibrium points (4) and (5) in figure 4.22.

What the two layer analysis does suggest is that if the system were ramped sufficiently slowly (so surfaces have time to establish equilibrium) then a change in the toroidal velocity would be expected upon bifurcation. A slight rise in the profile if outer surface bifurcates and slight fall in the profile if the inner surface bifurcates. Examination of figures 4.40 and 4.43 indicates that for a particular velocity equilibrium profile the magnitude of the rise and fall may vary and, is likely to depend on how close the rational is to the surface is to $r_{\perp e}$ (i.e. the

magnitude of the threshold for a particular ramp path through ψ space). Indeed, the velocity change for a case with surface close to $r_{\perp e}$ could be quite small as the initial $\omega_{\perp e}$ at that surface would be small. A possible method of experimental testing would be to examine the velocity profiles whilst performing q-scans in both directions, for a number of different coil currents, and examine the direction and magnitude of change in the toroidal velocity profiles. This is of course dependent on other factors which may effect the toroidal velocity profile.

It must be pointed out that if a bifurcation does precede ELM suppression, and two bifurcations causing the q windows, it still does not demonstrate the mechanism by which ELM suppression occurs, only providing possible threshold for access conditions. It would be the plasma state post downward bifurcation which would actually cause ELM suppression.

Interesting further work for the model presented in chapter 4, would be to extend the model to 3 surfaces. A 3 surface model would enable a more realistic velocity profile to be maintained upon central surface bifurcation. It would also indicate how further surfaces would effect the ψ space bifurcation threshold. For fixed surfaces ψ space would be extended to 3 dimensions, the ψ space locust obtained in section 4.3.9 providing one cross-section in this space, while a locust similar to that in section 4.3.5 providing another for the downward bifurcating case. The constraint regions in ω space would become volumes, the torque balance curves for each surface extruded into surfaces and the common intersections of these surfaces providing the possible equilibrium points. The model would also allow further questions to be asked about the applied spectrum. For example ψ space would provide clear bifurcation thresholds for the inner most surface with respect to those surrounding the $\omega_{\perp e}$ position indicating the possibility of the presence of more common lock mode scenarios which are sometimes observed in experiments.

The simplicity of the model was an attempt to reduce the number of variables involved. The ω, ψ, r spaces could be merged into a single higher dimensional space, in which 'volumes' of bifurcation stability would reside. For a realistic tokamak the number of dimensions would greatly increase. The most obvious omission was any form of current or pressure equilibrium and the corresponding evolution of these equilibrium quantities which is evident from experimental

results. The outer region ψ profiles and therefore Δ' not being accurately reflected. However, as for the bifurcation comparison between the single layer induction motor model and the quasi-linear layer equations, the model may provide a good qualitative comparison so long as the general shape of the torque balance curves are similar, as was found for the constant ψ regimes. The effect of electro-magnetic coupling between rational surfaces was neglected for simplicity. Deviations away from circular geometry allow for coupling between poloidal harmonics, which can alter the distribution of the electro-magnetic torque depending on the applied spectrum. This should be included as further work [62], [56].

5.2 Summery of Experimental Verifications and Predictions

5.2.1 Experimental Verification

1. Experimental result: For a particular initial plasma equilibrium and applied magnetic perturbation spectrum, the q_{95} window sizes increase with perturbation strength (figure 5.1).

   Model result: Bifurcation windows increase in size with increasing perturbation strength (figures 4.19, 4.20).

2. Experimental result: A magnetic spectrum with a lower absolute magnetic perturbation strength may result in ELM suppression, as compared to a different perturbation spectrum with a higher absolute perturbation strength which does not lead to ELM suppression. Both these spectrums are applied to the same initial plasma equilibria (figure 5.3).

   Model result: The resulting cusp in ψ space, caused by the surfaces straddling the surface at which $\omega_{\perp e} = 0$, can lead to increased bifurcation thresholds at a higher absolute applied perturbation strength (figure 5.2).

3. Experimental result: With increased perturbation strength, the absolute difference between the start of the lower and larger perturbation strength

q_{95} windows is less than their absolute difference at the end of the q_{95} window (figure 5.1).

Model results: The largest contribution to the increasing size of the bifurcation window with increasing perturbation strength comes from the change in the upward bifurcation strength threshold. This is due to the shallower absolute gradient of the upward bifurcation threshold with changing radial 'rational surface' location as compared to the downward bifurcation absolute gradient (figure 4.19).

5.2.2   Experimental Predictions

1. Prediction: The range of q_{95} for a particular q window will change depending on whether q_{95} is increasing or decreasing over the window. The start of the q window for either sweep should lie inside the other sweeps range. However the end of the q window should lie outside of the other sweeps range.

   Experimental Test: Scan across a particular q_{95} window (for example by changing the plasma current) with $dq/dt < 0$, then scan across the same window by altering the same parameter with $dq/dt > 0$. The range q_{95} values over which these windows occur is predicted to be different for a set perturbation strength and spectrum. This follows from the results of section 4.3.7.

2. Prediction: A jump in the toroidal velocity profile should occur at the onset of a q_{95} window. The magnitude of the toroidal velocity should decrease for a q-scan with $dq/dt < 0$ and should increase for a q-scan with $dq/dt > 0$. The magnitude of the velocity profile jump is dependent on the particular equilibrium and on the perturbation amplitude and potentially could be quite small. Performing the same scan with an increased perturbation amplitude should increase the magnitude of the velocity jump.

   Experimental test: Perform q-scans over a range of q windows. If possible, measure the toroidal velocity profile. Record the changes in the velocity profile at the onset of a q window. All q-scans performed with $dq/dt < 0$ should lead to a reduction in the magnitude of the toroidal velocity profile.

Conversely all q-scans performed with $dq/dt > 0$ should lead to an increase in the magnitude of toroidal velocity profile. This corresponds to the rational surface at radius less than the surface at which $\omega_{\perp e} = 0$ bifurcating and a surface at with radius greater than the surface of $\omega_{\perp e} = 0$ bifurcating respectively.

Chapter 6

Conclusions

Fusion energy has the potential to be a high energy density base load power supply, which is safe, and with negligible CO_2 emissions. Progress in fusion research over the last 30 years has been remarkable. The next stage in the road to fusion energy is the ITER tokamak, due to start operation in 2020, which is designed to produce 10 times more fusion energy than the energy supplied to the plasma.

The design of such a large scale machine presents large scale technical challenges. One such challenge involves reducing the peak energy loads to the divertor during large type I ELMing operating scenarios. Current models suggest that the divertor plate life-time will be unaccepably short.

The application of RMPs, via coil set external to the plasma, has been proven to be a successful technique for mitigating and suppressing ELMs. However, the physical mechanism behind both mitigation and suppression is not well understood. Furthermore many questions still remain about optimising the applied RMP spectrum, as well as the absolute threshold values.

A number of interesting points are observed in low collisionality experiments which successfully suppress ELMs. Firstly windows of suppression appear to exist when the q_{95} value is ramped over a sufficient range, the windows increasing in size with increasing perturbation strength. An apparently necessary condition for ELM suppression appears to be that there must exist a surface in the plasma at which the perpendicular electron rotation is zero.

The interpretation of experimental results, and the design of RMP coils for

ITER, have relied heavily on vacuum chaos modelling. However, two fluid modelling indicates that islands in the pedestal region are heavily suppressed, and that a self consistent model of the plasma response is required.

The techniques previously applied to error field analysis are now being used and developed to investigate the plasma response to RMPs. In chapter 1 an overview of the reconnection and error field analysis necessary for this document was given, ending with the conclusions of [41] that the plasma should brake towards the electron resonance.

In chapter 2 the BOUT++ code was tested against a selection of analytic results from linear layer analysis. This is the first time that the BOUT++ code has undergone rigorous testing for reconnection and error field linear layer analysis. Reconnection dynamics for the inviscid Taylor problem was compared with the results presented in [52], [53], and [57]. Three scalings were obtained corresponding to the maxima in the reconnection rate at the transition between the inertial and resistive inertial regimes; The maxima in the reconnection rate in the resistive inertial regime; The time to zero in the reconnection rate (or the maxima in the reconnected flux). The scalings were obtained by systematically changing the value of the resistivity. All were shown to be in good agreement. These tests are important for showing that small magnetic island dynamics, or the initial linear phase of larger island growth, can be accurately modelled in the BOUT++ code.

A topic which has been neglected by other authors is to determine the level of radial grid packing required to produce accurate reconnection dynamics at the rational surface. Furthermore, which regime determines the minimum amount of grid packing required. It was found that the relative error accumulated over the inertial regime was independent of resistivity and this regime set a minimum threshold value for the level of grid packing required in all problems. Whether this minimum threshold grid packing was sufficient to accurately model the resistive inertial regime, depended on the value of the resistivity. If the value of the resistivity was higher than a critical value, then the minimum threshold grid pack, determined by the inertial regime, was sufficient to model the resistive inertial regime. However, once the value of the resistivity dropped below a critical value, then additional grid packing was required in the resistive inertial regime.

Furthermore increases in amount of grid packing packing was then required with decreasing resistivity. Determining the minimum level of grid packing required to accurately model reconnection dynamics, and identifying which regimes determine this minimum, is important for all error field and RMP analysis. If inaccuracies are produced in the level of magnetic field penetration, then for a given magnetic perturbation magnitude, inaccurate final state equilibria will be produced. Furthermore, inaccurate bifurcation thresholds will be obtained.

Plasma rotation was introduced and its affect on the reconnection dynamics observed. Temporal profiles of the reconnected flux were displayed, initially showing oscillatory behave in qualitative agreement with the numerical results and analytic predictions of [49]. The time asymptotic, $t \to \infty$, reconnected flux profiles were compared with the analytic predictions and shown to be in good agreement. A slight deviation was observed as the rotation rate increased. This behaviour was expected because the analytic results were obtained in the $Q_\Omega \ll 1$ limit.

The equilibrium was altered in order to introduce a more general equilibrium current profile. The perturbed current in the outer region was compared to the neighbouring equilibria analytic values and found to be in good agreement. The effect of plasma rotation was tested for the new equilibrium, this time with the inclusion of a small amount, $P \ll 1$, of perpendicular viscosity. Good agreement was again displayed.

In chapter 3 a simplified model was developed to investigate bifurcation thresholds for multiple 'effective' rational surfaces coupled by plasma rotation. The model was a hybrid between tokamak and induction motor theory, with the specific aim of reducing the number of variables involved. A two surface model was initially investigated with no diamagnetic offset. Downward bifurcation locusts were obtained for both ω and ψ space. The results of ψ space were found to be qualitatively similar to [56].

Next a constant diamagnetic offset was introduced to produce a surface at which $\omega_{\perp e} = 0$, at a chosen radial location. A detailed analysis of the bifurcation thresholds in this region was carried out for the first time. For the single layer system, downward and upward bifurcation thresholds were obtained over a range of radial locations, the radial domain of testing including the surface of $\omega_{\perp e} = 0$.

Bifurcation windows were produced, the size of which increased with increasing perturbation strength. The radial domains of the windows were also found to be dependent on the direction of travel over the $\omega_{\perp e} = 0$ surface.

Subsequently a two surface system was examined, with the either surface straddling the position of $\omega_{\perp e} = 0$. The constraint and equilibrium points were found to be significantly altered from the case with no diamagnetic offset. This was found to be due to the electro-magnetic torques acting in opposite directions. Downward bifurcation locusts (from equilibrium region (1)) were obtained for both ψ and ω space. A marked difference was found in the geometry of ψ space compared to the previous two layer case. A cusp of increased stability developed, the opposing torques acting to stabilise each other against downward bifurcation. Intermediate equilibria ((4) and (5)) and their corresponding bifurcations were also investigated and a generalised bifurcation map produced.

The effect of altering the relative positions of the two surfaces on the bifurcation thresholds was investigated. In the first instance by maintaining one surface fixed and then incrementally moving the other surface. In the second an effective q scan was performed for a simple q profile. The q scan indicated the bifurcation threshold was relatively sensitive to the relative surface location and that the particular ramp path through ψ space was also important. The q scan revealed the start and end points of possible bifurcation windows, although the surface of $\omega_{\perp e} = 0$ was not crossed in this instance. The type of bifurcation was found to be dependent on the particular direction of the scan.

Finally the relative magnitude of the jump in the velocity profiles, upon bifurcation could be inferred from ω space. The relative jump was found to dependent on how difficult the system was to bifurcate and was dependent on both the surface positions and the particular ramp path though ψ space.

In chapter 5 the results of chapter 4 were compared with experimental results. The q_{95} windows were found to be in good qualitative agreement with the bifurcation windows. In addition the cusp in ψ space offered a possible explanation for the results of [36], where, in a comparison between two applied spectrums, the spectrum with the higher absolute perturbation strength was found not to suppress ELMs, whereas the other was. Experimental procedures were also suggested to test for bifurcation windows.

It was suggested that interesting further work would extend the model to three surfaces. Bifurcation windowing could then be tested with a more realistic velocity profile. In addition it would enable a qualitative means of testing spectrums against the more common lock mode scenarios preceding a bifurcation of a surface straddling $\omega_{\perp e} = 0$.

It was pointed out that the simplified model did not give an indication to the stability of an actual plasma in a bifurcated state. In addition even if a bifurcation windowing was responsible for q-windowing it does not provide the mechanism by which ELM suppression occurs, only a potential threshold to access.

Appendix A

The electromagnetic and viscous forces used in chapter 4 were referred to as 'steady state forces'. What is meant by steady state force is clarified here.

It is relatively straight forward to break up the viscous force into steady state and transient contributions. Considering flow between two surfaces at positions r_1 and r_2, which has evolution equation:

$$\rho \frac{\partial V}{\partial t} = \mu \nabla^2 V \tag{1}$$

and boundary conditions:

$$V(r_1, t) = V_{(1)}(t) \tag{2}$$
$$V(r_2, t) = V_2(t) \tag{3}$$

The steady state contribution, $V_{ss}(r, t)$ is that contribution which satisfies the Laplace equation and the boundary conditions.

$$\nabla^2 V_{(ss)} = 0 \tag{4}$$
$$V_{(ss)}(r_1, t) = V_{(1)}(t) \tag{5}$$
$$V_{(ss)}(r_2, t) = V_{(2)}(t) \tag{6}$$

The transient velocity is defined $V_{(tr)}(r,t) = V(r,t) - V_{(ss)(r,t)}$, with the associated evolution equation and boundary conditions:

$$\rho \frac{\partial V_{(tr)}}{\partial t} = \mu \nabla^2 V_{tr} - \rho \frac{\partial V_{(ss)}}{\partial t} \tag{7}$$

$$V_{(tr)}(r_1, t) = 0 \tag{8}$$

$$V_{(tr)}(r_2, t) = 0 \tag{9}$$

The viscous force acting in the surface is broken up into the transient contribution an the steady state contribution, $F_{VS} = F_{VS}^{(ss)} + F_{VS}^{(tr)}$

The electromagnetic torque is more difficult to brake up. In general $\psi(r,t) = \psi_{ss}(r,t) + \psi_{(tr)(r,t)}$. If surface 1 has rotation frequency $\omega_{(1)}(t)$, then $\psi_{ss}(r,t)$ is defined to be to be the profile of $\psi(r,t)$ if surface was in force balance at this rotation frequency. The steady state electromagnetic force, $F_{EM}^{(ss)}$, is defined in a similar fashion, the transient part being defined by $F_{EM}^{(tr)} = F_{EM} - F_{EM}^{(ss)}$.

References

[1] UN. *World Population Prospects. The 2010 Revision. Highlights and Advance Tables.* United Nations, New York, 2011. 1

[2] BP. *BP energy outlook 2030.* British Petroleum, London, 2012. 1

[3] C. Llewellyn-Smith. Meeting the future energy demand. *Transactions at Fusion Technolgy Conference, Univerity of York*, 2013. 1, 3

[4] WHO. *Review of evidence on health aspects of air pollution - REVIHAAP Project.* WHO Regional office to Europe, Copenhagen, Denmark, 2013. 2

[5] Core Editors: R. K. Pachauri and A. Reisinger. *Climate Change 2007: Synthesis Report.* IPCC, Geneva, Switzerland, 2007. 2

[6] D. J. C. Mackay. *Sustainable Energy - without the hot air.* UIT, Cambridge, UK, 2009. v, 2

[7] J. Ongena and G. Van Oost. Energy for future centuries - prospects for fusion power as a future energy source. *Fusion Science and Technology*, 61(2T), 2012. 3, 4, 5

[8] OECD and IAEA. *Uranium 2009, Resources, Production and Demand.* OECD Nuclear Energy Agency and International Atomic Energy Agency, 2010. 3

[9] UMPNER Review Taskforce. *Uranium Mining, Processing and Nuclear Energy - Oppertunities for Australia.* Australian Government, Australia, 2006. 4

[10] R. Keith Evans. Lithium reserves and resources. *Energy*, 3, 1978. 4

[11] I. Cook and et al. Saftey and environmental impact of fusion. *Report EFTA-S-RE-1, EUR(01) CCE-FU/FTC 8/5*, 2001. 5

[12] J. Friedberg. *Plasma Physics and Fusion Energy.* Cambridge University Press, Cambridge UK, 2007. 5, 13

[13] J. Wesson. *Tokamaks.* Oxford Univeristy Press, Oxford UK, third edition, 2004. 7, 9, 132

[14] G. Van Oost and R. Jaspers. Thermonuclear burn criteria. *Fusion Science and Technology*, 61(2T), 2012. 9

[15] R. Fitzpatrick. Driven reconnection in magnetic fusion experiments. *Lecture Notes*, 1995. ix, 12, 92, 93

[16] H. J. de Blank. Guiding centre motion. *Fusion Science and Technology*, 61(2T), 2012. v, 12, 13

[17] H. J. de Blank. Plasma equilibrium in tokamaks. *Fusion Science and Technology*, 61(2T), 2012. 13, 40

[18] D. Schnack. *University of Wisconsin Madison Magnetohydrodynamic lecture notes.* v, 15

[19] R. Fitzpatrick. Bifurcated states of a rotating tokamak plasma in the presence of a static error field. *Phys. Plasmas*, 5:3325, 1998. vii, 16, 56, 57, 58, 62, 64, 88, 90

[20] F. Wagner and et al. Regime of improved confinement and high beta in neutral beam heated divertor discharges of the asdex tokamak. *Phys. Rev. Lett.*, 49:1408–1412, 1982. 16, 143

[21] F. Wagner. A quater-century of h-mode studies. *Plasma Phys. and Control. Fusion*, 49:B1–B33, 2007. 16

[22] P. B. Snyder and et al. Edge localised modes and the pedestal: A model based on coupled peeling-ballooning modes. *Phys. of plasmas*, 9(5):2037–2043, 2001. 16

[23] H. R. Wilson. Edge localised modes in tokamaks. *Transactions of fusion science and technology*, 61:122–130, 2012. 16

[24] A. Kirk. Elm characteristics in mast. *Plasma Phys. Control. Fusion*, 46:551–572, 2004. 16

[25] A. Loarte and et al. Characteristics of type i elm energy and particle losses in existing devices and their extrapolation to iter. *Plasma Phys. Control. Fusion*, 45:1549, 2003. 16

[26] A Loarte and et al. Transient heat loads in current fusion experiments, extrapolation to iter and consequence for its operation. *Phys. Scr.*, T128, 2007. 16

[27] A. Kirk. Understanding the effect resonnant magnetic perturbations have on elms. *Transaction at the 40th European Physical Society Confernce on Plasma Physics, Espoo*, 2013. v, vi, 17, 19, 20, 27

[28] H. Zohm. Edge localised modes. *Plasma Phys. Control. Fusion*, 38:105–128, 1996. v, 18

[29] E. Nardon, A. Kirk, N. Ben Ayed, M. Becoulet, P. Cahyna, T. E. Evans, G. Huysmans, H. R. Koslowski, Y. Liang, S. Saarelma, and P. R. Thomas. Elm control by resonant magnetic perturbations on jet and mast. *J. Nucl. Mater.*, 390-391:773–776, 2009. vi, 22

[30] M. J. Schaffer, T. E. Evans, M. E. Fenstermacher, and R. A. Moyer. Elm suppression by resonant magnetic perturbations at diii-d. *23rd IEEE/NPSS symposium on Fusion Enineering*, 2009. vi, 23

[31] M. E. Fenstermacher and et al. Effect of island overlap on edge localised mode suppression by resonant magnetic perturbations in diii-d. *Plasma Phys. Control. Fusion*, 47:B37–B52, 2005. vi, xii, 24, 26, 92, 142

[32] A. Kirk and et al. Understanding the effect resonnant magnetic perturbations have on elms. *Plasma Phys. control. Fusion*, 55:124003, 2013. 24

[33] K. H. Burrel and et al. Elm suppression in low edge collisionality h-mode discharges using n = 3 magnetic perturbations. *Plasma Phys. Control. Fusion*, 47:B37–B52, 2005. vi, 24

[34] M. R. Wade. Advances in the physics understanding of elm suppression using resonnant magnetic perturbations in diii-d. *Transactions at the IAEA Fusion Energy Consference, San Diego, California*, 2012. vi, 25

[35] T. E. Evans and et al. Rmp elm suppression in diii-d plasmas with iter similar shapes and collisionalites. *Nucl. Fusion*, 48:024002, 2008. vi, 25

[36] M.E. Fenstermacher. Suppression of type-1 elms using a single toroidal row of magnetic field perturbations coils. *Nucl. Fusion*, 48:122001, 2008. vi, xii, 28, 92, 144, 152

[37] A. Kirk and et al. Observation of lobes near the x-point in resonant magnetic perturbation experiments on mast. *arXiv:1202.0160*, 2012. vi, 34, 35

[38] A. J. Thornton, A. Kirk, I. T. Chapman, and J. R. Harrison. Divertor heat fluxes during mitigated and unmitigated elms. *Transactions at the 20th plasma surface interactions conference*, 2012. 34

[39] E. Nardon and et al. Quasi-linear mhd mode plamsa response to resonnant magnetic perturbations. *Nucl. Fusion*, 50:034002, 2010. 34, 62, 91

[40] F. L. Waelbroeck. Shielding of resonant magnetic perturbations in the long mean-free path regime. *Phys. Plasmas*, 10(10):4040–4047, 2003. vii, 34, 35, 58, 61, 62

[41] F. L. Waelbroeck, I. Joseph, E. Nardon, M. Becoulet, and R. Fitzpatrick. Role of singular layers in the plasma response to resonant magnetic perturbations. *Nucl. Fusion*, 52:074004, 2012. 34, 60, 62, 91, 150

[42] R. J. Goldston and P. H. Rutherford. *Introduction to Plasma Physics*. Taylor and Francis Group, Oxford, U.K., 1995. 36, 37

[43] R. D. Hazeltine and J. D. Meiss. *Plasma Confinement.* Dover Publications, New York, 2003. 37, 38, 39, 45, 47, 54

[44] T. J. Boyd and J. J. Sanderson. *The Physics of Plamsa.* Cambridge University Press, Cambridge, U.K., 2003. 37

[45] J. Kevorkian and J. D. Cole. *Perturbation Methods in Applied Mathematics.* Springer-Verlag, New York, second edition, 1981. 39, 46

[46] R. D. Hazeltine, M. Kotschenreuther, and P. J. Morrison. A four-field model for tokamak plasma dynamics. *Phys. Fluids*, 28(8):2466–2477, 1985. 40, 58

[47] B. D. Dudson. *University of York MCF lecture Notes http://www-users.york.ac.uk/ bd512//teaching/mcf.html.* vii, 45

[48] J. D. Murray. *Asymptotic Analysis.* Springer-Verlag, New York, 1984. 46, 47, 49, 50

[49] R. Fitzpatrick and T. C. Hender. The interaction of resonant magnetic perturbations with rotating plasmas. *Phys. Fluids B*, 3(3):644–673, 1991. 48, 54, 151

[50] H. P. Furth, J. Killeen, and M. N. Rosenbluth. Finite-resistivity instabilities of a sheet pinch. *Phys. of fluids*, 6(4):459–481, 1963. 48

[51] W. Kaplan. *Advanced Mathemathics for Engineers.* Addison-Wesley Publications, Massachusetts, 1981. 49

[52] T. S. Hahm and R. M. Kulsrud. Forced magnetic reconnection. *Phys. Fluids*, 28(8):2412–2418, 1985. 51, 150

[53] A. Cole and R. Fitzpatrick. Forced magnetic reconnection in the inviscid taylor problem. *Phys. Plasmas*, 11(7):3525–3529, 2004. 51, 62, 63, 67, 150

[54] R. Fitzpatrick. A numerical study of forced magnetic reconnection in the viscous taylor problem. *Phys. Plasmas*, 10(6):2304, 2003. 51, 62, 63

[55] R. Fitzpatrick. Interaction of tearing modes with external structures in cylindrical geometry. *Nucl. Fusion*, 33(7):1049, 1993. 58

[56] R. Fitzpatrick and T. C. Hender. Effect of static magnetic perturbation on resistive mode stability in tokamaks. *Phys. Plasmas*, 1:3337, 1994. 60, 62, 91, 92, 107, 140, 146, 151

[57] R. Fitzpatrick. Scaling of the peak magnetic reconnection rate in the inviscid taylor problem. *Phys. Plasmas*, 15:024503, 2008. 62, 63, 67, 74, 87, 150

[58] M. F. Heyn and et al. Kinetic estimate of the shielding of resonant magnetic perturbations by the plasma in diii-d. *Nucl. Fusion*, 48:024005, 2008. 62

[59] Y. Liu and et al. Full toroidal plasma response to externally applied non-axisymmetric magnetic fields. *Phys. Plasma*, 14:122502, 2010. 63, 64, 88, 91

[60] B. D. Dudson, M. V. Umansky, X. Q. Xu, P. B. Snyder, and H. R. Wilson. Bout++: a framework for parallel plasma fluid simulations. *J. Comput. Phys.*, 180:1467–1480, 2009. 64, 65

[61] M. V. Umansky, X. Q. Xu, B. Dudson, L. L. LoDestro, and J. R. Myra. Status and varification of edge plasma turbulence code bout. *J. Comput. Phys.*, 180:887–903, 2009. 64

[62] R. Fitzpatrick. Error-field induced electromagnetic torques in a large aspect ratio, low-β, weakly shaped tokamak plamsa. *Phys. Plasmas*, 16:032502, 2009. 146